
Tokamak Modelling and Control



Atul Stefan Sharma

A thesis submitted for the degree of
Doctor of Philosophy of the
University of London and for the
Diploma of Membership of Imperial College

Centre for Process Systems Engineering
Imperial College of Science Technology and Medicine
London SW7 2BY
United Kingdom

Supervisor: D J N Limebeer

January 2002

Abstract

This thesis is concerned with the modelling and control of tokamak nuclear fusion reactors. A nonlinear model is derived using the classical arguments of Hamiltonian mechanics from which a low-order linear model is derived. The modelling process addresses flux and energy conservation issues explicitly and self-consistently, and shows the relationship between the initial modelling assumptions and the resulting predictions. The mechanisms behind the creation of uncontrollable modes in tokamak models are discussed.

A system identification procedure is applied to the large JT-60U tokamak in Japan to identify the open loop response from closed loop experiments. The measured time and frequency domain responses are predicted accurately by the model. Parametric model optimisation methods are developed and applied to further improve the model fit.

A normalised coprime factorisation \mathcal{H}_∞ controller is developed for the TCV tokamak in Switzerland using the verified linear model. Recent theory is applied to reduce the controller order significantly whilst guaranteeing *a priori* bounds on the robust stability and performance. The controller is shown to successfully track reference signals that dictate the plasma's shape, position and current. The tests used to verify this were carried out on linear and nonlinear models.

Acknowledgements

I have been honoured to work closely with a number of excellent people in my time at Imperial and it is a pleasure to acknowledge them. Firstly I thank my supervisor, David Limebeer, for his expertise, guidance and support in my work. Thanks also to Jo Lister whose infectious enthusiasm spurred me on, and whose prodigious intuition about tokamaks was always ready to call upon, whatever the distance. I would particularly like to thank John Wainwright for his modelling expertise and for his help, support, humour and encouragement above and beyond the call of duty. Thanks also to Imad Jaimoukha, probably the most acknowledged person in the Centre, for help on the control side at a number of crucial moments, and to Parag Vyas and Alfredo Portone for their discussions and advice.

During the work in Japan I also had the pleasure of working with Ryuji Yoshino, Yukiharu Nakamura and the JT-60U tokamak division at Naka, and I would like to thank them for looking after me so well and for sharing their expertise. I'm sorry about your bike, Yoshino-san.

The financial support of the EPSRC and the Centre for Process Systems Engineering is gratefully acknowledged. I also thank the British Council and JISTEC for their generous support of my work in Japan and for giving me the opportunity to explore a very beautiful country. Many thanks also to the CRPP-EPFL and JAERI for hosting my research activities.

Finally I would like to express my deep appreciation of my family and friends who carried me through the more difficult moments of this project.

Contents

1	Introduction	14
1.1	Motivation	14
1.2	Tokamaks	15
1.3	Tokamak modelling	16
1.4	Thesis outline	19
1.5	Thesis structure	21
2	Literature Review	23
2.1	Tokamak equilibrium physics	23
2.2	Tokamak modelling and identification for control	24
2.2.1	Rigid plasma displacement models	24
2.2.2	Deformable models	27
2.2.3	System identification of tokamaks	30
2.3	Modern control of tokamaks	31
3	Tokamak Modelling	33
3.0.1	The energy functions	34
3.0.2	The plasma internal energy	37

Contents	5
3.0.3 The equations of motion	37
3.0.4 Definitions of plasma bulk properties	40
3.1 Linearisation of equations	43
3.1.1 The structure circuit equation	43
3.1.2 The plasma circuit equation	45
3.1.3 The vertical force balance equation	46
3.1.4 The radial force balance equation	47
3.2 The eigenmode representation of passive structure currents	48
3.3 System outputs	50
3.3.1 Flux loops	50
3.3.2 Poloidal magnetic field probes	51
3.3.3 The output matrix, \mathbf{C}	53
3.4 The state-space model of a Tokamak	53
3.4.1 The RZIP linear model	55
4 Results for System Identification	56
4.1 Identification algorithm	56
4.1.1 Least-squares method for estimating the amplitude of specific frequencies in a signal	56
4.1.2 Frequency response estimation	58
4.2 Estimating modelling uncertainty	59
4.2.1 Error estimation for physical modelling	59
4.2.2 Error estimation for robust control	60
5 System Identification of JT-60U	64

5.1	JT-60U	65
5.2	Preliminary plasmaless model calibration	67
5.3	Plasmaless identification experiments	68
5.3.1	Experimental design	68
5.3.2	Data analysis	69
5.4	Plasmaless model optimisation	70
5.4.1	The optimisation process	70
5.4.2	Optimisation results	71
5.4.3	Possible causes for model error	72
5.5	Plasma experiments	73
5.6	Ohmically heated plasma experiments	73
5.7	Neutral beam injection (NBI) plasma experiments	74
5.8	Grey-box modelling	79
5.9	Results and model comparison	79
5.10	Closed-loop model of JT-60U	79
5.11	Discussion	85
6	Control of TCV	88
6.1	Control objectives	88
6.2	The RZIP model of TCV	89
6.2.1	Removal of poles at origin	91
6.2.2	Modelling of power supplies	92
6.3	Robust controller design	93
6.3.1	Normalised left coprime factorisation perturbations	93

6.3.2	The optimisation problem	93
6.3.3	Parameterisation of all suboptimal controllers	94
6.3.4	The controlled plant	96
6.3.5	Choice of weighting matrices	98
6.4	Normalised \mathcal{H}_∞ controller reduction	99
6.5	Controller reduction implementation	102
7	Controller Simulation Testing	105
7.1	Testing on RZIP in SIMULINK	106
7.2	Testing on the PROTEUS nonlinear tokamak simulation code . .	107
8	Conclusions and Future Work	110
8.1	Conclusions	110
8.2	Future work	112
A	Tokamak Equilibrium	118
A.1	Tokamak equilibrium	118
A.2	Flux functions	120
A.3	The Grad-Shafranov equation	122
B	Circular current loops	125
B.1	Inductance of circular current loops	125
B.2	Magnetic field due to circular current loops	126
C	JT-60U Control System	127
C.1	Control parameter estimator algorithm	127

C.1.1	Definitions	127
C.1.2	Estimator algorithm	127
C.2	The plasma controllers	128
C.2.1	Modelling of the PF coil current control loop (mode 0) . .	128
C.2.2	Modelling of the plasma control loop (modes 13, 9)	129
C.3	JT-60U feedback controller matrices	129
D	Example of a Coupled LR Circuit	131
E	Differential Operators in Cylindrical Coordinates	134

List of Figures

1.1	A diagram of a typical tokamak.	16
1.2	D-shaped plasma shape parameters: κ , elongation; δ , triangularity.	17
3.1	The plasma is represented by current-carrying elements. The cylindrical coordinate system (R, z, ϕ) is shown.	35
3.2	A plasma current element	35
3.3	Location and shape of a flux loop	51
3.4	B_{pol} probe geometry	52
5.1	A photograph of the JT-60U tokamak. The two engineers give an idea of scale.	65
5.2	A cross sectional diagram of the JT-60U tokamak.	66
5.3	Reference currents for plasmaless shot 4056.	69
5.4	Summary of ohmic discharge 35009.	75
5.5	Summary of ohmic discharge 35023.	76
5.6	Summary of neutral beam injection discharge 35561.	77
5.7	Summary of neutral beam injection discharge 35574.	78

5.8	Model comparison for control parameter R : (+) plasmaless data; (-) plasmaless model; (o) Ohmic data; (-) Ohmic nominal model; (- -) Ohmic optimised model; (x) NBI data; (-) NBI nominal model; (- -) NBI optimised model	80
5.9	Model comparison for control parameter z : (+) plasmaless data; (-) plasmaless model; (o) Ohmic data; (-) Ohmic nominal model; (- -) Ohmic optimised model; (x) NBI data; (-) NBI nominal model; (- -) NBI optimised model	81
5.10	Model comparison for control parameter I_p : (+) plasmaless data; (-) plasmaless model; (o) Ohmic data; (-) Ohmic nominal model; (- -) Ohmic optimised model; (x) NBI data; (-) NBI nominal model; (- -) NBI optimised model	82
5.11	Model comparison for control parameter X_p : (+) plasmaless data; (-) plasmaless model; (o) Ohmic data; (-) Ohmic nominal model; (- -) Ohmic optimised model; (x) NBI data; (-) NBI nominal model; (- -) NBI optimised model	83
5.12	Model comparison for control parameter δ : (+) plasmaless data; (-) plasmaless model; (o) Ohmic data; (-) Ohmic nominal model; (- -) Ohmic optimised model; (x) NBI data; (-) NBI nominal model; (- -) NBI optimised model	84
5.13	Modelled data (-) compared with real data (-) and the command signal (-).	86
6.1	TCV equilibrium 13333	90
6.2	Singular value plot of TCV RZIP model	90
6.3	Robust controller design problem	94
6.4	Lower LFT framework	96

6.5	Closed-loop configuration, single degree of freedom controller . . .	96
6.6	Response of the weighted plant	99
6.7	Plot of $\ \mathcal{F}_l(\mathbf{G}_W, \hat{\mathbf{K}})\ _\infty$ (*) against the order of the reduced controller. Closed-loop is unstable for order less than 12. The <i>a priori</i> bound on $\ \mathcal{F}_l(\mathbf{G}_W, \hat{\mathbf{K}})\ _\infty$ is shown as a (+) where stability is <i>a priori</i> guaranteed.	103
6.8	Singular value plots of the (-) $\gamma = 3.02$ controller, (- -) reduced $\gamma = 3.91$ controller (18 states)	103
6.9	Singular value plot for the weighted closed-loop plant with (-) $\gamma = 3.02$ and (- -) reduced $\gamma = 3.91$ controller	104
7.1	Results of closed loop simulation showing (:) reference and (-) RZIP simulated response.	107
7.2	Results of closed loop simulations, showing (-) the PROTEUS simulated response, (:) the reference and (- -) the SIMULINK simulated response.	108
7.3	Closed loop simulation coil voltage and current.	108
A.1	Cylindrical coordinate system. $R = 0$ is the major axis of the torus.	120
B.1	Two current carrying loops	125
D.1	A coupled LR circuit	132

Notation

a or A	a scalar
\mathbf{a} or \mathbf{A}	a vector
\mathbf{A}	a matrix
\mathbf{A}^T	the transpose of \mathbf{A}
\mathbf{A}'	the conjugate transpose of \mathbf{A}
$\mathbf{A}^\#$	the pseudo-inverse of \mathbf{A}
\dot{a}	the time derivative of a , $\frac{da}{dt}$
a_0	a at equilibrium
$\left. \frac{\partial a}{\partial b} \right _0$	$\frac{\partial a}{\partial b}$ evaluated at equilibrium
δa	the deviation of a from equilibrium, $\delta a = a - a_0$
j	$j = \sqrt{-1}$; sometimes an index
$\lambda_i(\mathbf{A})$	the i th eigenvalue of \mathbf{A}
$\sigma_i(\mathbf{A})$	the i th singular value of \mathbf{A}
$\bar{\sigma}(\mathbf{A})$	the maximum singular value of \mathbf{A}
\in	<i>is an element of</i>
$\mathbf{G}(s)$	a (matrix) transfer function
$\mathbf{G}(A, B, C, D)$	(A, B, C, D) is a state-space realisation of the transfer function $\mathbf{G}(s)$
$\mathbf{G}^*(s)$	denotes $\mathbf{G}^T(-s)$

$\ \mathbf{a}\ _2[t_1, t_2]$	the 2-norm of a signal \mathbf{a} , $\sqrt{\int_{t_1}^{t_2} \ \mathbf{a}(t)\ ^2 dt}$
$\ \mathbf{G}\ _\infty$	the infinity norm of the transfer function \mathbf{G} , $\sup_\omega \bar{\sigma}(\mathbf{G}(s))$
$\mathbb{C}^{p \times m}$	the set of complex matrices with p rows and m columns
$\mathbb{R}^{p \times m}$	the set of real matrices with p rows and m columns
\mathcal{L}_2	the finite-horizon Lebesgue space, the set of signals with a finite 2-norm
\mathcal{H}_∞	the class of systems for which \mathbf{G} is analytic in the open right-half plane and for which $\ \mathbf{G}\ _\infty$ is finite
\mathcal{R} (prefix)	real and rational

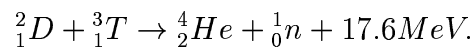
In Chapter 6, plain uppercase A will denote a matrix.

Introduction

1.1. Motivation

As a source of power, nuclear fusion has a number of attractive features. The fuels are abundant, there are no long-term waste management issues and it is inherently safe. The nuclear fusion reaction also does not contribute to the emission of gases causing the greenhouse effect, or acid rain. At the time of writing, the tokamak is the most promising route to a viable fusion reactor.

Nuclear fusion occurs when light atoms fuse and energy is released. The reaction which appears most promising as a long-term source of energy occurs when the nuclei of hydrogen isotopes deuterium (D) and tritium (T) combine, with the resultant release of helium, a neutron, and energy, described by:



The helium, deuterium and tritium nuclei are all positively charged, therefore to obtain the nuclear reaction the energies of the incident particles must be high enough to overcome the Coulomb barrier¹. A commercial reactor would use heat

¹The Coulomb barrier in this case is the energy required to overcome the mutual repulsion of the positively charged nuclei, although this is reduced by the quantum tunnelling effect.

generated by the neutrons, slowed down by a blanket of denser material, to generate electricity. The blanket would contain lithium that would react with the neutrons to form tritium. Thus lithium and deuterium are the primary fuels.

At these high temperatures, the atomic nuclei are dissociated from their electrons resulting in a mixture called a plasma, often referred to as the fourth state of matter.

Accurate models of the dynamic response of tokamak plasmas are needed for the design of multi-variable model-based tokamak controllers. A simple, validated tokamak model derived from first principles would also reveal the relative importance of various physical effects. The resulting improved controller design and physical understanding would enable existing tokamaks to extend their operating regimes and would facilitate the design of next-generation tokamaks.

1.2. Tokamaks

The tokamak was conceived by the Russian scientists Tamm and Sakharov, winners of the Nobel Physics and Peace Prizes respectively. A tokamak² is a toroidal device (see Figure 1.1) that uses magnetic fields to confine a similarly shaped, hot plasma (typically up to 10^8K). The vacuum vessel contains a plasma at typically some five orders of magnitude below atmospheric density. This method of confinement exploits the fact that plasmas are made up of free electrons and ions. As a result the plasma can be confined using electromagnetic forces generated by external fields. This external magnetic field has two components. The large toroidal field is produced by a set of poloidally wound coils equally spaced around the vacuum vessel and the smaller poloidal field comes from the induced plasma current. The resultant field is helical as shown schematically in Figure 1.1.

Plasma shape parameters are defined in Figure 1.2. In this diagram, R is the

²from the Russian '*toroidalnaya kamera magnitnaya katushka*', literally 'toroidal chamber, magnetic coils'

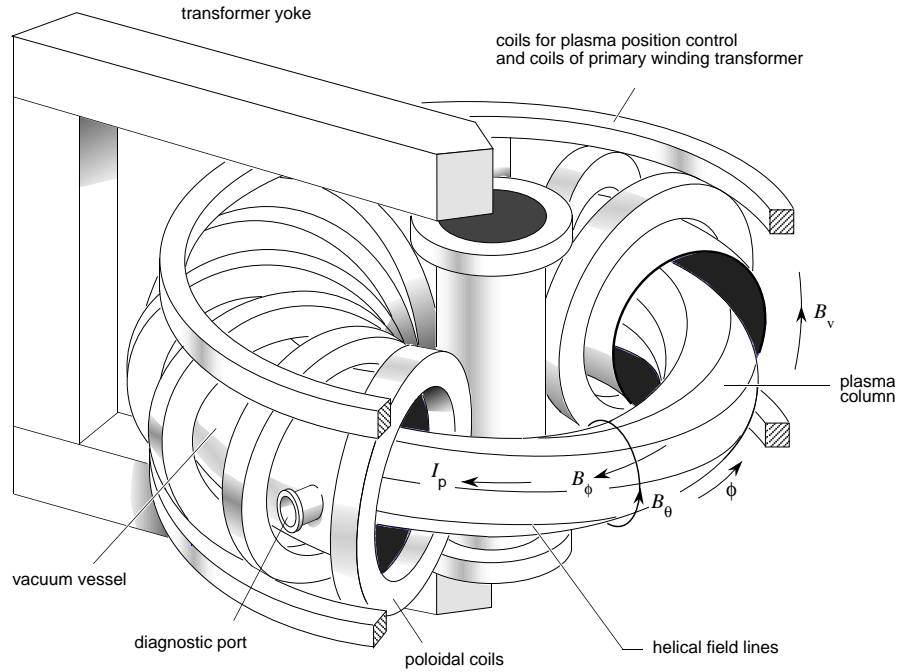


Figure 1.1: A diagram of a typical tokamak.

radial distance from the tokamak axis to halfway across the plasma width (the major radius). R_m is the radial distance to the highest point of the outer plasma flux surface. We define a as half the width of the plasma, and b as half the height. From these values we calculate δ and κ , the plasma triangularity and elongation, as described in the figure.

A tokamak large enough to act as a reactor would have a major radius of order 8m, a minor radius of order 3m and a plasma current of approximately 20MA. The largest experimental tokamak now in use has a major radius of 3m, a minor radius of 1m and a plasma current of up to 7MA.

1.3. Tokamak modelling

Current tokamak control methods perform satisfactorily but for next generation tokamaks we require controllers with guaranteed performance characteristics. The performance of control systems designed using model-based methods is limited by

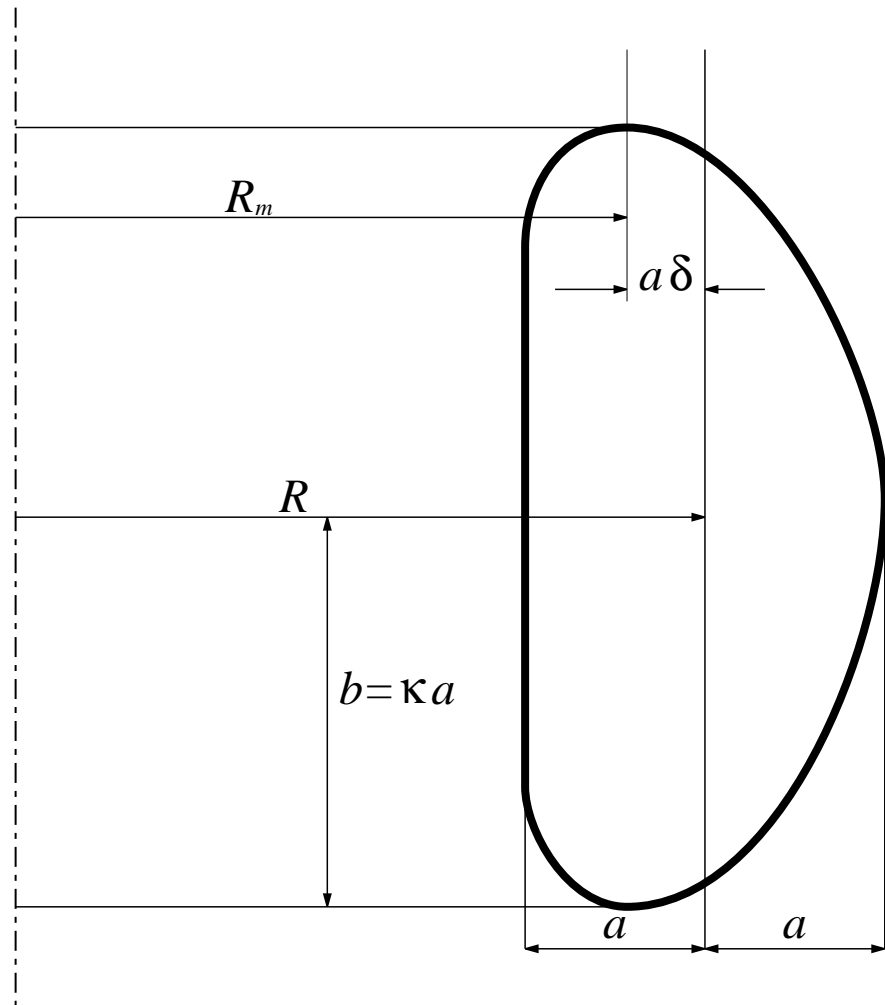


Figure 1.2: D-shaped plasma shape parameters: κ , elongation; δ , triangularity.

the quality of model used. In our context, we require a model to have a number of attributes. Since the intended model application is control, we require the model to make sufficiently accurate statements about the future behaviour of the system's inputs and outputs. A model derived from physical principles and assumptions must generate a set of rules with which we can make generalisations about the behaviour of the tokamak. Comparisons with real data then allow us to make judgements about the validity of the original physical assumptions. Given two equivalent models of differing complexity, it is more practical and preferable aesthetically, to choose the less complex model. Thus we desire a model to be as compact as possible.

Models can be classified into three groups depending on the level of physical interpretation contained:

- Black-box modelling

A black-box model assumes only a causal relationship between the system input-output data set. No assumptions are made about the system internal structure. The system identification experiments described in this thesis yield black-box models. Our level of confidence in the model equals our level of confidence in the data, but the model generates little meaningful physical insight.

- White-box modelling

Also called *a priori* or physical modelling, we use knowledge of the internal form of the system to hypothesise an input-output relationship, which is falsifiable against further data.

- Grey-box modelling

A grey-box model is parametric; some internal form is assumed but certain parameters are adjusted until the discrepancy between observed and predicted data is minimised.

The class of modelling technique employed will depend on the level of knowledge of the modelled system. Since we wish to examine the quality of our assumptions about tokamak plasma behaviour, this thesis will explore all three types of models.

The basic characteristics of tokamak equilibrium, as described by the Grad-Shafranov equation, are well understood [1] and the theory is relatively accessible [2]. In order to model the gross dynamic behaviour it is possible to make a number of approximations, that permit the creation of simple white-box models accurate enough to provide a basis for modern controller design. Recent techniques in system identification as applied to tokamaks [3] allow the identification of accurate black-box tokamak models that act as exacting constraints on the range of possible models. Grey-box modelling proves indispensable in determining the validity of particular physical assumptions.

1.4. Thesis outline

A lumped-parameter model is derived using the established processes of classical mechanics. For the purposes of model-based controller design, this model can be linearised about any prescribed equilibrium state. As compared with the current art, this model has several distinct features. To begin, flux and energy conservation issues are treated explicitly and self-consistently. In [4], for instance, plasma profile parameters are considered as disturbances, which the authors acknowledge is not self-consistent. Previous incarnations of the RZIP model [5] have also not considered conservation laws in a self-consistent manner. This was first addressed in our previous work [6], where a Lagrangian approach to tokamak modelling was introduced.

The modelling theory presented here is of particular value, because it shows clearly the relationship between the initial assumptions and the final model. For instance, it becomes obvious that the adiabatic approximation is a natural result of assuming a massless plasma. The modelling presented in this paper considers fully the

effects of plasma resistance, showing how to incorporate resistance and mass into the model from the initial stages, if required. The necessity of current ramping to overcome plasma resistance is explained in simple terms, as is the creation of uncontrollable modes when a superconducting plasma is assumed. Also, it becomes clear why the use of flux coordinates becomes problematic when plasma resistance is introduced.

By rigorously deriving a simple linear tokamak equilibrium response model from a clear set of assumptions, comparisons with data from open-loop system identification experiments on tokamaks become possible. With this approach we intend to clearly demonstrate the validity or otherwise of the assumptions used to derive this and other models. By carefully examining the predictive quality of these assumptions, we can assess the feasibility of control studies based on the model. Also, we expect that directions for improvement will be clarified.

Open-loop system identification experiments have been performed on TCV [5], [3]. The identified model was compared with the CREATE-L and RZIP models. Both models were found to be reasonably accurate, but there were a number of issues raised by the work. Also the method used to quantify the model error was ad-hoc. It is shown that the positive TCV results are transferable to larger and hotter tokamaks such as JT-60U. The plasma response identification experiments were carried out with both Ohmically heated discharges and discharges with additional neutral beam injection heating.

High-order \mathcal{H}_∞ controllers can present implementation problems. The usual approach is to design the \mathcal{H}_∞ controller about a reduced-order model. In this thesis a reduced-order normalised coprime factor controller is developed for TCV that exploits results presented in [7]. It is shown that this controller extends the performance of the existing PID schemes [8], [9]. This approach guarantees both the stability of the closed-loop (via an *a priori* condition) and the closed-loop performance via an *a priori* performance bound [7].

The theory in [7] is applied to the full-order \mathcal{H}_∞ controller developed for TCV, reducing the controller order from 76 to 18 without a significant loss of performance or robustness. Successful closed-loop tests are performed with the PROTEUS nonlinear tokamak simulation code. The remaining verification step will involve hardware tests on the TCV machine itself.

1.5. Thesis structure

This first part of this thesis is concerned with the modelling of tokamak systems as it relates to plasma position and shape control, using both *a priori* and identification methods. Chapter 2 describes some current efforts reported in the literature to tackle this problem. In Chapter 3 a simple tokamak model is derived that is suitable for control purposes.

Model verification is achieved by comprehensive comparison against experimental data. To extend our knowledge of the subject we use a number of techniques, described in Chapter 4. In Chapter 5, open-loop frequency response identification experiments performed on the JT-60U tokamak both with and without plasma, for two different types of plasma heating, are detailed and discussed. This series of experiments act as a stringent test of the tokamak model presented, leading us to consider the validity of some the modelling assumptions.

The second part of the thesis is concerned with the control of TCV. Many efforts have been made to implement \mathcal{H}_∞ and model predictive control strategies on tokamaks. Chapter 2 reviews the literature describing some of the present work on tokamak control. The development of an \mathcal{H}_∞ controller is presented in Chapter 6 along with the controller reduction methodology. In Chapter 7 the reduced order controller is tested on the linear model used for design and the nonlinear PROTEUS tokamak model.

The content of the thesis as a whole is discussed in Chapter 8, where conclu-

sions are drawn from the work described. Directions for future research are also proposed in this chapter.

Literature Review

2.1. Tokamak equilibrium physics

The Grad-Shafranov equation describes the shape and current profile of a toroidally symmetric plasma in an externally applied magnetic field. [1] considers the form the plasma equilibrium may take in a toroidal tokamak with conducting casing and an inhomogeneous magnetic field produced by poloidal field coils. A more accessible account of the tokamak equilibrium equations is to be found in reference [2]. The equilibrium equations are found by considering (in the absence of resistive dissipation) the force balance between thermodynamic pressure and magnetic force,

$$\mathbf{j} \times \mathbf{B} = \nabla p$$

subject to toroidal symmetry, where \mathbf{j} is the current density, \mathbf{B} is the magnetic field and p is the pressure. From this it follows immediately that

$$\mathbf{B} \cdot \nabla p = 0,$$

which shows the magnetic surfaces are surfaces of constant pressure, and that

$$\mathbf{j} \cdot \nabla p = 0,$$

which shows the lines of current lie on the magnetic surfaces. A more complete discussion of tokamak equilibrium is presented in Appendix A.

2.2. Tokamak modelling and identification for control

The performance of a modern control system is limited by the open-loop plant model used in the design phase. With this in mind a number of linear tokamak plasma response models are discussed.

2.2.1. Rigid plasma displacement models

The class of models that assume the plasma current density profile is unchanged under spatial translation are called rigid plasma displacement models. The plasma is pictured to move as a unit vertically or radially without changing its cross-section. Although the current profile is fixed, in some models the total plasma current is allowed to change, and as such each element of the plasma current profile changes proportionally. Since these models treat the plasma as a unit, simple force balance considerations can be invoked to determine the movement of the plasma. Contrast this with the deformable class of models, where the plasma current profile is allowed to vary, generally in accordance with the Grad-Shafranov equation (A.11). Because of the severe restriction placed on plasma behaviour, the rigid plasma displacement class of models is the simplest to implement.

One model that disregards all but the vertical motion of the plasma is presented in [10]. The plasma vertical position response is modelled by a massless single-filament plasma, that includes the response of the tokamak vessel and coils. An eigenmode representation of the vessel eddy currents is used (see Section 3.2,) which has become a common approach. The model is essentially the vertical force balance equation and the circuit equation for the vessel. The stability properties of the model are analysed, and two critical indices are defined to characterise

the stability properties of the plasma. A crude single-filament model is adequate for the control problem studied, and is instructive due to its simplicity. However, when a subsystem is reduced using the vessel eigenmode model reduction method, there are no guaranteed stability properties of the whole system.

Numerical studies are done to include the nonlinear effect of the power supply limits. The open-loop plasma vertical position growth rate on the D-IIID tokamak is measured directly. This is used to determine the bandwidth requirement of the power supply system. It is a relatively crude test of the model, but sufficiently strong for the control problem studied. Measuring the open-loop response is desirable over the closed-loop response as it is a more direct test of the open-loop model. A study of the poloidal field coil positioning is also made and it is concluded that inboard coils are desirable to achieve vertical stability.

Using these results, improvements to the D-IIID control system were made. Further experimental results and improvements are detailed in [11]. The single-filament model is validated, and improvements to the control system were made to allow control of a $\kappa = 2.5$ plasma. It was confirmed that the inboard coils are necessary for fast control (*i.e.* control of high growth rate plasmas).

The simple single-filament model is extended in [12] to include multi-pole magnetic fields, *i.e.* the gradients of magnetic fields are described. These corrections to the simple model allow the model to perform adequately in comparison with other models. In particular a comparison with the PROTEUS nonlinear tokamak simulation code was made. The vertical plasma position growth rate was compared as a crude measure (the only unstable eigenmode). A controller designed using the extended model functioned within specifications on the nonlinear PROTEUS code. All comparisons were made in the time-domain.

A simpler model is proposed in [5]. This paper presents the technique and results of an open-loop frequency response estimation of TCV (using work in [3]). The identified data is compared with the (deformable plasma) CREATE-L model,

showing good agreement. This is a more useful test than the closed-loop comparison discussed earlier.

The RZIP model, a simple, linear, discretised-plasma model based on perturbing the vertical and radial force balance and the plasma and structure circuit equations, is also presented. The RZIP model has a transparent structure in order to understand the reasons for good model agreement - *i.e.* which physical assumptions are necessary or useful. The plasma is assumed to behave as a toroidally symmetric body, with fixed current distribution about the plasma centre, capable of vertical motion and radial deformation. The plasma current distribution and tokamak structure are discretised into elements. Changes in internal inductance $(l_i)^1$, and the poloidal beta $(\beta_p)^2$ are handled as disturbances, as in the CREATE-L model. The RZIP model agrees equally well with the data presented.

A grey-box modelling approach is presented, where a set of purely plasma-related parameters in the RZIP model are floated to minimise a cost function compared with the experimental data, in the frequency domain. This gives valuable information on the quality of the RZIP model and its weaknesses. However the approach suffers from the ad-hoc nature of the cost function chosen, and from the inconsistencies in the structure of the RZIP model.

In [13] a plasma response model similar to RZIP in nature is described, in the sense that it is derived from the perturbed force balance equations and circuit

¹For a circular cross-section plasma we define l_i , the plasma internal inductance per unit length, as [2]

$$l_i = \frac{\bar{B}_\theta^2}{B_{\theta a}^2} = \frac{2 \int_0^a B_\theta^2 r dr}{a^2 B_{\theta a}^2},$$

where B_θ is the poloidal magnetic field, a is the minor radius of the plasma, and r is the minor radius coordinate.

²The efficiency of confinement of plasma pressure by the magnetic field can be simply measured by the ratio between the plasma and magnetic pressures,

$$\beta = \frac{p}{B^2/2\mu_0}.$$

Clearly there are many specific ways of defining β . The poloidal beta, β_p , uses an average pressure divided by the poloidal magnetic field pressure

equations. It also admits variations in β_p and l_i . The model is validated in the time-domain on the D-IIID tokamak, and applied to the design of plasma position and shape controllers, with some success, although there were problems predicting the growth rate of some plasma discharges.

2.2.2. Deformable models

The second class of linear models is the deformable models. These models generally solve for Ψ in the Grad-Shafranov equation (A.11), to calculate the plasma equilibrium response to all possible perturbations in the coil currents. Because of the effort needed to numerically solve the equilibrium equation each time, these models are very computationally expensive.

A deformable model is described in [4]. The aim of this paper is to present a simple, reliable plasma response model suitable for control purposes. The CREATE-L model presented is essentially the Grad-Shafranov equation perturbed around a particular equilibrium. This is achieved by linearising the PROTEUS model about an operating point. As such it is a deformable, *a priori* model. It admits plasma current, internal inductance (l_i), and the poloidal beta (β_p) as degrees of freedom, treating the last two as disturbances. The corresponding changes in plasma current profile are constrained by magnetic flux conservation considerations.

The most significant energy term is that stored in the magnetic field. The macroscopic kinetic energy, radiative dissipation, and effects of nuclear reactions are neglected. Instead, work done by pressure and the exchange between toroidal and poloidal magnetic energy are considered. The results presented in [4] for example assume the plasma resistance is negligible.

The model is compared against two linear plasma response models: the rigid current displacement model (TCV configuration) and a similar model CORSICA (ITER³ configuration). Also comparisons in the time-domain are made with the

³International Thermonuclear Experimental Reactor

nonlinear codes TSC and MAXFEA, using square pulse voltage injection into the PF coils, and using β_p and l_i disturbances. The agreement was good between models for the PF coil response, but merely satisfactory for the response to the β_p and l_i disturbances.

The CREATE model is also validated experimentally on the TCV tokamak. The experiments and comparison are performed in closed-loop, and showed good agreement, although the closed-loop response is dominated by the power supply responses.

The CREATE model, as it is related to PROTEUS, has a wealth of physical intuition and interpretation associated with it. However the complex form the model takes means that it is difficult to clearly examine the link between physical assumptions and experimental agreement, and in so doing glean extra information from the experiments.

Similar in essence to the CREATE model is that proposed in [14]. The model is intended to approximately conserve flux, and takes the plasma current as constant. The model is derived by perturbing the full equilibrium equations to give a deformable plasma model.

In [9] the formulation of another non-rigid plasma response model, the Deformable Plasma Model (DPM) is described. The growth rates of TCV plasmas are predicted using three codes; the DPM, a rigid displacement model (the same one used in [15], called RCDM) and the NOVA-W linear stability code. The rigid displacement model used (RCDM) contains simple vertical force balance only, and vessel and coil currents. Good agreement is found between the DPM and NOVA-W predictions. Differences in predictions between the RCDM and the DPM are marked for high elongation and high triangularity plasmas. This is to be expected given the known inadequacy of the RCDM model.

The DPM model is derived by directly perturbing the Grad-Shafranov equation to give a perturbed equilibrium with perturbed poloidal flux Ψ and perturbed source

functions p and f . The resulting equation can be solved by iterative methods as usual, imposing ideal MHD constraints of flux conservation, fixed safety factor q^4 , and adiabaticity. One must compute a perturbed equilibrium for all conceivable coil current and vessel current perturbations to give a complete plasma model. This is very computationally intensive, and must be redone for each different plasma equilibrium.

The stability of the closed loop system is analysed as a function of PD controller gains, the size of the stable domains in the gain space being calculated for the DPM and RCDM for various plasma shapes. The two models give unequal stable regions in gain space, but both are consistent with the particular test TCV plasma, a D-shaped plasma with $\kappa = 2.55$.

Further experimental comparisons are made in [16]. Growth rate predictions from DPM and a different rigid model, RPM (Rigid Plasma Model, [17]) are compared to experimental values for plasma shapes in the ranges $1.2 \leq \kappa \leq 2.2$ and $-0.3 \leq \delta \leq 0.6$. Again, the stability of the closed loop vertical position control system is examined theoretically and experimentally. It is found that the RPM underestimates the open loop growth rate for large triangularity and overestimates the stable region in controller gain space, while the DPM gives good agreement with experiment. Like the RCDM, the RPM is simply the structure circuit equation plus the vertical force balance equation. As such it will suffer from the same problems as the RCDM.

The DINA code [18] is a comprehensive nonlinear axisymmetric free-boundary

⁴In general terms the safety factor q is a measure of the plasma MHD stability [2]. In axisymmetric equilibrium each magnetic field line has a q value. The field line follows a helical path around the torus on some magnetic surface. If at some toroidal angle ϕ the field line has a certain position in the poloidal plane, it will return to that position in the poloidal plane after the change of toroidal angle $\Delta\phi$. The q -value for this field line is defined by

$$q = \frac{\Delta\phi}{2\pi}.$$

Thus if a magnetic field line returns to its starting position after one rotation around the torus, then $q = 1$. If it moves more slowly in the poloidal direction then it has a higher value of q .

Grad-Shafranov equilibrium code that models both resistive and transport effects self-consistently. There is facility for modelling neutral beam and radio-frequency heating or current drive, α -particle injection, pressure driven bootstrap current and pellet injection.

2.2.3. System identification of tokamaks

As well as the deformable and rigid plasma models, we can identify the actual response of a plasma, using system identification techniques.

In [3] we see an \mathcal{H}_∞ system identification technique presented, applicable to MIMO systems such as tokamaks. The technique allows the identification of an open-loop response from closed-loop data. This technique was applied to the TCV tokamak to give a linear black-box model of the plasma response to the PF coil voltages, via six control parameters. The PF coils were stimulated with a multisine signal. A least-squares method was used as a generalised discrete Fourier transform to obtain the frequency response estimates from the time domain data. Then, a nonlinear algorithm was used to identify a high-order non-causal finite-impulse response model, which was then reduced to a low-order infinite-impulse response model by a Hankel model reduction technique and MISO Chebycheff reduction.

Closed loop experiments were performed, and the open-loop system was identified from these experiments. The identified model was compared to a rigid current displacement model, and two types of CREATE-L model (limited and diverted).

In this way a frequency domain open-loop response identification technique is successfully applied to the TCV tokamak, which is a much stronger test of the physics models than time-domain or straightforward growth rate comparisons. However, the identified model included the power supplies to the PF coils which tend to dominate the response. Also the plasma was relatively small and cold, leaving questions about possible hot plasma edge-currents unexplored.

In [19] the experiments were repeated on the DINA simulation code. The responses were well modelled for limited and diverted plasmas. The most significant difference was in the penetration time of the magnetic flux, leading to a delayed onset of saw-toothing in the DINA simulation. Nonlinear effects observed in a few experiments, namely instability arising from the over-stimulation of the equilibrium, was also observed in the simulations.

2.3. Modern control of tokamaks

Linear quadratic control schemes have been investigated in some detail for ITER. In [20] a multi-variable LQG method is applied to control the gap between the plasma and tokamak structure. In linear and nonlinear simulations, decoupling and tracking are found to be satisfactory. In [21], a linear quadratic scheme is applied to the Burning Plasma Experiment (BPX) design which simulates a tokamak operating in a fusion regime. The results show that modifications to the safety factor profile affect the plasma temperature and density profile by transport effects, and that fusion events further complicate control efforts. As such, under these conditions, some profile modelling is found to be necessary.

A mixed PD- \mathcal{H}_∞ controller has already been designed and tested on COMPASS-D [22]. In this work, an analogue PD controller is used to stabilise the tokamak plasma vertical position before implementing a digital \mathcal{H}_∞ controller around the stabilised plant. In [23] a digital \mathcal{H}_∞ controller is used to reduce the 600Hz noise found in the system and was found to stabilise the plasma at the required operating point. The model used to design the controller was found from closed-loop system identification experiments.

This mixed control architecture was developed and successfully implemented on the TCV machine [24]. The control scheme was based on the CREATE-L model presented in [4]. The controller was tested on a challenging equilibrium on the PROTEUS nonlinear time-evolution tokamak simulation code, which is closely

related to CREATE.

In [25], a multi-variable normalised coprime factor \mathcal{H}_∞ controller is designed using a simple single-filament model of the DIII-D tokamak. However some problems were encountered with controlling plasma shape parameters. The authors conjecture that a model only slightly more sophisticated than the rigid radial response model used is necessary for effective multi-variable controller design.

\mathcal{H}_∞ control design work has also been investigated on ITER [26], [27]. In [26], \mathcal{H}_∞ and μ -synthesis techniques are used to address issues including input signal constraints (for example power limits). Model reduction of high-order systems such as tokamaks is discussed in [27], where Krylov subspace techniques are employed to reduce the tokamak model order before \mathcal{H}_∞ control design is performed.

Tokamak Modelling

“A good notation has a subtlety and suggestiveness which at times makes it seem almost like a live teacher.”

Bertrand Russel

The aim of this chapter is present a new approach for developing a dynamic model of the tokamak using established arguments from Hamiltonian mechanics [28]. The derivation builds on the author’s previous work given in [6]. The new approach permits revealing insights into the structure of the tokamak modelling problem. From the nonlinear model a linear model is derived that is similar to the RZIP model [5]. It is hoped that the approach presented here will provide a firmer theoretical basis. The main components of the model are the poloidal field coils, the passive structure, which carries eddy currents, and the plasma. The poloidal field coils are driven by external voltage sources, while the eddy currents in the passive structure are electromagnetically induced. A cylindrical coordinate system is used, with R the radial coordinate, z the vertical coordinate, and ϕ the angular coordinate describing rotation around the z -axis (see Figure 3.1). When deriving the model, we will make the following simplifying assumptions:

- The system is symmetric around the z -axis (axisymmetry);
- Any poloidal currents are ignored;
- The tokamak structure will be represented by a finite set of toroidal circuits.

We also assume that:

- These circuits are fixed in space and have finite resistance;
- The toroidal currents in the structure may vary in time;
- The plasma is represented by a finite number of axisymmetric current carrying elements that have a circular cross-section (see Figure 3.1). In addition, the filaments will each:
 - carry current that may vary in time;
 - be free to move axisymmetrically;
 - have finite mass and resistance that are assumed constant.

3.0.1. The energy functions

In the next phase of the modelling process we will select the generalised coordinates and introduce the external voltages into the potential energy function.

Consistent with the modelling assumptions, we define the generalised coordinates \mathbf{q} via

$$\dot{\mathbf{q}} = \begin{bmatrix} \mathbf{I}_e \\ \mathbf{I}_s \\ \dot{\mathbf{r}} \end{bmatrix}.$$

The vector \mathbf{I}_e contains the currents in the plasma elements, \mathbf{I}_s is a vector of structure currents and $\mathbf{r} = \begin{bmatrix} R \\ z \end{bmatrix}$ is a vector of position coordinates associated with the plasma current elements.

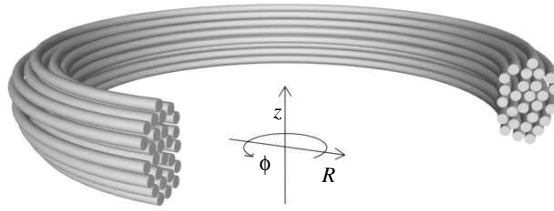


Figure 3.1: The plasma is represented by current-carrying elements. The cylindrical coordinate system (R, z, ϕ) is shown.

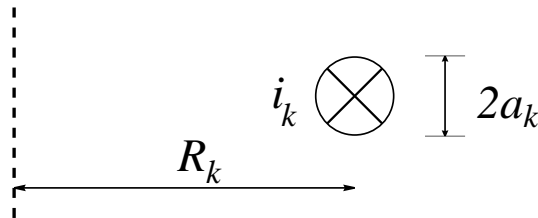


Figure 3.2: A plasma current element

Next, we introduce the inductance-mass matrix:

$$\mathbf{T}(\mathbf{q}) = \begin{bmatrix} \mathbf{L}_e & \mathbf{M}_{es} & 0 \\ \mathbf{M}'_{es} & \mathbf{L}_s & 0 \\ 0 & 0 & \mathbf{m}_e \end{bmatrix}$$

in which \mathbf{L} and \mathbf{M} are the self and mutual inductance matrices. Subscripts s and e refer to the structure and plasma elements respectively as above. The matrices \mathbf{L}_e and \mathbf{M}_{es} are functions of position, because the plasma current elements are free to move axisymmetrically. The structure self-inductance matrix, \mathbf{L}_s , is constant. Note that $\mathbf{M}_{se} = \mathbf{M}'_{es}$. The constant diagonal mass matrix, \mathbf{m}_e , contains the mass of each plasma current element.

The input vector is given by:

$$\mathbf{U} = \begin{bmatrix} \mathbf{V}_e \\ \mathbf{V}_s \\ 0 \end{bmatrix}$$

where \mathbf{V}_e is a vector of effective voltages applied to each element (for example by ion injection) and \mathbf{V}_s is the vector of externally applied poloidal field coil voltages.

The resistance matrix is defined as

$$\mathbf{\Omega} = \begin{bmatrix} \mathbf{\Omega}_e & 0 & 0 \\ 0 & \mathbf{\Omega}_s & 0 \\ 0 & 0 & 0 \end{bmatrix}.$$

The generalised kinetic energy is given by:

$$\mathcal{T} = \frac{1}{2} \dot{\mathbf{q}}' \mathbf{T} \dot{\mathbf{q}} \tag{3.1}$$

and the generalised potential is:

$$\mathcal{V} = -W - \mathbf{q}'\mathbf{U} + \frac{1}{2} \frac{\mathrm{d} \left(\int_{\mathbf{q}(t_0)}^{\mathbf{q}(t)} \int_{\mathbf{q}(t_0)}^{\mathbf{q}(t)} \mathrm{d}\mathbf{q}' \mathbf{\Omega} \mathrm{d}\mathbf{q} \right)}{\mathrm{d}t}, \quad (3.2)$$

in which W represents the plasma's internal energy.

As usual, the Lagrangian is given by:

$$\mathcal{L} = \mathcal{T} - \mathcal{V} = \frac{1}{2} \dot{\mathbf{q}}' \mathbf{T} \dot{\mathbf{q}} + W + \mathbf{q}'\mathbf{U} - \frac{1}{2} \frac{\mathrm{d} \left(\int_{\mathbf{q}(t_0)}^{\mathbf{q}(t)} \int_{\mathbf{q}(t_0)}^{\mathbf{q}(t)} \mathrm{d}\mathbf{q}' \mathbf{\Omega} \mathrm{d}\mathbf{q} \right)}{\mathrm{d}t}. \quad (3.3)$$

The term containing $\mathbf{\Omega}$ is the total energy dissipated from time t_0 to t ; it is essentially an integral form of Ohm's law. In the Hamiltonian formulation, the dissipation term must be included in \mathcal{V} and not as a separate power dissipation function.

3.0.2. The plasma internal energy

We will see later that the internal energy W varies as $\mathbf{R}\mathbf{I}_e^2$. As such we can express it as

$$W = \frac{\mathbf{q}' \mathbf{E} \mathbf{q}^2}{2} \quad (3.4)$$

where \mathbf{E} is a constant matrix.

This representation is chosen for convenience when forming the Hamiltonian.

3.0.3. The equations of motion

Using the above we can now express the Lagrangian (3.3) as

$$\begin{aligned} \mathcal{L} = & \frac{1}{2} \dot{\mathbf{q}}' \mathbf{T} \dot{\mathbf{q}} + \frac{\mathbf{q}' \mathbf{E} \mathbf{q}^2}{2} + \mathbf{q}'\mathbf{U} \\ & - \frac{1}{2} \frac{\mathrm{d} \left(\int_{\mathbf{q}(t_0)}^{\mathbf{q}(t)} \int_{\mathbf{q}(t_0)}^{\mathbf{q}(t)} \mathrm{d}\mathbf{q}' \mathbf{\Omega} \mathrm{d}\mathbf{q} \right)}{\mathrm{d}t}. \end{aligned} \quad (3.5)$$

To form the Hamiltonian, via the correct Legendre transformation, the generalised momenta are computed next:

$$\mathbf{p} = \frac{\partial \mathcal{L}}{\partial \dot{\mathbf{q}}}$$

giving

$$\mathbf{p} = \mathbf{T}\dot{\mathbf{q}} + \mathbf{q}'\mathbf{E}\dot{\mathbf{q}}. \quad (3.6)$$

The Hamiltonian is given by

$$\mathcal{H} = \mathbf{p}'\dot{\mathbf{q}} - \mathcal{L}$$

or equivalently:

$$\begin{aligned} \mathcal{H} = & \frac{1}{2}\dot{\mathbf{q}}'\mathbf{T}\dot{\mathbf{q}} + \frac{1}{2}\mathbf{q}'\mathbf{E}\dot{\mathbf{q}}^2 - \mathbf{q}'\mathbf{U} \\ & + \frac{1}{2} \frac{\mathrm{d} \left(\int_{\mathbf{q}(t_0)}^{\mathbf{q}(t)} \int_{\mathbf{q}(t_0)}^{\mathbf{q}(t)} \mathrm{d}\mathbf{q}'\Omega \mathrm{d}\mathbf{q} \right)}{\mathrm{d}t}. \end{aligned} \quad (3.7)$$

We now eliminate $\dot{\mathbf{q}}$ using (3.6), to obtain the Hamiltonian in terms of \mathbf{p} , \mathbf{q} and t :

$$\begin{aligned} \mathcal{H}(\mathbf{p}, \mathbf{q}, t) = & \frac{1}{2}\mathbf{p}'[\mathbf{T} + \mathbf{q}'\mathbf{E}]^{-1}\mathbf{p} - \mathbf{q}'\mathbf{U} \\ & + \frac{1}{2} \frac{\mathrm{d} \left(\int_{\mathbf{q}(t_0)}^{\mathbf{q}(t)} \int_{\mathbf{q}(t_0)}^{\mathbf{q}(t)} \mathrm{d}\mathbf{q}'\Omega \mathrm{d}\mathbf{q} \right)}{\mathrm{d}t}. \end{aligned} \quad (3.8)$$

The relation

$$\dot{\mathbf{p}} = -\frac{\partial \mathcal{H}}{\partial \mathbf{q}} \quad (3.9)$$

gives

$$\begin{aligned} \frac{\mathrm{d}(\mathbf{T}\dot{\mathbf{q}} + \mathbf{q}'\mathbf{E}\dot{\mathbf{q}} + \Omega\mathbf{q})}{\mathrm{d}t} = & \mathbf{U} + \frac{\mathbf{E}\dot{\mathbf{q}}^2}{2} + \frac{1}{2}\dot{\mathbf{q}}'\frac{\partial \mathbf{T}}{\partial \mathbf{q}}\dot{\mathbf{q}} \\ & - \frac{1}{2} \frac{\mathrm{d} \left(\int_{\mathbf{q}(t_0)}^{\mathbf{q}(t)} \mathrm{d}\mathbf{q}'\Omega \right)}{\mathrm{d}t}, \end{aligned} \quad (3.10)$$

which is the required equation of motion.

This equation can now be expanded into four vector equations. The equation for

\mathbf{I}_e is:

$$\frac{d(\mathbf{L}_e \mathbf{I}_e + \mathbf{M}_{es} \mathbf{I}_s + \mathbf{R} \mathbf{E} \mathbf{I}_e)}{dt} + \mathbf{\Omega}_e \mathbf{I}_e = \mathbf{V}_e, \quad (3.11)$$

which is essentially a statement of Kirchoff's voltage law for the plasma elements.

Similarly, we have Kirchoff's voltage law for the structural and poloidal circuits, giving the equation for \mathbf{I}_s :

$$\frac{d(\mathbf{L}_s \mathbf{I}_s + \mathbf{M}_{se} \mathbf{I}_e)}{dt} + \mathbf{\Omega}_s \mathbf{I}_s = \mathbf{V}_s. \quad (3.12)$$

The remaining equations are force balances in the R and z -directions respectively.

For \mathbf{R} we have:

$$\frac{d(\mathbf{m}_e \dot{\mathbf{R}})}{dt} = \frac{1}{2} \mathbf{I}_e' \frac{\partial \mathbf{L}_e}{\partial \mathbf{R}} \mathbf{I}_e + \mathbf{I}_s' \frac{\partial \mathbf{M}_{se}}{\partial \mathbf{R}} \mathbf{I}_e + \frac{\mathbf{E} \mathbf{I}_e^2}{2} \quad (3.13)$$

and for z :

$$\frac{d(\mathbf{m}_e \dot{z})}{dt} = \frac{1}{2} \mathbf{I}_e' \frac{\partial \mathbf{L}_e}{\partial z} \mathbf{I}_e + \mathbf{I}_s' \frac{\partial \mathbf{M}_{se}}{\partial z} \mathbf{I}_e. \quad (3.14)$$

We conclude this section with a number of observations:

- In the case that \mathcal{H} is independent of a particular coordinate, the corresponding canonical momentum will be conserved (see (3.9), and by Noether's theorem, see [28], Section 12-7). In the same way, if \mathcal{H} is time invariant, the associated system is conservative.
- If \mathbf{U} and $\mathbf{\Omega}$ are both zero, the magnetic fluxes \mathbf{p}_e and \mathbf{p}_s will remain constant. This situation is analogous to a system of purely inductive closed loops. More specially $\mathbf{V}_e = 0$, $\mathbf{\Omega}_e = 0$ implies constancy of the magnetic flux associated with the plasma model. These assumptions result in the well-known ideal MHD situation, in which lines of constant flux are 'frozen' in the plasma. Since some plasma resistance will occur in practice, the

$\Omega_e = 0$ assumption is generally false. A distinguishing feature of the model we present is the introduction and consideration of resistance terms in the plasma model from the beginning.

- Replacing the generalised coordinates with $-\mathbf{p}$ gives an equivalent model, because of the invariance properties of the canonical equations. In the case of a non-resistive plasma, one may use the fluxes associated with the plasma elements as generalised coordinates. Since one cannot express the resistive form of Ohm's law in terms of flux, this necessitates a loss of generality. As a result, plasma models that describe plasma behaviour in terms of plasma flux functions must necessarily neglect plasma resistance effects.
- Also evident from the \mathbf{I}_e equation is the necessity of current ramping in \mathbf{I}_s to maintain a steady \mathbf{I}_e against the plasma resistance, or alternatively a nonzero \mathbf{V}_e . It can be seen from (3.12), that in the case of a plasma resistance, a constant \mathbf{V}_s will not suffice to maintain a steady plasma current and position. As such, the plasma resistance is an important feature of the model, which has consequences for the controllability. This conclusion is illustrated by a simple, intuitive example in Appendix D.
- It is interesting to note that as the plasma mass approaches zero, the plasma profile adjusts to the fields instantaneously. This is the approximation of instantaneous MHD equilibrium.

3.0.4. Definitions of plasma bulk properties

A lumped-parameter model can be defined from equations (3.11) to (3.14), by defining various averaged plasma quantities. The total plasma current will be called I_p . The equilibrium plasma current density distribution $j(R, z)$ is calculated from the Grad-Shafranov equation [2], [1] by an inverse equilibrium reconstruction code. We take the plasma mass to be zero, because the associated modes

would operate on a frequency much higher than the range of interest.

The average plasma radial position R is defined by a current-weighted average of plasma element radial positions [12],

$$R = \frac{\sum_k i_k R_k}{\sum_k i_k}, \quad (3.15)$$

The average plasma vertical position z is defined similarly.

The effective mutual inductance matrix between the plasma and structure \mathbf{M}_{ps} is

$$I_p \mathbf{M}_{ps} \mathbf{I}_s = \sum_k i_k \mathbf{M}_{ks} \mathbf{I}_s \quad (3.16)$$

where \mathbf{M}_{ks} is the mutual inductance between the k th plasma element and the vector of structure element currents.

We define the effective plasma self inductance L_p via the equivalent energy of the total current distribution;

$$\frac{1}{2} L_p I_p^2 = \frac{1}{2} \sum_k \sum_h i_k M_{kh} i_h \quad (3.17)$$

where M_{kh} is the mutual inductance between the h th and k th elements, for $h \neq k$. In the case of $h = k$, the self inductance of the k th element is used.

To evaluate the internal energy of the plasma, W , we may start with the equations governing the plasma profile:

$$\nabla p = \mathbf{j} \times \mathbf{B}$$

$$\mu_0 \mathbf{j} = \nabla \times \mathbf{B}.$$

By substitution we have

$$\mu_0 \nabla p = (\nabla \times \mathbf{B}) \times \mathbf{B}.$$

Using the identity

$$(\nabla \times \mathbf{A}) \times \mathbf{A} = (\mathbf{A} \cdot \nabla) \mathbf{A} - \frac{1}{2} \nabla \mathbf{A}^2$$

gives

$$\begin{aligned} \mu_0 \nabla p &= (\mathbf{B} \cdot \nabla) \mathbf{B} - \frac{1}{2} \nabla \mathbf{B}^2 \\ \Rightarrow \quad \nabla \left(p + \frac{\mathbf{B}^2}{2\mu_0} \right) &= (\mathbf{B} \cdot \nabla) \mathbf{B}. \end{aligned}$$

At equilibrium and for our geometry the right hand side is small (zero for the circular, small aspect ratio approximation), which gives

$$p + \frac{\mathbf{B}^2}{2\mu_0} = \text{const.} = \frac{\mathbf{B}_0^2}{2\mu_0}$$

where \mathbf{B}_0 is the magnetic field outside the plasma (where $p = 0$).

We define

$$\beta = \frac{p}{\left(\frac{\mathbf{B}^2}{2\mu_0} \right)}.$$

Since W is the energy associated with the pressure, and taking the plasma volume V as $V = 2\pi R S$ where S is the plasma cross-sectional area, we have for W

$$W = pV = \frac{\mathbf{B}^2}{2\mu_0} \beta S 2\pi R.$$

We can write

$$W = pV = \int p \, dS \, 2\pi R.$$

Defining an average poloidal field as $\bar{\mathbf{B}}_\theta = \frac{\mu_0 I_p}{l}$, gives a correspondingly averaged poloidal beta,

$$\beta_p = \frac{\int p \, dS}{S} \frac{2\mu_0}{\bar{\mathbf{B}}_\theta^2}.$$

We can then approximate W as

$$\begin{aligned} W &= \frac{\bar{\mathbf{B}}_\theta^2}{2\mu_0} \beta_p S 2\pi R. \\ &= \mu_0 \pi \frac{S}{l^2} \beta_p R I_p^2. \end{aligned}$$

The proper evaluation of W requires careful consideration. For comparison, a slightly different treatment is to be found in [6].

3.1. Linearisation of equations

Equations (3.11) to (3.14) define the evolution of the variables $(R, z, I_p, \mathbf{I}_s)$. For consistency with earlier work [5], we will replace the variables (R, z) with (RI_p^0, zI_p^0) in which I_p^0 is the constant equilibrium plasma current. With this change of variable in place, we introduce the perturbations;

$$\mathbf{x} = \begin{bmatrix} \mathbf{I}_s - \mathbf{I}_s^0 \\ (z - z^0)I_p^0 \\ (R - R^0)I_p^0 \\ I_p - I_p^0 \end{bmatrix} = \begin{bmatrix} \delta \mathbf{I}_s \\ \delta z I_p^0 \\ \delta R I_p^0 \\ \delta I_p \end{bmatrix}. \quad (3.18)$$

3.1.1. The structure circuit equation

The tokamak structure obeys the circuit equation (3.12)

$$\begin{aligned} \frac{d(\mathbf{M}_{sp} I_p)}{dt} + \mathbf{L}_s \dot{\mathbf{I}}_s + \mathbf{\Omega}_s \mathbf{I}_s &= \mathbf{V}_s \\ \Rightarrow \dot{\mathbf{M}}_{sp} I_p + \mathbf{M}_{sp} \dot{I}_p + \mathbf{L}_s \dot{\mathbf{I}}_s + \mathbf{\Omega}_s \mathbf{I}_s &= \mathbf{V}_s \end{aligned} \quad (3.19)$$

where \mathbf{M}_{sp} is the mutual inductance matrix between the plasma and the structure, \mathbf{L}_s is the inductance matrix of the structure, and $\mathbf{\Omega}_s$ is the resistance matrix of

the structure. \mathbf{V}_s is the vector of voltages applied to the structure elements. Appendix B describes how to calculate the self and mutual inductances of an array of current carrying loops.

We know that $\mathbf{L}_s = \mathbf{L}_s^0$ and $\mathbf{\Omega}_s = \mathbf{\Omega}_s^0$ are constant. Using this and expanding all terms gives

$$\begin{aligned} \frac{d(\delta \mathbf{M}_{sp})}{dt} (I_p^0 + \delta I_p) + (\mathbf{M}_{sp}^0 + \delta \mathbf{M}_{sp}) \frac{d(\delta I_p)}{dt} + \\ \mathbf{L}_s^0 \frac{d(\delta \mathbf{I}_s)}{dt} + \mathbf{\Omega}_s^0 (I_s^0 + \delta \mathbf{I}_s) = (\mathbf{V}_s^0 + \delta \mathbf{V}_s). \end{aligned}$$

Subtracting the equilibrium equation

$$\mathbf{L}_s \dot{\mathbf{I}}_s^0 + \mathbf{\Omega}_s^0 \mathbf{I}_s^0 = \mathbf{V}_s^0$$

and neglecting second order terms, we get

$$\frac{d(\delta \mathbf{M}_{sp})}{dt} I_p^0 + \mathbf{M}_{sp}^0 \frac{d(\delta I_p)}{dt} + \mathbf{L}_s \frac{d(\delta \mathbf{I}_s)}{dt} + \mathbf{\Omega}_s \delta \mathbf{I}_s = \delta \mathbf{V}_s.$$

The time derivatives can be expanded using the chain rule in terms of the time derivatives of the state variables. The mutual inductance \mathbf{M}_{sp} is a function of geometry only, so we can write

$$\dot{\mathbf{M}}_{sp}(z I_p^0, R I_p^0) = \left. \frac{\partial \mathbf{M}_{sp}}{\partial z I_p^0} \right|_0 \frac{d(z I_p^0)}{dt} + \left. \frac{\partial \mathbf{M}_{sp}}{\partial R I_p^0} \right|_0 \frac{d(R I_p^0)}{dt}$$

allowing us to state the linearised equation in terms of the state vector and its time derivative

$$\left[\begin{array}{cc} \mathbf{L}_s & \left. \frac{\partial \mathbf{M}_{sp}}{\partial z I_p^0} \right|_0 \\ \left. \frac{\partial \mathbf{M}_{sp}}{\partial R I_p^0} \right|_0 & \mathbf{M}_{sp}^0 \end{array} \right] \begin{bmatrix} I_p^0 \\ \mathbf{I}_s^0 \end{bmatrix} \dot{\mathbf{x}} + \left[\begin{array}{cccc} \mathbf{\Omega}_s & 0 & 0 & 0 \end{array} \right] \mathbf{x} = \delta \mathbf{V}_s.$$

Since the derivatives are evaluated at the equilibrium, we can write

$$\left. \frac{\partial \mathbf{M}_{sp}}{\partial z I_p^0} \right|_0 I_p^0 = \left. \frac{\partial \mathbf{M}_{sp}}{\partial z} \right|_0$$

allowing us to simplify the linearised equation to:

$$\left[\begin{array}{c} \mathbf{L}_s \\ \left. \frac{\partial \mathbf{M}_{sp}}{\partial z} \right|_0 \end{array} \quad \left. \frac{\partial \mathbf{M}_{sp}}{\partial R} \right|_0 \quad \mathbf{M}_{sp}^0 \right] \dot{\mathbf{x}} + \left[\begin{array}{cccc} \boldsymbol{\Omega}_s & 0 & 0 & 0 \end{array} \right] \mathbf{x} = \delta \mathbf{V}_s. \quad (3.20)$$

3.1.2. The plasma circuit equation

The plasma circuit equation (3.11) becomes

$$\frac{d(\mathbf{M}_{ps} \mathbf{I}_s)}{dt} + \frac{d(L_p I_p)}{dt} + \Omega_p I_p + \frac{d \frac{\mu_0 \frac{2\pi S}{l^2} \beta_p R I_p}{2}}{dt} = V_p. \quad (3.21)$$

Following the procedure used to derive (3.20), we obtain

$$\dot{\mathbf{M}}_{ps} \mathbf{I}_s^0 + \mathbf{M}_{ps}^0 \dot{\mathbf{I}}_s + \dot{L}_p I_p^0 + L_p^0 \dot{I}_p + \Omega_p^0 \delta I_p + \delta \Omega_p I_p^0 + \frac{d \frac{\mu_0 \frac{2\pi S}{l^2} \beta_p R I_p}{2}}{dt} = \delta V_p.$$

As before we can expand the time derivative of the plasma self inductance out

$$\dot{L}_p = \left. \frac{\partial L_p}{\partial R I_p^0} \right|_0 \frac{d(R I_p^0)}{dt} + \left. \frac{\partial L_p}{\partial z I_p^0} \right|_0 \frac{d(z I_p^0)}{dt}$$

and similarly for the mutual inductances. The plasma resistance is taken as independent of \mathbf{x} . We can then write

$$\left. \frac{\partial \mathbf{M}_{ps}}{\partial z I_p^0} \right|_0 \mathbf{I}_s^0 \frac{d(z I_p^0)}{dt} + \left. \frac{\partial \mathbf{M}_{ps}}{\partial R I_p^0} \right|_0 \mathbf{I}_s^0 \frac{d(R I_p^0)}{dt} + \mathbf{M}_{ps}^0 \dot{\mathbf{I}}_s + \left. \frac{\partial L_p}{\partial R I_p^0} \right|_0 I_p^0 \frac{d(R I_p^0)}{dt} + \left. \frac{\partial L_p}{\partial z I_p^0} \right|_0 I_p^0 \frac{d(z I_p^0)}{dt} +$$

$$L_p^0 \dot{I}_p + \mu_0 \frac{2\pi S}{l^2} \beta_p \left(\dot{R} I_p^0 + R^0 \dot{I}_p \right) = \delta V_p.$$

The term $\left. \frac{\partial \mathbf{M}_{ps}}{\partial z} \right|_0 \mathbf{I}_s$ is the radial magnetic field at equilibrium, which is zero.

This gives

$$\left[\begin{array}{cc} \mathbf{M}_{ps}^0 & \left. \frac{\partial L_p}{\partial z} \right|_0 \\ \left(\left. \frac{\partial \mathbf{M}_{ps}}{\partial R} \right|_0 \frac{\mathbf{I}_s^0}{I_p^0} + \left. \frac{\partial L_p}{\partial R} \right|_0 + \mu_0 \frac{2\pi S}{l^2} \beta_p \right) & (L_p^0 + \mu_0 \frac{2\pi S}{l^2} \beta_p R^0) \end{array} \right] \dot{\mathbf{x}} + \left[\begin{array}{cccc} \mathbf{0} & 0 & 0 & \Omega_p^0 \end{array} \right] \mathbf{x} = \delta \mathbf{V}_p. \quad (3.22)$$

3.1.3. The vertical force balance equation

The vertical force balance equation (3.14) is

$$\frac{\partial L_p}{\partial z} \frac{I_p^2}{2} + \frac{\partial (I_p \mathbf{M}_{ps} \mathbf{I}_s)}{\partial z} = 0$$

Perturbing the equation and taking the time derivative gives

$$\begin{aligned} \frac{1}{2} \frac{d\delta \left(\frac{\partial L_p}{\partial z} I_p^2 \right)}{dt} + \frac{d\delta \left(I_p \frac{\partial \mathbf{M}_{ps}}{\partial z} \mathbf{I}_s \right)}{dt} = \\ \frac{1}{2} \frac{\partial^2 L_p}{\partial z^2} \Big|_0 \dot{z} I_p^0 I_p^0 + \frac{1}{2} \frac{\partial^2 L_p}{\partial z \partial R} \Big|_0 \dot{R} I_p^0 I_p^0 + \left. \frac{\partial L_p}{\partial z} \right|_0 I_p^0 \dot{I}_p^0 + \\ I_p^0 \left. \frac{\partial \mathbf{M}_{ps}}{\partial z} \right|_0 \dot{\mathbf{I}}_s + \left. \frac{\partial \mathbf{M}_{ps}}{\partial z} \right|_0 \mathbf{I}_s^0 \dot{I}_p + \frac{\partial^2 \mathbf{M}_{ps}}{\partial z^2} \Big|_0 \mathbf{I}_s^0 \frac{d(z I_p^0)}{dt} + \frac{\partial^2 \mathbf{M}_{ps}}{\partial z \partial R} \Big|_0 \mathbf{I}_s^0 \frac{d(R I_p^0)}{dt} = 0 \end{aligned}$$

The term $\left. \frac{\partial \mathbf{M}_{ps}}{\partial z} \right|_0 \mathbf{I}_s$ is the radial magnetic field at equilibrium, which is zero.

This gives the linearised vertical force balance equation which can be expressed as

$$\left[\begin{array}{cc} \left. \frac{\partial \mathbf{M}_{ps}}{\partial z} \right|_0 & \left(\left. \frac{1}{2} \frac{\partial^2 L_p}{\partial z^2} \right|_0 + \left. \frac{\partial^2 \mathbf{M}_{ps}}{\partial z^2} \right|_0 \frac{\mathbf{I}_s^0}{I_p^0} \right) \\ \left(\left. \frac{1}{2} \frac{\partial^2 L_p}{\partial z \partial R} \right|_0 + \left. \frac{\partial^2 \mathbf{M}_{ps}}{\partial z \partial R} \right|_0 \frac{\mathbf{I}_s^0}{I_p^0} \right) & \left. \frac{\partial L_p}{\partial z} \right|_0 \end{array} \right] \dot{\mathbf{x}} = 0. \quad (3.23)$$

3.1.4. The radial force balance equation

The radial force balance equation (3.13) becomes

$$\frac{1}{2} \frac{\partial L_p I_p^2}{\partial R} + \frac{\partial(I_p \mathbf{M}_{ps} \mathbf{I}_s)}{\partial R} + \mu_0 \frac{\pi S}{l^2} \beta_p I_p^2 = 0 \quad (3.24)$$

Consider this equation term-by-term.

$$\sigma + \tau + v = 0$$

Perturbing term by term and taking the time derivative gives

$$\begin{aligned} \frac{d\delta\sigma}{dt} &= \frac{d\delta \left(\frac{1}{2} \frac{\partial L_p}{\partial R} I_p^2 \right)}{dt} = \frac{\partial L_p}{\partial R} \bigg|_0 I_p^0 \dot{I}_p + \frac{\partial^2 L_p}{\partial R^2} \bigg|_0 \frac{I_p^0}{2} \dot{R} I_p^0 + \frac{1}{2} \frac{\partial^2 L_p}{\partial z \partial R} \bigg|_0 I_p^0 \dot{z} I_p^0 \\ \frac{d\delta\tau}{dt} &= \frac{d\delta \left(I_p \frac{\partial \mathbf{M}_{ps}}{\partial R} \mathbf{I}_s \right)}{dt} \\ &= \frac{\partial \mathbf{M}_{ps}}{\partial R} \bigg|_0 \mathbf{I}_s^0 \dot{I}_p + I_p^0 \frac{\partial \mathbf{M}_{ps}}{\partial R} \bigg|_0 \dot{\mathbf{I}}_s + \frac{\partial^2 \mathbf{M}_{ps}}{\partial R^2} \bigg|_0 \mathbf{I}_s^0 \frac{d(R I_p^0)}{dt} + \frac{\partial^2 \mathbf{M}_{ps}}{\partial z \partial R} \bigg|_0 \mathbf{I}_s^0 \frac{d(z I_p^0)}{dt} \\ \frac{d\delta v}{dt} &= \mu_0 \frac{2\pi S}{l^2} \beta_p I_p^0 \dot{I}_p \end{aligned}$$

Putting the parts together gives the linearised radial force balance equation, which can be written as

$$\begin{aligned} &\left[\frac{\partial \mathbf{M}_{ps}}{\partial R} \bigg|_0 \left(\frac{1}{2} \frac{\partial^2 L_p}{\partial z \partial R} \bigg|_0 + \frac{\partial^2 \mathbf{M}_{ps}}{\partial z \partial R} \bigg|_0 \frac{\mathbf{I}_s^0}{I_p^0} \right) \quad \dots \right. \\ &\quad \left. \dots \left(\frac{1}{2} \frac{\partial^2 L_p}{\partial R^2} \bigg|_0 + \frac{\partial^2 \mathbf{M}_{ps}}{\partial R^2} \bigg|_0 \frac{\mathbf{I}_s^0}{I_p^0} \right) \left(\frac{\partial L_p}{\partial R} \bigg|_0 + \frac{\partial \mathbf{M}_{ps}}{\partial R} \bigg|_0 \frac{\mathbf{I}_s^0}{I_p^0} + \mu_0 \frac{2\pi S}{l^2} \beta_p \right) \right] \dot{\mathbf{x}} = 0. \end{aligned} \quad (3.25)$$

3.2. The eigenmode representation of passive structure currents

In this section we review the eigenmode representation of the tokamak passive structure. The tokamak structure can be considered as two separate interacting parts, the active structure (the coil system) and the passive structure (the vacuum vessel and protective components). The active structure by definition is able to support externally applied voltages. In the case of more than one distinct passive structure, the passive structures need to be considered separately.

The state of the structure can be written as

$$\mathbf{I}_s = \begin{pmatrix} \mathbf{I}_c \\ \mathbf{I}_v \end{pmatrix}$$

where subscript v (for vessel) denotes the passive structure and subscript c (for coils) denotes the active structure.

The plasma circuit equation is

$$\frac{d(\mathbf{M}_{ps}\mathbf{I}_s)}{dt} + \frac{d(L_p I_p)}{dt} + \Omega_p I_p = 0.$$

The circuit equations of the structure (3.12) and the plasma can then be written as a matrix equation:

$$\begin{bmatrix} \mathbf{L}_c & \mathbf{M}_{cv} & \mathbf{M}_{cp} \\ \mathbf{M}_{vc} & \mathbf{L}_v & \mathbf{M}_{vp} \\ \mathbf{M}_{pc} & \mathbf{M}_{pv} & L_p \end{bmatrix} \begin{pmatrix} \dot{\mathbf{I}}_c \\ \dot{\mathbf{I}}_v \\ \dot{I}_p \end{pmatrix} + \begin{bmatrix} \Omega_c & 0 & \dot{\mathbf{M}}_{cp} \\ 0 & \Omega_v & \dot{\mathbf{M}}_{vp} \\ \dot{\mathbf{M}}_{pc} & \dot{\mathbf{M}}_{pv} & \Omega_p + \dot{L}_p \end{bmatrix} \begin{pmatrix} \mathbf{I}_c \\ \mathbf{I}_v \\ I_p \end{pmatrix} = \begin{pmatrix} \mathbf{V}_c \\ 0 \\ 0 \end{pmatrix}. \quad (3.26)$$

The passive structure has induced eddy currents occurring over different time-

scales, associated with the $\Omega^{-1}\mathbf{L}$ times. If we set

$$\mathbf{\Lambda} = \Omega_v^{-1}\mathbf{L}_v$$

then the eigenvalues and eigenvectors of $\mathbf{\Lambda}$ will relate to the different physical responses or eigenmodes of various frequencies of the vessel structure. Writing

$$\mathbf{\Lambda}\Psi = \Psi\lambda$$

we can represent the vessel states in terms of its eigenvectors Ψ ,

$$\mathbf{I}_v = \Psi\mathbf{I}_\Lambda.$$

Pre-multiplying the second line of (3.26) by Ω_v^{-1} and replacing \mathbf{I}_v with $\Psi\mathbf{I}_\Lambda$ gives

$$\begin{bmatrix} \mathbf{L}_c & \mathbf{M}_{cv}\Psi & \mathbf{M}_{cp} \\ \Omega_v^{-1}\mathbf{M}_{vc} & \Omega_v^{-1}\mathbf{L}_v\Psi & \Omega_v^{-1}\mathbf{M}_{vp} \\ \mathbf{M}_{pc} & \mathbf{M}_{pv}\Psi & L_p \end{bmatrix} \begin{pmatrix} \dot{\mathbf{I}}_c \\ \dot{\mathbf{I}}_\Lambda \\ \dot{I}_p \end{pmatrix} + \begin{bmatrix} \Omega_c & 0 & \dot{\mathbf{M}}_{cp} \\ 0 & \Psi & \Omega_v^{-1}\dot{\mathbf{M}}_{vp} \\ \dot{\mathbf{M}}_{pc} & \dot{\mathbf{M}}_{pv}\Psi & \Omega_p + \dot{L}_p \end{bmatrix} \begin{pmatrix} \mathbf{I}_c \\ \mathbf{I}_\Lambda \\ I_p \end{pmatrix} = \begin{pmatrix} \mathbf{V}_c \\ 0 \\ 0 \end{pmatrix}.$$

We know that $\Omega_v^{-1}\mathbf{L}_v\Psi = \mathbf{\Lambda}\Psi = \Psi\lambda$; substituting this in and pre-multiplying the second line by Ψ^{-1} yields the circuit equations in terms of the vessel eigenmodes

$$\begin{bmatrix} \mathbf{L}_c & \mathbf{M}_{cv}\Psi & \mathbf{M}_{cp} \\ \Psi^{-1}\Omega_v^{-1}\mathbf{M}_{vc} & \lambda & \Psi^{-1}\Omega_v^{-1}\mathbf{M}_{vp} \\ \mathbf{M}_{pc} & \mathbf{M}_{pv}\Psi & L_p \end{bmatrix} \begin{pmatrix} \dot{\mathbf{I}}_c \\ \dot{\mathbf{I}}_\Lambda \\ \dot{I}_p \end{pmatrix} +$$

$$\begin{bmatrix} \Omega_c & 0 & \dot{\mathbf{M}}_{cp} \\ 0 & 1 & \Psi^{-1} \Omega_v^{-1} \dot{\mathbf{M}}_{vp} \\ \dot{\mathbf{M}}_{pc} & \dot{\mathbf{M}}_{pv} \Psi & \Omega_p + \dot{L}_p \end{bmatrix} \begin{pmatrix} \mathbf{I}_c \\ \mathbf{I}_\Lambda \\ I_p \end{pmatrix} = \begin{pmatrix} \mathbf{V}_c \\ 0 \\ 0 \end{pmatrix}.$$

These equations can be linearised and incorporated into the model in the same way as the straightforward structure circuit equation. In this way we can represent the passive structure states in terms of the current eigenmodes rather than the currents. A truncation of eigenmode states naturally follows, by ignoring eigenmodes with frequencies outside the experimental bandwidth or by some other criterion.

3.3. System outputs

In this section we review the method of reproducing the tokamak outputs from the model states.

Some states of the tokamak can be considered as part of the output. In addition there are two more quantities that appear in the output vector, the poloidal magnetic field (\mathbf{B}_{pol}) at a given point and the magnetic flux at a given point. In the state space form, the vector of outputs \mathbf{y} is related to the state vector \mathbf{x} by

$$\mathbf{y} = \mathbf{C}\mathbf{x} + \mathbf{D}\mathbf{u}.$$

Since the control vector \mathbf{u} does not directly affect the output, the feedforward matrix \mathbf{D} is zero.

3.3.1. Flux loops

Figure 3.3 shows how a flux loop is placed in a tokamak. There will be flux loops all around the tokamak.

A change in flux Φ within the loop is measured by the induced voltage ε across

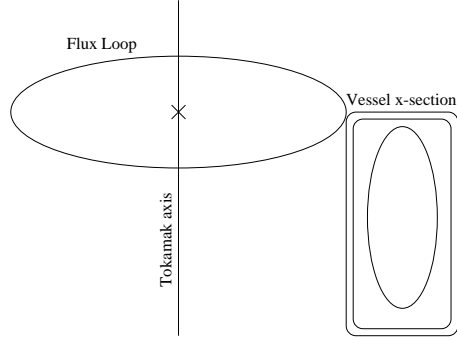


Figure 3.3: Location and shape of a flux loop

the loop; the change in flux is given by the relationship

$$\Delta\Phi = \Delta(M_{pf}I_p + \mathbf{M}_{sf}\mathbf{I}_s).$$

M_{pf} is the mutual inductance between the plasma and the flux loop. This equation can be expanded about the plasma equilibrium state;

$$\begin{aligned} \Delta\Phi = & \left[\frac{\partial M_{pf}}{\partial z} \bigg|_0 \delta(zI_p^0) + \frac{\partial M_{pf}}{\partial R} \bigg|_0 \delta(RI_p^0) \right] I_p \\ & + M_{pf}^0 \delta I_p + \mathbf{M}_{sf}^0 \delta \mathbf{I}_s. \end{aligned}$$

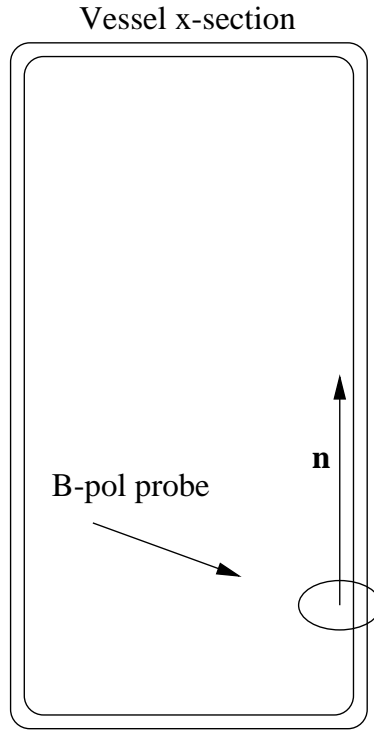
Casting this in terms of the state vector gives

$$\Delta\Phi = \begin{bmatrix} \mathbf{M}_{sf}^0 & \frac{\partial M_{pf}}{\partial z} \bigg|_0 & \frac{\partial M_{pf}}{\partial R} \bigg|_0 & M_{pf}^0 \end{bmatrix} \mathbf{x}. \quad (3.27)$$

3.3.2. Poloidal magnetic field probes

The poloidal magnetic field (\mathbf{B}_{pol}) probe is a loop of negligible area. It measures the magnetic field normal to the loop.

If the magnetic field at the probe is $\mathbf{B} = B_R \hat{\mathbf{R}} + B_z \hat{\mathbf{z}}$, and if $\hat{\mathbf{n}}$ is normal to the

Figure 3.4: B_{pol} probe geometry

coil, it follows that (see Figure 3.4)

$$\mathbf{B} \cdot \hat{\mathbf{n}} = B_{pol}.$$

Since magnetic fields obey the superposition principle, the field can be calculated from each current element and then the contributions summed to give the total magnetic field \mathbf{B} ;

$$\mathbf{B} = \sum_{all\ I} \mathbf{B}_I.$$

Formulae are given for B_R and B_z in Appendix B. From these we can see that all of \mathbf{B} is invariant and known from the tokamak geometry, except for the state variables. Therefore we can expand \mathbf{B} in terms of the state variables about the tokamak equilibrium.

$$\mathbf{B}_{pol} = \frac{\partial(\mathbf{B} \cdot \hat{\mathbf{n}})}{\partial RI_p^0} \bigg|_0 \delta(RI_p^0) + \frac{\partial(\mathbf{B} \cdot \hat{\mathbf{n}})}{\partial zI_p^0} \bigg|_0 \delta(zI_p^0) + \frac{\partial(\mathbf{B} \cdot \hat{\mathbf{n}})}{\partial I_p} \bigg|_0 \delta(I_p) + \frac{\partial(\mathbf{B} \cdot \hat{\mathbf{n}})}{\partial I_s} \bigg|_0 \delta(I_s).$$

This can be written in terms of the state vector:

$$\mathbf{B}_{pol} = \begin{bmatrix} \frac{\partial(\mathbf{B} \cdot \hat{\mathbf{n}})}{\partial I_s} \bigg|_0 & \frac{\partial(\mathbf{B} \cdot \hat{\mathbf{n}})}{\partial zI_p^0} \bigg|_0 & \frac{\partial(\mathbf{B} \cdot \hat{\mathbf{n}})}{\partial RI_p^0} \bigg|_0 & \frac{\partial(\mathbf{B} \cdot \hat{\mathbf{n}})}{\partial I_p} \bigg|_0 \end{bmatrix} \mathbf{x}. \quad (3.28)$$

3.3.3. The output matrix, C

Using results (3.27, 3.28), we can relate the system outputs \mathbf{y} to the state of the system \mathbf{x} by writing (where the subscript n denotes a particular diagnostic):

$$\mathbf{y} = \mathbf{C}\mathbf{x}$$

$$\begin{pmatrix} I_c \\ zI_p^0 \\ RI_p^0 \\ I_p \\ \mathbf{B}_{pol_n} \\ \Delta\phi_n \end{pmatrix} = \begin{bmatrix} \begin{bmatrix} \mathbf{I} & \mathbf{0} \end{bmatrix} & 0 & 0 & 0 \\ \mathbf{0} & 1 & 0 & 0 \\ \mathbf{0} & 0 & 1 & 0 \\ \mathbf{0} & 0 & 0 & 1 \\ \frac{\partial(\mathbf{B} \cdot \hat{\mathbf{n}})_n}{\partial I_s} \bigg|_0 & \frac{\partial(\mathbf{B} \cdot \hat{\mathbf{n}})_n}{\partial zI_p^0} \bigg|_0 & \frac{\partial(\mathbf{B} \cdot \hat{\mathbf{n}})_n}{\partial RI_p^0} \bigg|_0 & \frac{\partial(\mathbf{B} \cdot \hat{\mathbf{n}})_n}{\partial I_p} \bigg|_0 \\ (\mathbf{M}_{sf}^0)_n & \frac{\partial(\mathbf{M}_{pf})_n}{\partial z} \bigg|_0 & \frac{\partial(\mathbf{M}_{pf})_n}{\partial R} \bigg|_0 & (\mathbf{M}_{pf}^0)_n \end{bmatrix} \mathbf{x}. \quad (3.29)$$

3.4. The state-space model of a Tokamak

The four physics equations are now linearised in \mathbf{x} about the equilibrium $\mathbf{x}^0 = \mathbf{0}$, to give four linear equations. These can then be cast in the standard state-space model form:

$$\begin{aligned} \dot{\mathbf{x}} &= \mathbf{A}\mathbf{x} + \mathbf{B}u \\ \mathbf{y} &= \mathbf{C}\mathbf{x} + \mathbf{D}u. \end{aligned} \quad (3.30)$$

The linearised structure circuit equation, plasma circuit equation and plasma force balance equations can be represented as follows:

$$\begin{aligned}
 & \left[\begin{array}{ccc} \mathbf{L}_s & \left. \frac{\partial \mathbf{M}_{sp}}{\partial z} \right|_0 & \dots \\ \left. \frac{\partial \mathbf{M}_{ps}}{\partial z} \right|_0 & \left(\left. \frac{1}{2} \frac{\partial^2 L_p}{\partial z^2} \right|_0 + \left. \frac{\partial^2 \mathbf{M}_{ps}}{\partial z^2} \right|_0 \frac{\mathbf{I}_s^0}{I_p^0} \right) & \dots \\ \left. \frac{\partial \mathbf{M}_{ps}}{\partial R} \right|_0 & \left(\left. \frac{1}{2} \frac{\partial^2 L_p}{\partial z \partial R} \right|_0 + \left. \frac{\partial^2 \mathbf{M}_{ps}}{\partial z \partial R} \right|_0 \frac{\mathbf{I}_s^0}{I_p^0} \right) & \dots \\ \mathbf{M}_{ps}^0 & \left. \frac{\partial L_p}{\partial z} \right|_0 & \dots \end{array} \right. \\
 & \left. \begin{array}{cc} \left. \frac{\partial \mathbf{M}_{sp}}{\partial R} \right|_0 & \mathbf{M}_{sp}^0 \\ \left(\left. \frac{1}{2} \frac{\partial^2 L_p}{\partial z \partial R} \right|_0 + \left. \frac{\partial^2 \mathbf{M}_{ps}}{\partial z \partial R} \right|_0 \frac{\mathbf{I}_s^0}{I_p^0} \right) & \left. \frac{\partial L_p}{\partial z} \right|_0 \\ \left(\left. \frac{1}{2} \frac{\partial^2 L_p}{\partial R^2} \right|_0 + \left. \frac{\partial^2 \mathbf{M}_{ps}}{\partial R^2} \right|_0 \frac{\mathbf{I}_s^0}{I_p^0} \right) & \left(\left. \frac{\partial L_p}{\partial R} \right|_0 + \left. \frac{\partial \mathbf{M}_{ps}}{\partial R} \right|_0 \frac{\mathbf{I}_s^0}{I_p^0} + \mu_0 \frac{2\pi S}{l^2} \beta_p \right) \\ \left(\left. \frac{\partial \mathbf{M}_{ps}}{\partial R} \right|_0 \frac{\mathbf{I}_s^0}{I_p^0} + \left. \frac{\partial L_p}{\partial R} \right|_0 + \mu_0 \frac{2\pi S}{l^2} \beta_p \right) & L_p^0 + \mu_0 \frac{2\pi S}{l^2} \beta_p R^0 \end{array} \right] \dot{\mathbf{x}} \quad (3.31) \\
 & + \begin{bmatrix} \boldsymbol{\Omega}_s & 0 & 0 & 0 \\ \mathbf{0} & 0 & 0 & 0 \\ \mathbf{0} & 0 & 0 & 0 \\ \mathbf{0} & 0 & 0 & \Omega_p \end{bmatrix} \mathbf{x} = \begin{bmatrix} \mathbf{I} & 0 \\ \mathbf{0} & 0 \\ \mathbf{0} & 0 \\ \mathbf{0} & I \end{bmatrix} \begin{bmatrix} \delta \mathbf{V}_s \\ \delta V_p \end{bmatrix}.
 \end{aligned}$$

This is of the form $\mathcal{M}\dot{\mathbf{x}} + \mathcal{R}\mathbf{x} = \mathbf{u}$. Comparing (3.31) with (3.30) gives the matrix of coefficients \mathbf{A} , and the control matrix \mathbf{B} ;

$$\begin{aligned}
 \mathbf{A} &= -\mathcal{M}^{-1}\mathcal{R} \\
 \mathbf{B} &= \mathcal{M}^{-1} \begin{bmatrix} \mathbf{I} & 0 & 0 & 0 \\ 0 & 0 & 0 & I \end{bmatrix}^T.
 \end{aligned}$$

Note that \mathcal{M} and \mathcal{R} are symmetric with \mathcal{M} positive definite and \mathcal{R} positive

semi-definite.

From a minimal set of assumptions we have derived a linear, time invariant model in state-space form. All linear models with the same choice of states can be represented in this form.

3.4.1. The RZIP linear model

Further to the assumptions detailed earlier, the linear RZIP model also makes the rigid current displacement assumption, namely that the normalised current profile is independent of movements in the R and z directions and of changes in plasma current. It follows therefore that changes in the plasma current profile are not modelled. As such, $\left. \frac{\partial L_p}{\partial z} \right|_0 = 0$.

Changes to the current and pressure profile can be approximately modelled by permitting perturbations to β_p . These changes are then introduced as disturbances in $\dot{\beta}_p$ on the right hand side of (3.31), as in [6].

The rigid current displacement assumption allows us to calculate the plasma mutual and self inductance derivatives simply and directly.

For example, the mutual inductance between two plasma elements must satisfy:

$$\frac{\partial M_{fg}}{\partial R} = \frac{\partial M_{fg}}{\partial R_f} \frac{\partial R_f}{\partial R} + \frac{\partial M_{fg}}{\partial R_g} \frac{\partial R_g}{\partial R}.$$

The rigid current displacement assumption fixes the two radius relations as

$$\frac{\partial R_f}{\partial R} = \frac{\partial R_g}{\partial R} = 1.$$

Results for System Identification

4.1. Identification algorithm

The identification algorithm described follows previous work [5, 29]. We review it here in a form suitable for its application in the following chapter.

4.1.1. Least-squares method for estimating the amplitude of specific frequencies in a signal

In this work we assume that the identified plant is essentially linear. Any output signal frequency not present in the input spectrum is a non-linear effect and is considered noise. In this sense, the error is a measure of the linearity of the plant. If the plant is linear, the signal sampled at any point will comprise the frequencies in the input. We use a form of curve-fitting applicable to signals made up of non-harmonic frequencies, presented in [29].

Assuming linearity, in the absence of noise, a sampled signal consisting of N sine waves can be decomposed as

$$u(kt_s) = \sum_{i=0}^N A_i \cos(\omega_i kt_s + \phi_i), \quad (4.1)$$

for $k = 0, 1, \dots, m$ where $m + 1$ is the total number of data points and $2\pi/t_s$ is the sampling frequency.

Allowing for a linear drift term, we may define

$$e_k = u(kt_s) - \sum_{i=1}^N B_i \cos(\omega_i kt_s) + C_i \sin(\omega_i kt_s) + D + Ekt_s.$$

We calculate B_i , C_i , D and E such the square of the error,

$$e^T e$$

is minimised, where e is the vector of errors,

$$e = [e_0 \ e_1 \ \dots \ e_m]^T.$$

Then A_i and ϕ_i are given by

$$A_i = \sqrt{B_i^2 + C_i^2}$$

and

$$\phi_i = \tan^{-1}(-C_i/B_i).$$

We write

$$e = U - \Phi\theta$$

where

$$U = [u(0) \ u(t_s) \ \dots \ u(mt_s)]^T,$$

$$\Phi = \begin{bmatrix} 1 & \dots & 1 & 0 & \dots & 0 & 1 & 0 \\ \cos(\omega_1 t_s) & \dots & \cos(\omega_N t_s) & \sin(\omega_1 t_s) & \dots & \sin(\omega_N t_s) & 1 & t_s \\ \cos(\omega_1 2t_s) & \dots & \cos(\omega_N 2t_s) & \sin(\omega_1 2t_s) & \dots & \sin(\omega_N 2t_s) & 1 & 2t_s \\ \vdots & \ddots & \vdots & \vdots & \ddots & \vdots & \vdots & \vdots \\ \cos(\omega_1 mt_s) & \dots & \cos(\omega_N mt_s) & \sin(\omega_1 mt_s) & \dots & \sin(\omega_N mt_s) & 1 & mt_s \end{bmatrix}$$

and

$$\theta = [B_1 \ \dots \ B_N \ C_1 \ \dots \ C_N \ D \ E]^T.$$

Necessary for a minimising solution θ^* to be minimising is

$$\left. \frac{d(e^T e)}{d\theta} \right|_{\theta^*} = 0 \quad \Rightarrow$$

$$-\Phi^T U + \Phi^T \Phi \theta^* = 0$$

or

$$\theta^* = (\Phi^T \Phi)^{-1} \Phi^T U.$$

From the second derivative

$$\frac{d^2(e^T e)}{d\theta^2} = \Phi^T \Phi$$

$$> 0$$

we see that θ^* is indeed a minimum.

4.1.2. Frequency response estimation

With this method, for a $p \times q$ system we obtain a best estimate of $U_k^j(\omega_i)$, the k th input from the j th experiment, $k = 1, \dots, q$ and $j = 1, \dots, q$, at ω_i , and similarly the output $Y_k^j(\omega_i)$. This gives an expression for the frequency response estimate $\hat{\mathbf{G}}$ [29],

$$\begin{bmatrix} Y_1^1(\omega_i) & \dots & Y_1^q(\omega_i) \\ \vdots & \ddots & \vdots \\ Y_p^1(\omega_i) & \dots & Y_p^q(\omega_i) \end{bmatrix} = \begin{bmatrix} \hat{G}_{11}(\omega_i) & \dots & \hat{G}_{1q}(\omega_i) \\ \vdots & \ddots & \vdots \\ \hat{G}_{p1}(\omega_i) & \dots & \hat{G}_{pq}(\omega_i) \end{bmatrix} \begin{bmatrix} U_1^1(\omega_i) & \dots & U_1^q(\omega_i) \\ \vdots & \ddots & \vdots \\ U_q^1(\omega_i) & \dots & U_q^q(\omega_i) \end{bmatrix}. \quad (4.2)$$

This gives

$$\hat{\mathbf{G}}(\omega_i) = \mathbf{Y}(\omega_i) \mathbf{U}^{-1}(\omega_i).$$

To be invertible \mathbf{U} must have full rank, a condition satisfied by the independence of the experiments.

An expression for the estimate of the error on $\hat{\mathbf{G}}$ is to be found in [29].

4.2. Estimating modelling uncertainty

This section will present two methods for estimating modelling uncertainty given experimental data. The second method is original and both are presented in [6].

Parametric or grey-box modelling allows certain model parameters to be adjusted until any discrepancy between the observed and predicted data is minimised. In this sense the resulting grey-box model is optimal. Of course it becomes necessary to quantify the model-data discrepancy (by means of a cost function) so that minimisation is possible. The appropriate choice of cost function will depend on the intended model application. For our particular case we are considering a system that has outputs measured in many different units at different magnitudes, from milli-Teslas to mega-Ampères. Consequently it becomes necessary to define a cost function that is equally responsive to all outputs regardless of unit. There are many possible ways of achieving this. Also the plant response varies in magnitude significantly over the experimental frequency range. A suitable cost function could equally weight the response at all frequencies (given a sufficiently good signal to noise ratio) as different significant physical effects are important at different frequencies.

4.2.1. Error estimation for physical modelling

A first quantification of the model error is derived simply from the differences between the data points and the model prediction, for all data points. We consider that the cost function described below should provide a simple estimate of the uncertainty. These distances are normalised to an estimate of the likely error. The weighted error given below has an upper bound of 2, corresponding to the case where the model and data are equal in amplitude and π apart in phase.

One cost function is therefore defined as

$$\chi^2 = \sum_i \frac{2(d_i - m_i)^2}{d_i^2 + m_i^2}$$

where d_i is a data point and m_i is the corresponding model prediction.

4.2.2. Error estimation for robust control

The infinity norm $\|\cdot\|_\infty$ is well understood and commonly employed in the control literature [30] as a useful tool for quantifying multi-input multi-output modelling uncertainty. Here we establish its relation to the singular value decomposition to demonstrate its significance as the worst case energy gain of a system.

The singular value decomposition

For any $m \times p$ complex matrix \mathbf{Q} , there exist $m \times m$ and $p \times p$ unitary matrices \mathbf{Y} and \mathbf{U} such that

$$\mathbf{Q} = \mathbf{Y} \begin{bmatrix} \boldsymbol{\Sigma} & \mathbf{0} \\ \mathbf{0} & \mathbf{0} \end{bmatrix} \mathbf{U}^* \quad (4.3)$$

where $\boldsymbol{\Sigma} = \text{diag}(\sigma_1, \dots, \sigma_r)$ with $\sigma_1 \geq \sigma_2 \geq \dots \geq \sigma_r > 0$, $r \leq \min(m, p)$. Expression (4.3) is the singular value decomposition of \mathbf{Q} . The σ s are the singular values. A proof of existence can be found in [31].

Letting \mathbf{u}_i and \mathbf{y}_i be the rows and columns of \mathbf{U} and \mathbf{Y} , we can express \mathbf{Q} in terms of the dyadic expansion

$$\mathbf{Q} = \left(\sum_{i=1}^r \sigma_i \mathbf{y}_i \mathbf{u}_i^* \right).$$

Since \mathbf{U} is unitary, $\mathbf{u}_i^* \mathbf{u}_j = \delta_{ij}$, so \mathbf{u}_j is mapped by \mathbf{Q} into

$$\mathbf{Q} \mathbf{u}_j = \left(\sum_{i=1}^r \sigma_i \mathbf{y}_i \mathbf{u}_i^* \right) \mathbf{u}_j = \sigma_j \mathbf{y}_j.$$

We can therefore regard the matrix \mathbf{Q} as a linear mapping from vector space \mathbb{C}^p to \mathbb{C}^m defined by

$$\mathbf{Q}: \mathbb{C}^p \mapsto \mathbb{C}^m: \mathbf{u} \mapsto \mathbf{Q}\mathbf{u}.$$

The set of columns of the singular-vector matrices \mathbf{U} and \mathbf{Y} respectively define unitary bases for the domain \mathbb{C}^p and range \mathbb{C}^m of \mathbf{Q} . For this choice of bases, the mapping \mathbf{Q} takes the j th basis vector \mathbf{u}_j of \mathbb{C}^p to a vector lying in the direction of the j th basis \mathbf{y}_j of \mathbb{C}^m . If we restrict \mathbf{Q} to the one-dimensional complex subspace spanned by \mathbf{u}_j , the corresponding singular value σ_j can be regarded as a gain factor for the restriction map $\mathbf{Q}|_{\mathbf{u}_j}$ [30].

The maximum singular value $\bar{\sigma}$ is clearly just

$$\bar{\sigma}(\mathbf{Q}) = \sigma_1(\mathbf{Q}).$$

The infinity norm as the worst case energy gain

Suppose we have the transfer function

$$\mathbf{y} = \mathbf{G}\mathbf{u}, \quad \mathbf{G} \in \mathcal{RH}_\infty^{+, p \times m}.$$

We can define the infinity norm of \mathbf{G} as

$$\|\mathbf{G}\|_\infty = \max_{\mathbf{u} \neq 0} \frac{\|\mathbf{G}\mathbf{u}\|_2}{\|\mathbf{u}\|_2}.$$

where we use the standard $\mathcal{L}^2[0, \infty]$ norm, which for $\mathbf{u}(t)$ is (if $\mathbf{u}(t)$ is a square integrable time function,)

$$\|\mathbf{u}(t)\|_2 = \int_0^\infty \mathbf{u}^*(t)\mathbf{u}(t) \, dt < \infty.$$

This represents the energy in the signal $\mathbf{u}(t)$. By Parseval's theorem we have

$$\|\mathbf{u}(t)\|_2 = \|\mathbf{u}(j\omega)\|_2.$$

Intuitively therefore the infinity norm is the worst case energy gain.

It is possible to show [30]

$$\|\mathbf{G}\|_\infty = \sup_{\omega} \bar{\sigma}(\mathbf{G}(j\omega)).$$

Model uncertainty

We can use these definitions to quantify and interpret an unstructured model error¹.

Calculation of model error

Given the model error representation

$$\hat{\mathbf{G}}(j\omega) = (\mathbf{I} + \Delta(j\omega))\mathbf{G}(j\omega)$$

we wish to find $\hat{\mathbf{G}}$ such that $\|\Delta\|_\infty$ is minimised.

If \mathbf{G} has full column rank (almost everywhere) there exists a spectral factor $\mathbf{M} \in \mathcal{RH}_\infty$ with $\mathbf{M}^{-1} \in \mathcal{RH}_\infty$ such that $\mathbf{G}^*\mathbf{G} = \mathbf{M}\mathbf{M}^*$. Here we use the adjoint system $\mathbf{G}^* = \mathbf{G}^T(-j\omega)$. For any $\hat{\mathbf{G}}$ defining $\Delta = (\hat{\mathbf{G}} - \mathbf{G})(\mathbf{G}^*\mathbf{G})^{-1}\mathbf{G}^*$ gives $\hat{\mathbf{G}} = (\mathbf{I} + \Delta)\mathbf{G}$ and

$$\|\Delta\|_\infty = \|(\mathbf{G} - \hat{\mathbf{G}})\mathbf{M}^{*-1}\mathbf{M}^{-1}\mathbf{G}^*\|_\infty \leq \|(\mathbf{G} - \hat{\mathbf{G}})\mathbf{M}^{*-1}\|_\infty,$$

¹The model error is unstructured in the sense that we assume nothing about the model error probability distribution. The error therefore may be due to random noise or unmodelled dynamics.

so we have a conservative estimate of the model error $||\Delta||_\infty$. An algorithm for evaluating \mathbf{M} in state-space form can be found in [32]. For our purposes we need to evaluate \mathbf{M} at only a few specific frequencies. This can be done simply via the singular value decomposition of $\mathbf{G}^*\mathbf{G}$,

$$\mathbf{G}^*\mathbf{G} = \mathbf{Y}\Sigma\mathbf{V}^*,$$

with \mathbf{Y} , \mathbf{V} unitary, and since $\mathbf{G}^*\mathbf{G}$ is Hermitian, $\mathbf{Y} = \mathbf{V}$.

Thus we can write (since \mathbf{Y} is unitary and Σ is positive definite)

$$\begin{aligned}\mathbf{G}^*\mathbf{G} &= \mathbf{Y}\Sigma\mathbf{Y}^* \\ &= \mathbf{Y}\Sigma^{1/2}\mathbf{Y}^*\mathbf{Y}\Sigma^{1/2}\mathbf{Y}^*.\end{aligned}$$

Comparison with $\mathbf{G}^*\mathbf{G} = \mathbf{M}\mathbf{M}^*$ gives $\mathbf{M} = \mathbf{Y}\Sigma^{1/2}\mathbf{Y}^*$.

A suitable choice of cost function for robust controller design, that will not be biased to any particular frequency range, is given by

$$||\Delta||_\infty \leq ||(\mathbf{G} - \hat{\mathbf{G}})\mathbf{M}^{-1}||_\infty.$$

System Identification of JT-60U

This chapter describes the system identification experiments performed on the large JT-60U tokamak by the author in collaboration with Jo Lister, Ryuji Yoshino and Yukiharu Nakamura as presented in [6]. Advantages of the JT-60U tokamak are the long discharge duration, the very high accessible plasma current and temperature and the large plasma cross section, allowing investigation of plasma edge current and other effects. The size of JT-60U allows us to generalise the results of previous work to reactor-relevant conditions.

The machine is introduced in Section 5.1. Plasmaless and plasma RZIP models were constructed and the plasmaless model was tuned against experimental data, as described in Section 5.2. Corresponding frequency response measurements were made of the tokamak plant without plasma, as described in Section 5.3. The measurements were made inside the plasma control loop in order to identify purely the open-loop plasma response. A plasmaless model optimisation approach was then applied and is described in Section 5.4. The plasma experimental method is detailed in Section 5.5. Both Ohmically heated (Section 5.6) and neutral beam injection (NBI, Section 5.7) plasmas were used in separate experiments. Section 5.8 outlines the application of a similar model optimisation approach to the plasma model. The final results are presented in Section 5.9 where a model comparison is made. Section 5.10 gives a demonstration of a closed loop simulation with the optimised model and the work is concluded in Section 5.11.

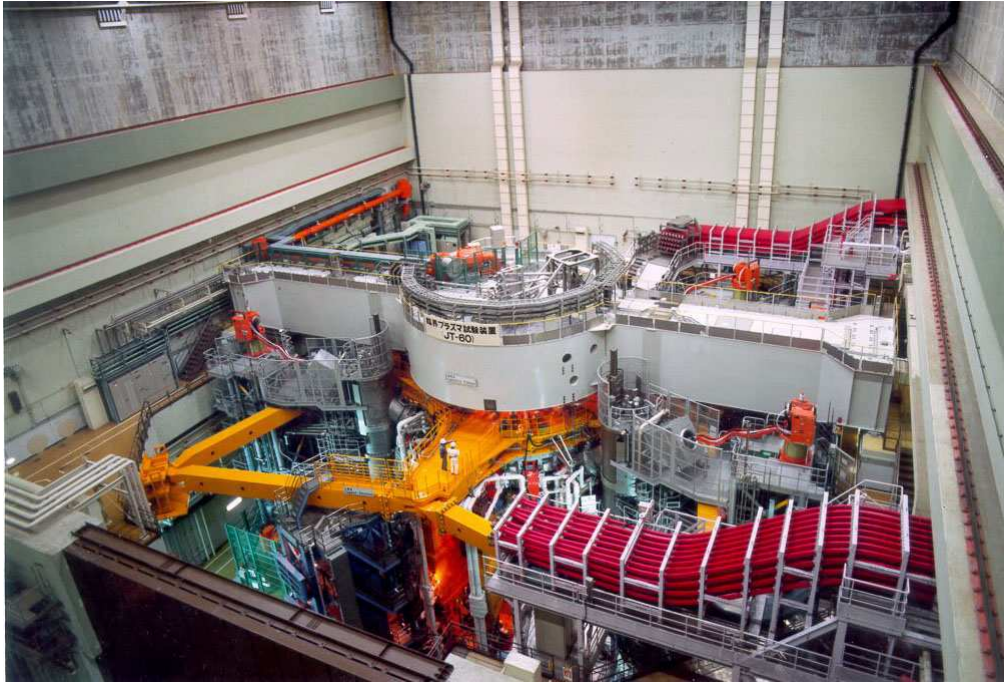


Figure 5.1: A photograph of the JT-60U tokamak. The two engineers give an idea of scale.

The experimental work was carried out in tandem with and acted as motivation for the modelling improvements described in Chapter 3. The model optimisation work was performed solely by Jo Lister and is included to give a coherent view of the whole body of work.

5.1. JT-60U

The JT-60U tokamak, in Naka, Japan, is the largest tokamak ever built, after JET¹. It has produced plasmas with currents up to 5MA. A photograph of the JT-60U tokamak is shown in Figure 5.1 and a cross-section is shown in Figure 5.2, which illustrates the position of the PF coils, the vacuum vessel, and the limiter.

There are 43 poloidal field coils, linked in series to form a total of five indepen-

¹Joint European Torus, in Abingdon, UK.

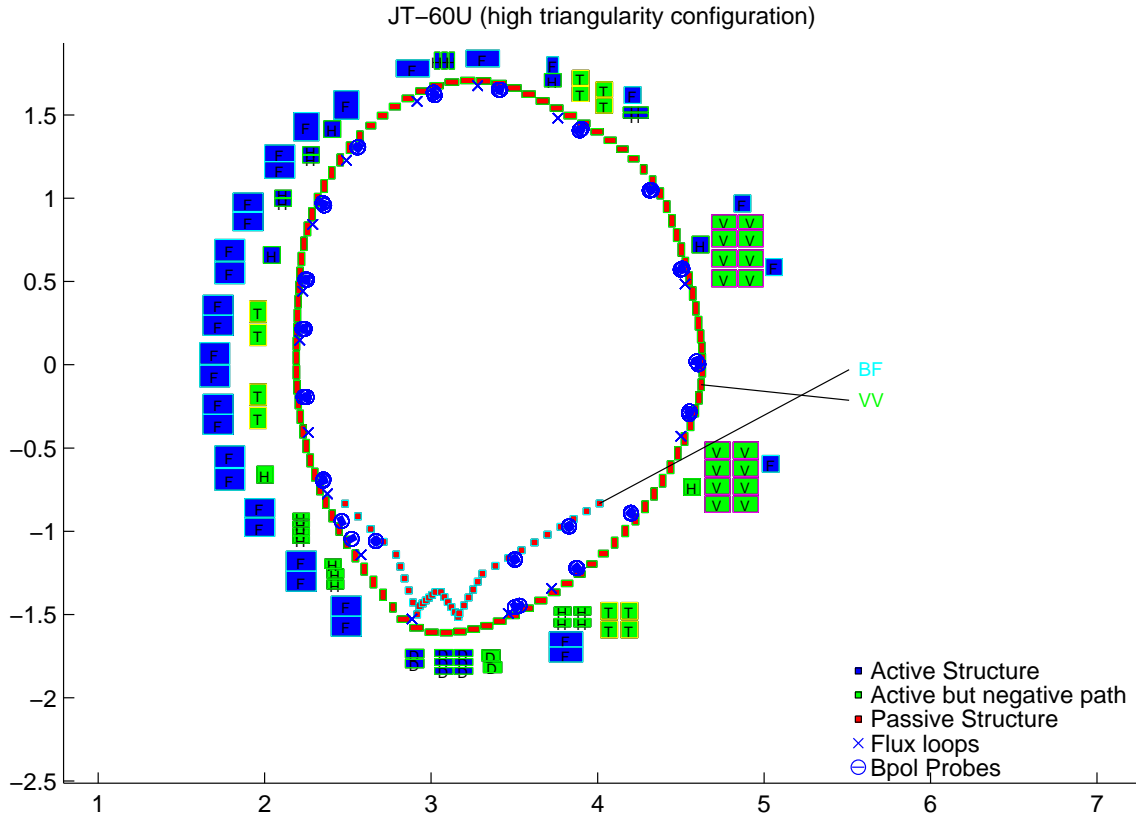


Figure 5.2: A cross sectional diagram of the JT-60U tokamak.

dently driven poloidal field coil-sets, named F, V, H, D and T. The figure also shows the twenty normal magnetic probes, the twenty tangential magnetic probes and the fifteen flux loops. The coil currents are measured by Rogowski coils, and there are Rogowski coils both inside and outside the vacuum vessel to measure plasma and vessel currents. The experiments were performed with the tokamak in high-triangularity configuration. The electromagnetic model of the JT-60U hardware was generated from information taken from the blueprints and other design specifications.

5.2. Preliminary plasmaless model calibration

Some magnetic field probe signals significantly and systematically disagreed with the plasmaless model predictions. It appeared that the worst discrepancies were correctable by a small change in the angle of the probe, at most 4.5 degrees. The plasmaless model was calibrated by using trapezoidal stimulation data to correct the \mathbf{C} matrix (the output matrix in the state-space model, see Section 3.3). The matrix element C_{ij} for each measurement j is given by the magnitude of the field produced by current i multiplied by $\cos(\theta)$, θ being the angle between the probe and the tangent to the field at the probe. To correct for an angle error ϵ we evaluate

$$Y_j = \sum_i C_{ij} \frac{\cos(\theta_i + \epsilon)}{\cos(\theta_i)}.$$

Scanning over values of ϵ to find the minimum of $(y_j - Y_j)^2$ where y_j is the output of probe j , summing over five different coil stimulations, gives the best value for ϵ . Cases where the minimum of the cost function is offset from zero by more than the cost function width are taken to be suitable for adjustment, since in these cases the cost function is sensitive to angle and the minimum is significantly away from zero. Twelve out of forty probes had their angles altered in the model. An open loop simulation of a typical plasmaless trapezoidal stimulation shot was performed as a check.

It should be noted that the agreement of the coil and vessel currents is necessary to obtain good agreement of the field and flux diagnostics. The effective PF coil resistances were obtained from the flat-top currents and the steady voltages, while the effective inductance was obtained from the ramp-up and ramp-down of the coil-set currents. The values obtained from this data were slightly different from the nominal values of the model, mostly because the connection leads to the power supplies are not accounted for in the nominal model. This approach to correcting the nominal values is sensitive to small offsets in the voltage measurements which

can have a significant effect on the estimated resistance.

5.3. Plasmaless identification experiments

5.3.1. Experimental design

A multisine stimulation was applied to the PF coil-sets. Since it is possible to programme only three frequencies on each coil-set for each shot (and one at a time only), the experiment was split into two shots (A004056 and A004061). The direct-current part of the experiment was simply repeated. A shot can contain a number of stimulations. Five different frequencies were used on five different coil-sets, in five separate stimulations. During a stimulation all coils were simultaneously excited by different frequencies. During an experiment no coil-set was excited at the same frequency twice. Thus, if the plant is linear, it is possible to determine the contribution of each coil-set to each diagnostic signal. The frequency range was chosen to cover as much as possible of the estimated bandwidth of the plant, within the limit set by the Nyquist sampling theorem, given an expected input signal sampling rate of $100Hz$. The frequencies chosen for the plasmaless experiment were $1.25Hz$, $3.2Hz$, $7.5Hz$, $19Hz$ and $43Hz$. A similar technique was successfully applied on the TCV fast internal coil system before [33]. A closed-loop model was used to estimate the response to the command currents I_{xCOM} so that the power supply voltage demand was reasonable. The controllers are described in Appendix C.2. The power supply limits are:

Power supply	limit / V
D	850
F	1250
DCW (for T coil)	1000
V	2500
H	550.

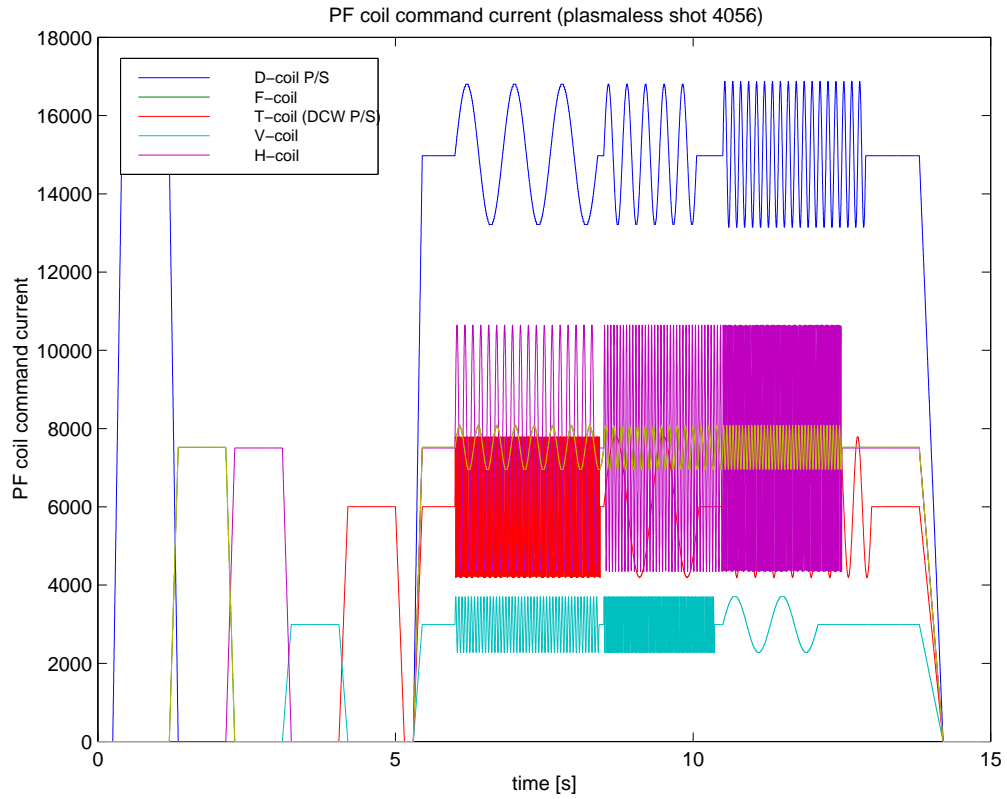


Figure 5.3: Reference currents for plasmaless shot 4056.

The command PF coil currents for shot 4056 are shown in figure 5.3, showing the first three stimulations.

5.3.2. Data analysis

A dummy identification of the open-loop plasma was successfully performed on the closed loop simulation to verify that the identification technique was correctly implemented. No evidence of aliasing at the higher frequencies was seen in the real experimental data so it was noted that the coils can be driven at higher frequencies for the plasma experiments if desired.

The stimulations in the two plasmaless shots are fitted to the chosen frequencies using the algorithm described in Section 4.1.1. The algorithm used to identify the plant transfer function is described in Section 4.1.2.

5.4. Plasmaless model optimisation

The model predictions agreed well but imperfectly with the data. Therefore the information in the experiments was used to improve the fit of the model to the data. This was achieved by making a parametric fit, which is optimal according to a cost function described in Chapter 4.

Another optimisation approach has been developed on TCV [34], in which triangulation techniques are applied to find the globally minimal set of changes to all the physical properties of the TCV model to reduce the discrepancies of the measurements at very low frequency. This was considered impossible on JT-60U because there are 43 physical coils with only five independent voltage inputs, leading to an underconstrained problem.

We have chosen not to modify the positions of the flux-loops and poloidal field probes, since these had been established very precisely and since the calibration described in Section 5.2 showed satisfactory agreement.

5.4.1. The optimisation process

The choice of cost function requires some engineering intuition. The criteria for choosing a cost function will be ultimately decided by the intended purpose of the model. To this end, two cost functions have been described in Chapter 4.

The input to the cost function is the set of differences between the experimental data and the model predictions. The differences must be normalised to take into consideration the differences in unit between signals.

A single parameter scan of selected electromagnetic model parameters was made in a specific order. Those parameters which appeared to generate the largest improvement to the cost functions were manually modified. The order was selected on the basis of the physical ordering and is:

- the self-inductances of the PF coil-sets
- the PF-set coil resistances
- the mutual inductances of the PF coil-sets
- the vessel eigenmode description.

Many parameters show almost no influence on the cost function. Rather than make large changes to these parameters to reduce the cost function by small amounts, model parameters close to their nominal values were left unless there were clear indications to modify the values.

5.4.2. Optimisation results

The model fit was most improved if the PF coil-set self inductances are modified by +23%, -4%, +2%, +1% and +24% for PF coil-sets D, F, T, V and H respectively. The two large positive corrections are understood as correcting for significant external coil impedances in the cables, power supplies and connections for the D and H-coils and the remaining corrections can be attributed to small errors in the calibration². The optimal PF coil-set resistances were found to be quite different from the values calculated in Section 5.2. However as mentioned before, the calibration results were sensitive to offsets in voltage measurements and the other tuning shows a flat minimum. Only some values in the PF coil-set mutual inductance matrix, involving the H coil-set, needed to be adjusted to show an improved fit to the experimental data as most of the coil-sets are only weakly coupled by design. The largest change to a coupling coefficient was 2.7%, between the D and H coils. Those mutual inductances were small in the nominal model, so large relative modifications are plausible. It was not necessary to iterate this process.

²This is not without precedent, [33].

The nominal poloidal field probe angles were then tuned. The model error was checked at the lowest frequency (the least perturbed by the shell current uncertainties) as the probe angle was changed to minimise the χ^2 cost function. 13 of the 39 probes used were uncorrected. 14 probes were corrected by 1-2 degrees, 11 probes were corrected by 3-5 degrees and one probe was adjusted by 8 degrees. Only those probes close to perpendicular to the field of a particular PF coil-set were considered for correction.

Finally, the vessel eigenmodes were corrected to adjust for differences between the nominal filament model and the physical vacuum vessel. The approach was the same as for the PF coil impedances. The adjustments to the inductance and resistance were small, ranging from -5% to +10%.

5.4.3. Possible causes for model error

The basic electromagnetic model of JT-60U was generated from the nominal parameters. Good agreement was obtained when initially comparing our experimental responses with our modelling. However, particular inconsistencies led us to re-examine the assumptions made in the electromagnetic model. One possible correction involves the assumption that a current would be uniformly distributed across the cross-section of a coil. The JT-60U PF coils are constructed from horizontal stacks of plates which are the width of the coil and there are non-centred cooling pipes in the coils. This implies that the current centroid is not necessarily centred in the coil cross-section. The nominal model was adjusted to take account of this effect. The skin effect in the PF conductors was also considered and discarded as small. The coupling of the PF coils to any metallic structures other than the vacuum vessel was ignored.

Other possible modifications to the electromagnetic model might involve metallic casing of the toroidal field coils and any non-axisymmetric structures near the magnetic probes. Small corrections could be attributed to three dimensional eddy

currents affecting the localised pick-up probes, the finite size of the magnetic probes *etc.* It is imperative to ensure that the plasmaless model is as close as possible to the actual data so that any errors are not wrongly attributed to the plasma model at a later stage.

5.5. Plasma experiments

To create a plasma model of JT-60U the equilibrium current distribution is needed. This was obtained using the FBEQU equilibrium reconstruction code.

The nonlinear estimator algorithm (see Appendix C.1) uses a combination of the directly measured PF coil-set and plasma currents, and the magnetic field probes to estimate four control parameters dR , dZ , X_p , and δ (also called CL1), which are the plasma radial displacement, the vertical displacement, the X-point position and a measure of the triangularity (δ) respectively. I_p is also a control parameter. Since the estimator is nonlinear it is necessary to linearise it about the plasma equilibrium at a particular time. The resulting linearisation gave near perfect comparison with the full estimator and database values in the region of operation.

To implement a good closed loop model, useful in experimental design, the controllers must be modelled. The JT-60U control algorithms are described in Appendix C.2.

As before, the algorithms in Chapter 4 are used to determine the plant transfer function.

5.6. Ohmically heated plasma experiments

The frequencies used for the two plasma shot experiments were 3Hz, 7Hz, 16Hz, 35Hz and 80Hz. The frequencies were raised from the plasmaless values since there was no evidence of aliasing in the plasmaless experimental data.

The plasma conditions were: $I_p = 1.2MA$, $\kappa = 1.33$, $\delta = 0.28$, $q_{95} = 3.9$, $\beta = 0.06$, $l_i = 1.2$, $L_p = 5.54mH$ and $n_e = 2 \times 10^{19}m^{-3}$ ³. Rather than modulate the power supply demand signals, the reference signals for the five control parameters used on JT-60U were modulated. The amplitudes of the control parameter variations were chosen to provide a significant signal on the measurements, without excessively perturbing the operation, and chosen to reduce with frequency to avoid excessive voltage demand signals. Typical values for the control parameter excursions were: 10-50kA for I_p , 2-5cm for R , 2-5cm for z , 0.05-0.1 for δ and 3-5cm for X_p .

A test Ohmic discharge (E034993) was made to check the useful range of frequency stimulation and noise levels. It was found that the PF coil-set voltages were in a reasonable range, there was no sign of harmonics over the driven frequencies and there was excellent signal to noise ratio on all frequencies, including the highest. The frequencies were therefore unchanged for the experiment ohmic discharges E035009 and E035023. The experiments are summarised in figures 5.4 and 5.5.

5.7. Neutral beam injection (NBI) plasma experiments

Two more sets of experiments were carried out in the presence of 12MW of neutral beam injection heating (discharges E35561, E35574). The experiments are summarised in figures 5.6 and 5.7. With these experiments we hoped to increase the plasma edge conductivity. The plasma equilibrium was similar ($I_p = 1.19MA$, $q_{95} = 2.9$, $\kappa = 1.44$, $\delta = 0.23$, $l_i = 1.01$, $\beta = 0.41$, $L_p = 5.34mH$) and the experimental technique was unchanged. The increase in the electron temperature (T_e) at the edge was smaller than hoped for since the discharge remained in L-mode with only $T_e = 2.5keV$ on axis, although the value of β was significantly greater. The result cannot therefore be considered definitive concerning the importance of edge conductivity. However, it does provide substantial confirmation of the Ohmic discharge results.

³ n_e is the electron density.

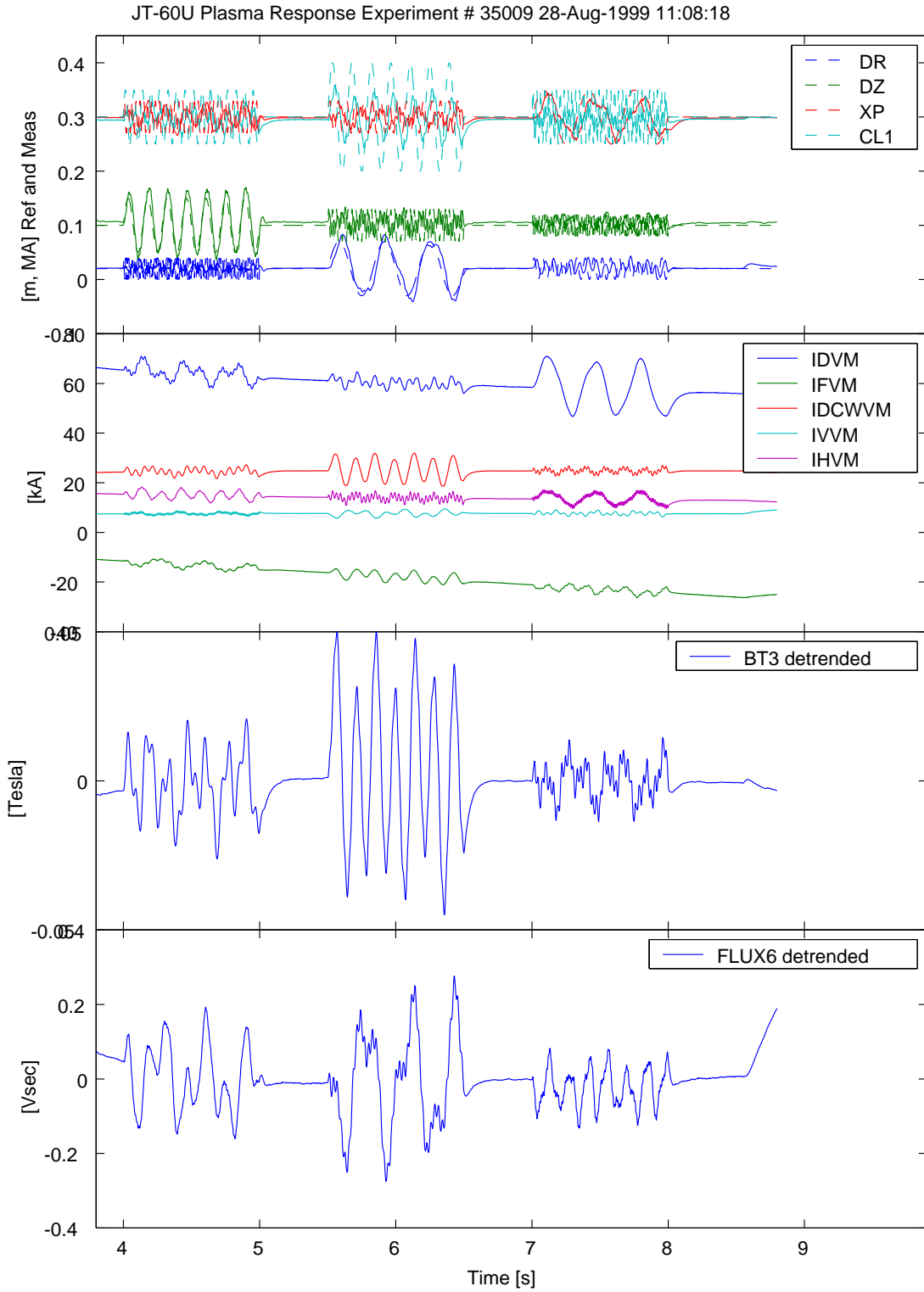


Figure 5.4: Summary of ohmic discharge 35009.

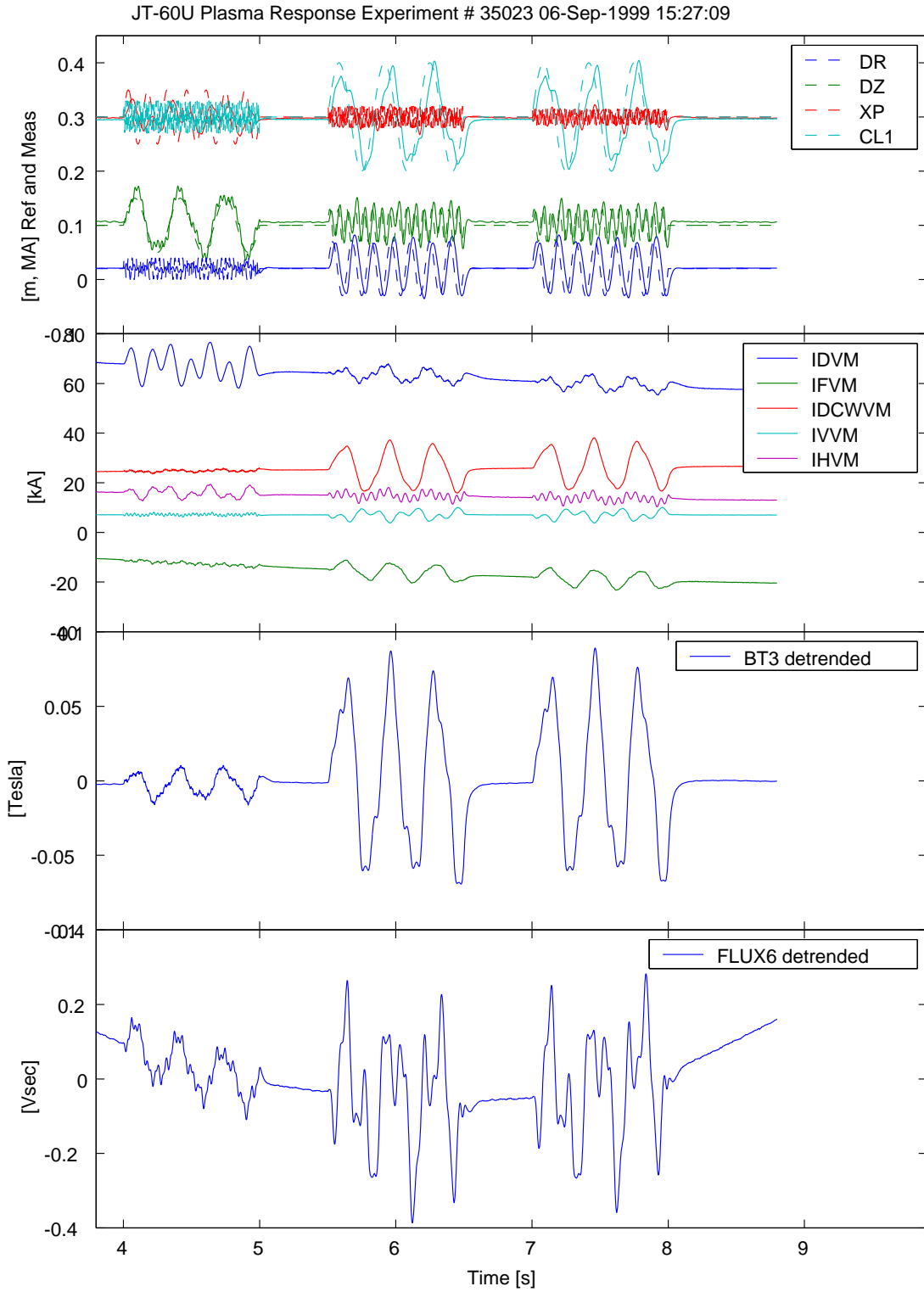


Figure 5.5: Summary of ohmic discharge 35023.

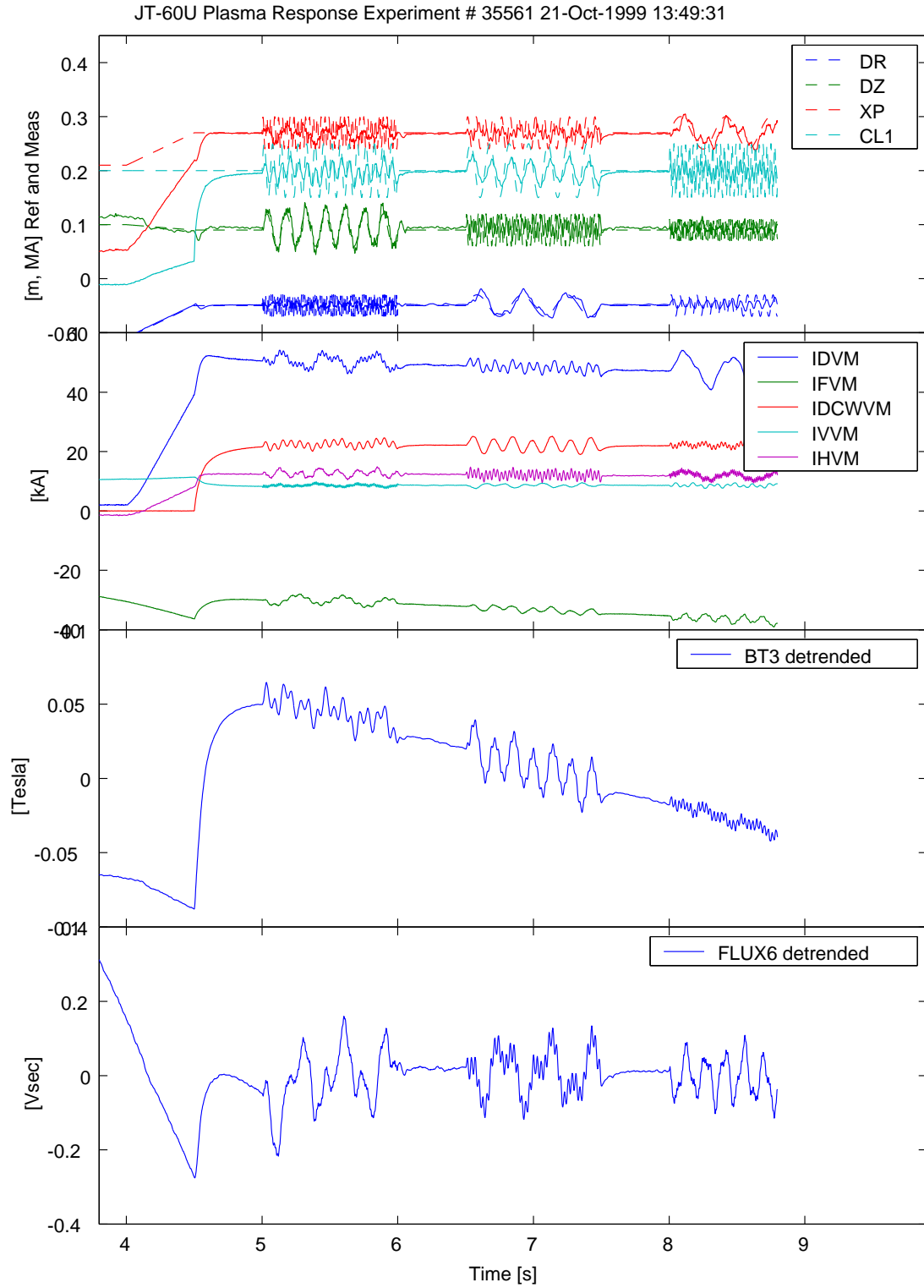


Figure 5.6: Summary of neutral beam injection discharge 35561.

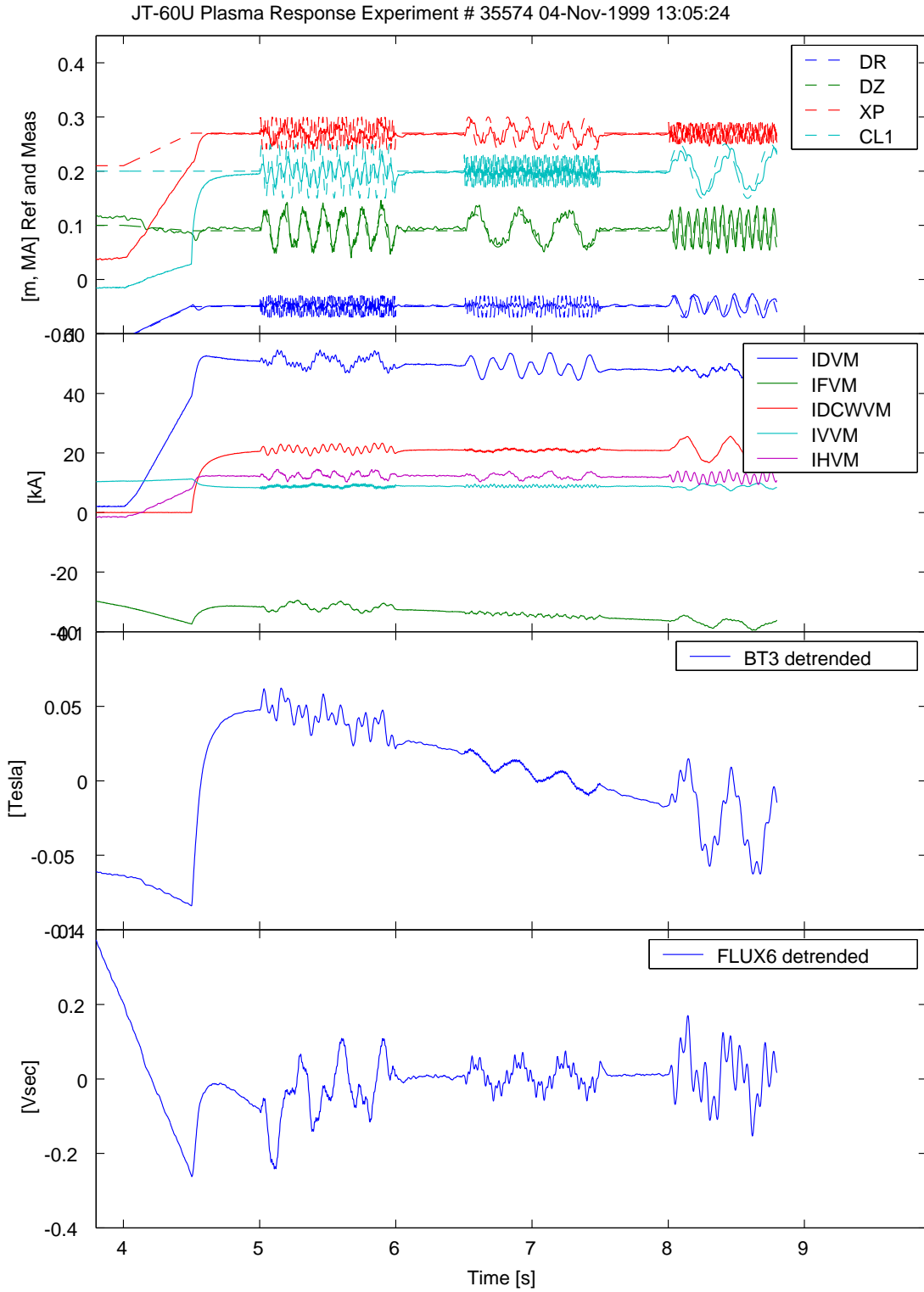


Figure 5.7: Summary of neutral beam injection discharge 35574.

5.8. Grey-box modelling

Searching within the space of models representable in the form of equation 3.31 provides the optimal model among all linear models with the same choice of states. The effect of varying coefficients in the RZIP model has been investigated previously [5]. Given a perfect plasmaless model, it is possible to float the dominantly plasma terms (the bottom right hand four or nine terms of \mathcal{M} , and any plasma terms in \mathcal{R} ; see equation (3.31)). This gives an estimate of the best model. This work has been performed and is presented in [6]. The results are presented here alongside the nominal model.

5.9. Results and model comparison

Bode plots of the identification results are compared with nominal model and grey-box model predictions in figures 5.8 to 5.12 for each control parameter. The nominal model used is described in Chapter 3, with the plasmaless optimisation described in Section 5.3 applied. The grey-box model used is the one found in Section 5.8.

The model prediction is overall very accurate, although the I_p response is somewhat stronger than expected for the D, F and H coils. Also the X-point position response to the F coil is stronger than predicted.

5.10. Closed-loop model of JT-60U

It is interesting to see whether the validated open-loop tokamak model, when combined with a model of the controller, can successfully simulate the closed-loop response in the time-domain. The controller used in the flat-top regime controls the vertical instability, and is designed to track the five parameters, dR , dZ , I_p , X_p and δ . These parameters are determined in real-time by the state

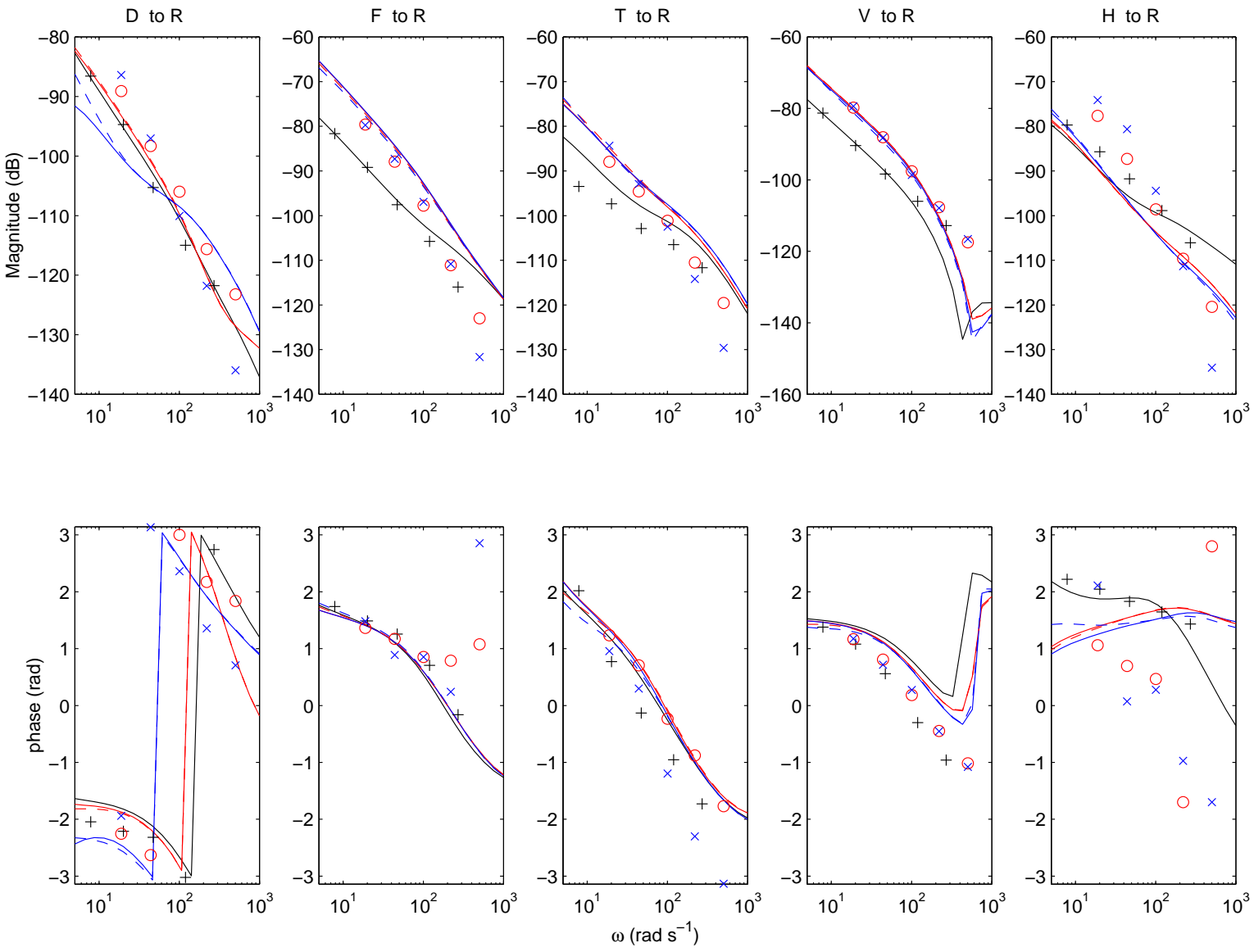


Figure 5.8: Model comparison for control parameter R : (+) plasmaless data; (-) plasmaless model; (o) Ohmic data; (- -) Ohmic nominal model; (- -) NBI nominal model; (- -) NBI optimised model

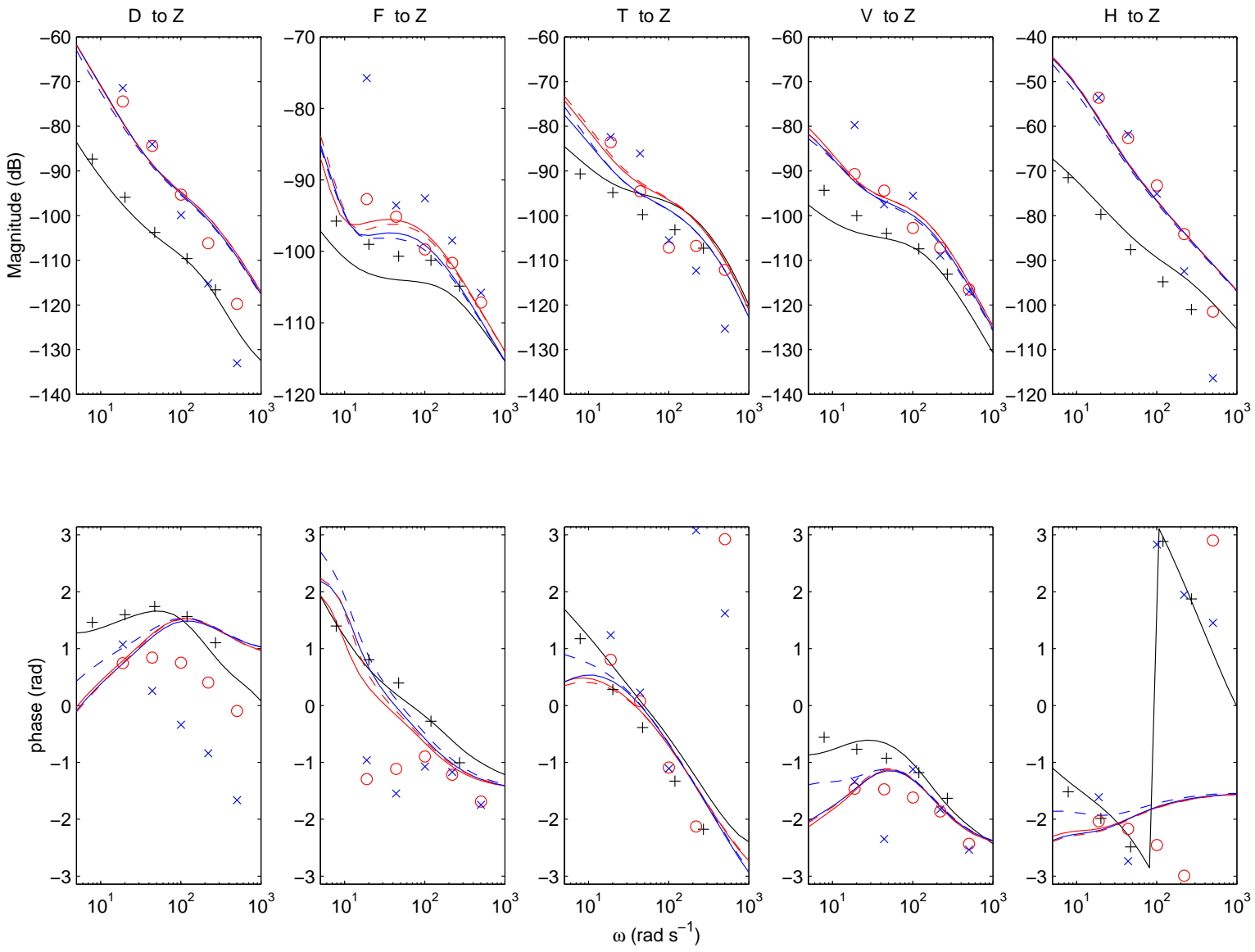


Figure 5.9: Model comparison for control parameter z : (+) plasmaless data; (-) plasmaless model; (o) Ohmic data; (- -) Ohmic nominal model; (- -) NBI nominal model; (- -) NBI optimised model

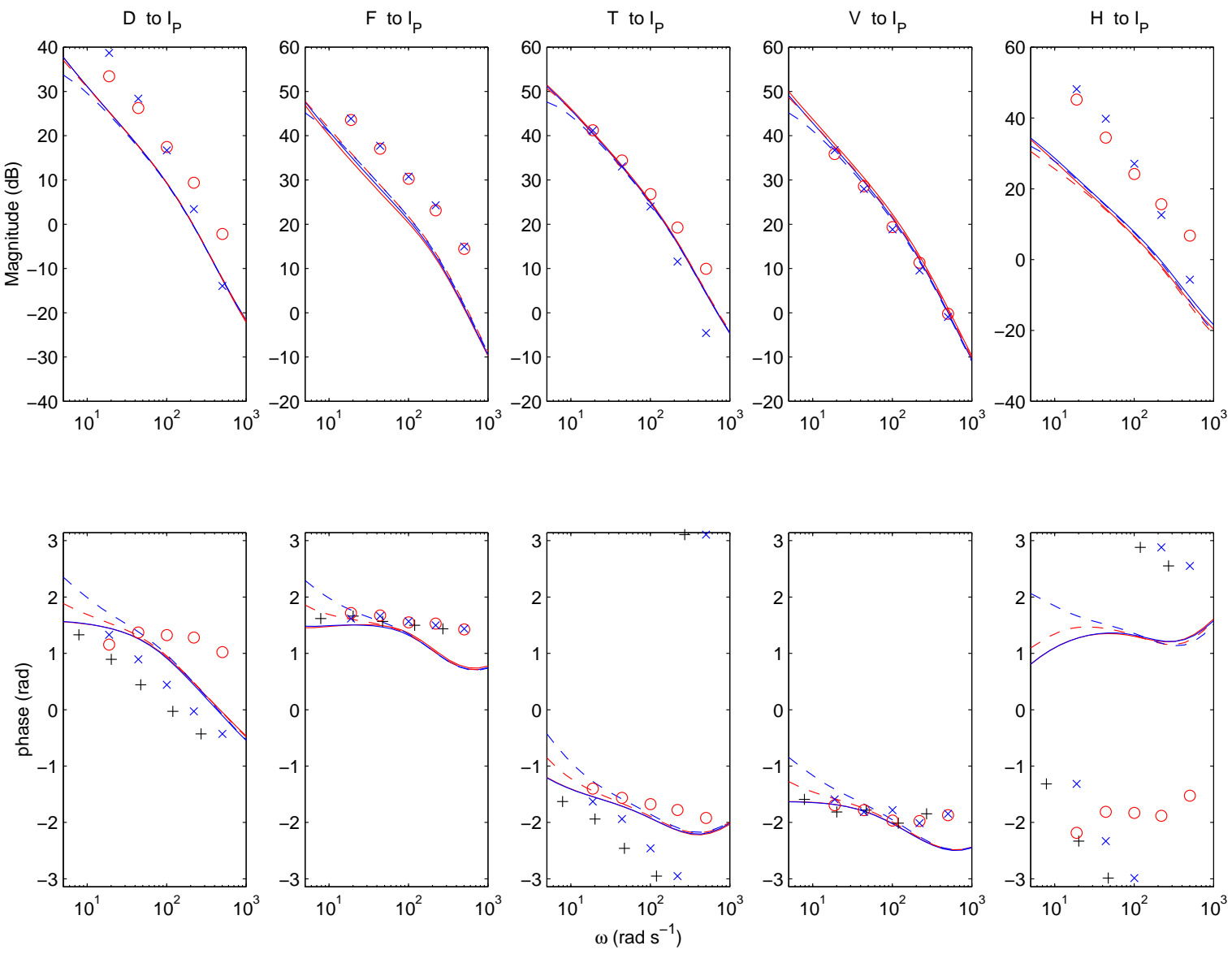


Figure 5.10: Model comparison for control parameter I_p : (+) plasmaless data; (-) plasmaless model; (o) Ohmic data; (- -) Ohmic nominal model; (-) Ohmic optimised model; (x) NBI data; (- -) NBI nominal model; (-) NBI optimised model

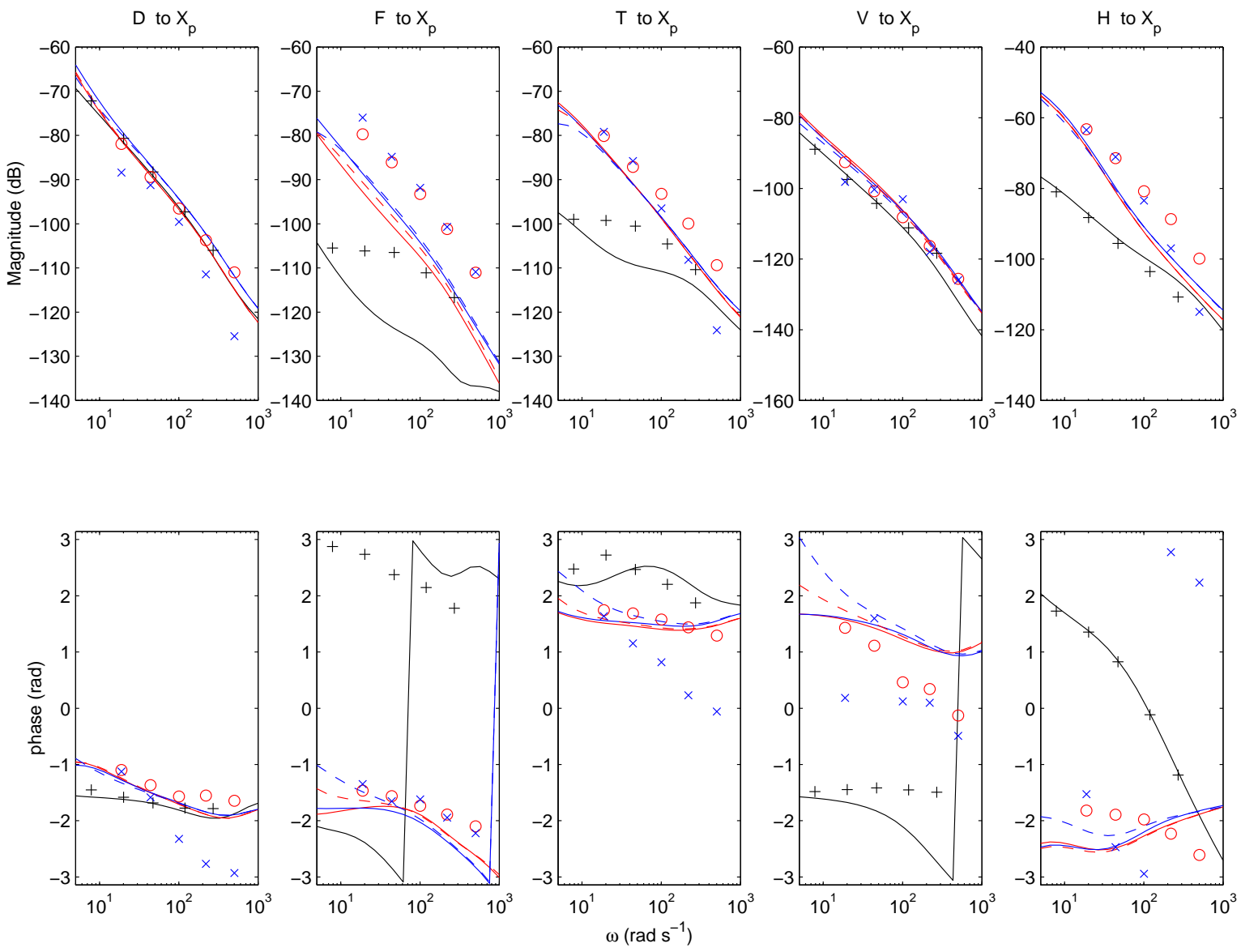


Figure 5.11: Model comparison for control parameter X_p : (+) plasmaless data; (o) Ohmic data; (x) NBI data; (---) Ohmic nominal model; (---) NBI nominal model; (—) optimised model

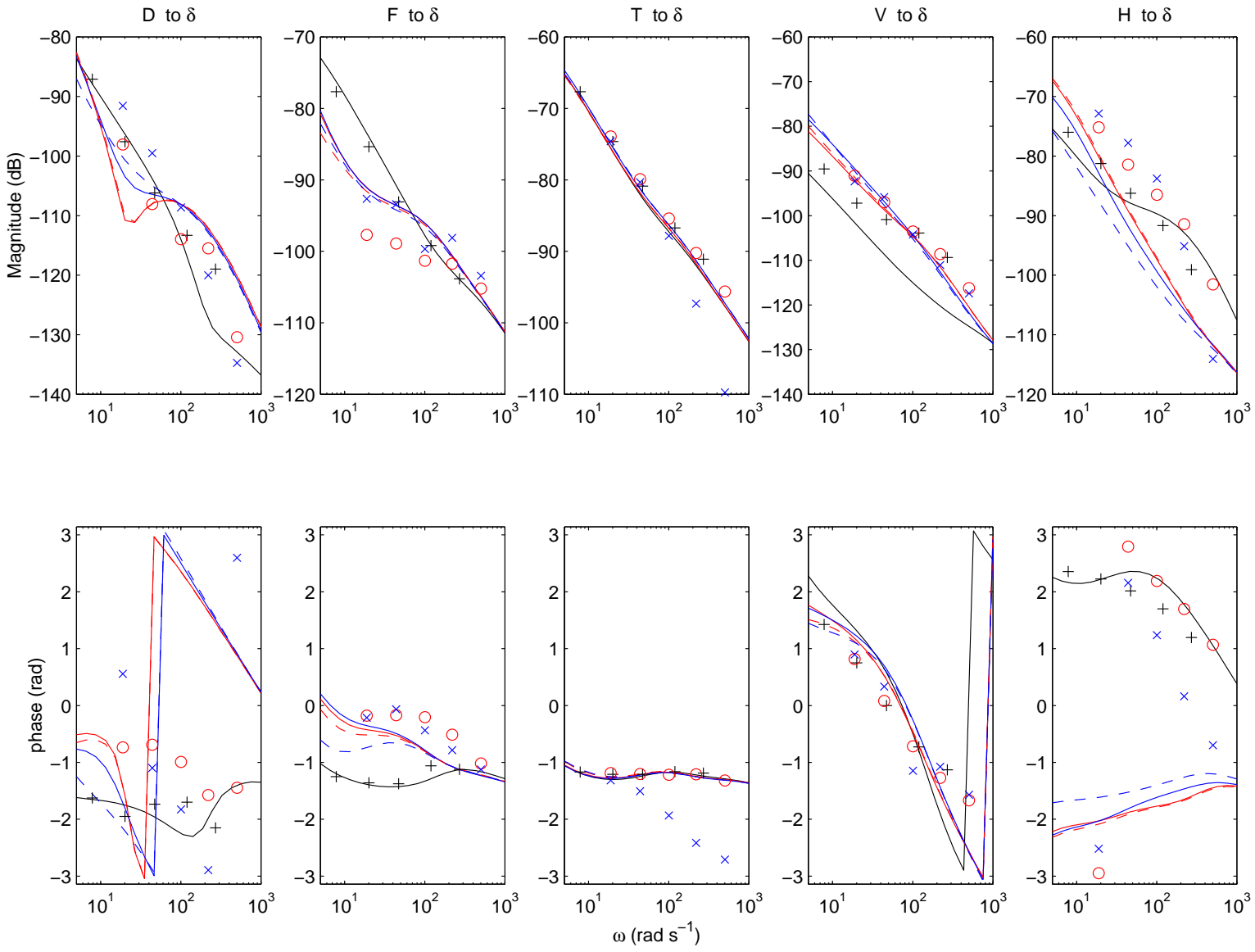


Figure 5.12: Model comparison for control parameter δ : (+) plasmaless data; (-) plasmaless model; (o) Ohmic data; (-) Ohmic nominal model; (- -) Ohmic optimised model; (x) NBI data; (-) NBI nominal model; (- -) NBI optimised model

estimator from a combination of normal and tangential poloidal magnetic field probe measurements, the D and T coil currents and the plasma current.

For the closed-loop simulation an RZIP model was made, linearised about the flat-top of Ohmic discharge E035023, at 3.9 seconds. The estimator was linearised about the same point and incorporated into the \mathbf{C} matrix. The optimal grey-box model was used.

A simulation of shot E034993 was made, this shot being an Ohmic shot similar to the others but not used in the identification experiments or the grey-box modelling. As such it is a completely independent data set, suitable for comparison. The equilibrium values of the coil voltages, coil currents, and control parameters, were defined as the average values between 3.7-3.9 seconds, before stimulation of the command signal began.

Figure 5.13 shows the results of the simulation compared with the experimental data. The command signal is shown in red, the actual experimental response in green, and the simulation in black. Linear trends and offsets have been removed to aid visual comparison, although small. The closed-loop simulation of the estimator response is extremely good. The response of the coil voltages and currents are similarly well-modelled.

5.11. Discussion

The work presented in this chapter extends previous work by applying a system identification procedure to the large JT-60U tokamak. The work on TCV has now been validated on the larger and hotter JT-60U tokamak with a different PF coil system. The frequency response was predicted with a high degree of accuracy by a model derived from first principles. This model was then optimised by parametric fit and closed-loop simulations showed excellent agreement with experiment.

The nominal model can be seen to lay close to the best-fit model, and although

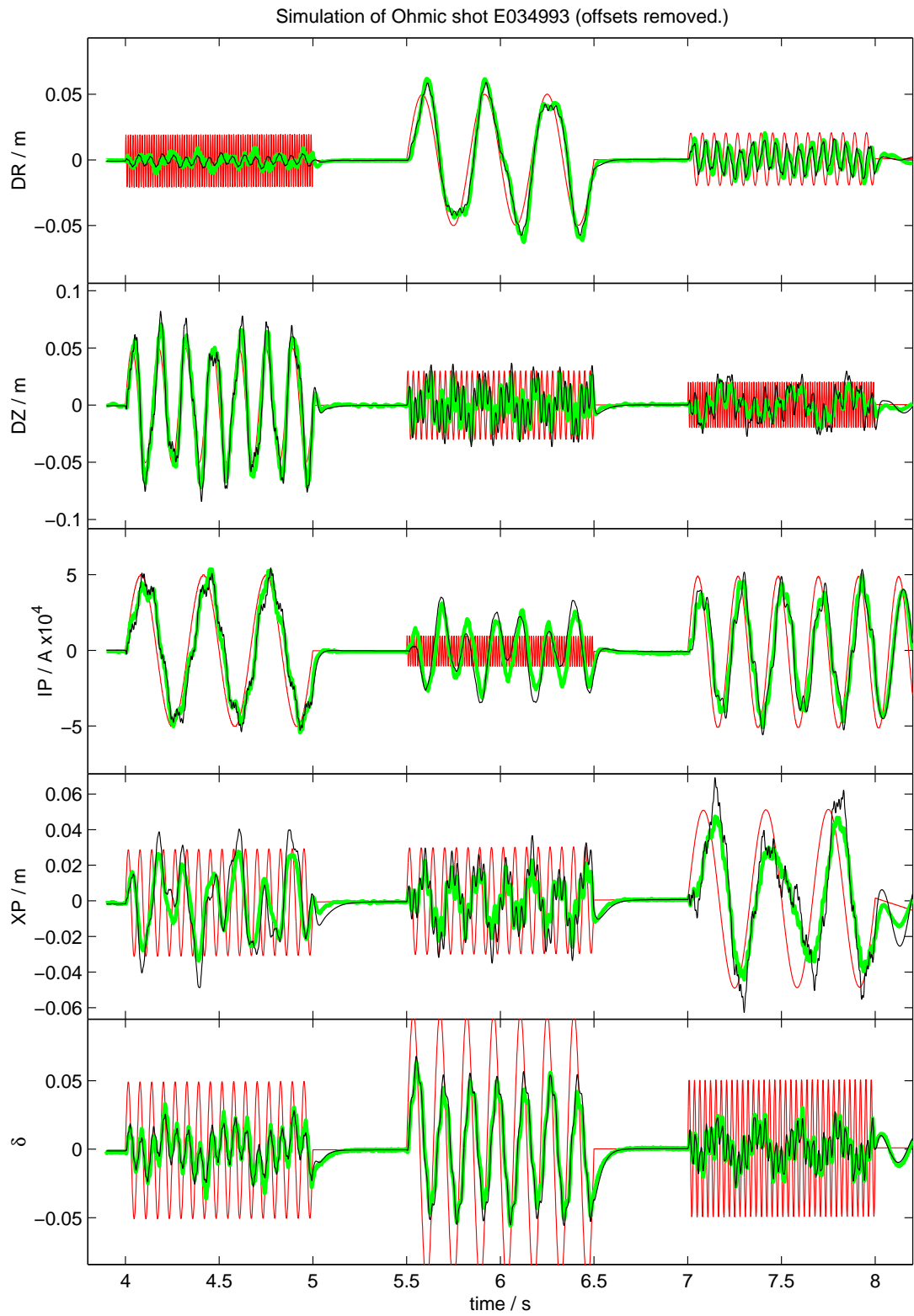


Figure 5.13: Modelled data (-) compared with real data (--) and the command signal (-).

both give excellent predictions in the time and frequency domain, there are predictive errors with the I_p response to the H, F and D coils only. The X_p response to the F and H coils is also imperfect, although less so. It is unclear why this is so.

Having said that, the modelling of the vertical position response is superb and this gives confidence that a stabilising controller could be designed using the model. The radial response is well modelled and yet could perhaps be slightly improved by including the toroidal magnetic field \mathbf{B}_T in the model.

For the purposes of shape, current and position control by the PF coils, no essential difference was found between the Ohmically and NBI heated plasmas with quite different values of β .

Control of TCV

This chapter is concerned with the design and evaluation of a control system for the TCV tokamak [8]. The linearised model described in Chapter 3 will be used as a basis for designing the controller. It will be tested on a nonlinear code based on a sequence of Grad-Shafranov equilibria [35].

Although the controller synthesis procedure is established, the application of this particular \mathcal{H}_∞ controller design methodology to TCV has not been performed before. Also to the author's knowledge this represents the first real-world application of the controller reduction procedure described in [7].

6.1. Control objectives

The primary interest of this work is the study of control systems for elongated plasmas in TCV. As with all elongated plasmas, the equilibrium under consideration is unstable in the vertical position and so the open-loop plant is characterised by a single unstable pole that requires stabilisation. One of the major challenges is the uncertainty in the modelling of the tokamak plasma dynamics together with the fact that these dynamics vary with the operating conditions. For this reason, it is important that the proposed control system has adequate robust stability and performance margins. We will also seek to decouple the five outputs that characterise the plasma shape, position and current. Ideally, we would like to be

able to implement variation in any one of these outputs without influencing the others.

6.2. The RZIP model of TCV

The RZIP model plus power supplies has been qualified against the TCV equilibrium 13333 [5]. The plasma in this shot is well understood and unstable with a moderate growth rate measured and predicted by RZIP as approximately $100s^{-1}$; the equilibrium profile is shown in Figure 6.1. The five control parameters used for controlling this type of equilibrium on TCV are:

- p_{vert} , the radial flux imbalance (a radial position measurement);
- tri_{out} , the outboard field curvature;
- tri_{in} , the inboard field curvature;
- zI_p , the product of plasma vertical position and current;
- I_p , the plasma current.

The particular RZIP model used for controller design assumes a superconducting plasma (see Section 3). Figure 6.2 shows the singular value plot of the TCV RZIP model with 18 inputs and 5 outputs. It can be seen from this figure that there is a large spread in the singular value magnitudes. As is standard practice, we will seek to reduce the transfer function's condition number by scaling. Indeed, this will be the initial step of the loop shaping design.

A characterising feature of models with zero plasma resistance (such as those based on ideal MHD assumptions) is the introduction of uncontrollable modes at the origin. The underlying mechanism that gives rise to these modes is described briefly in Appendix D using simple circuit theoretic arguments. Since these poles

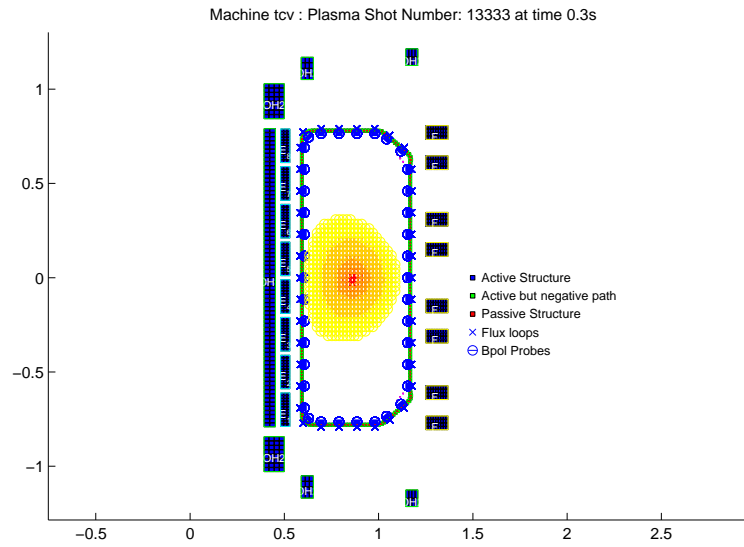


Figure 6.1: TCV equilibrium 13333

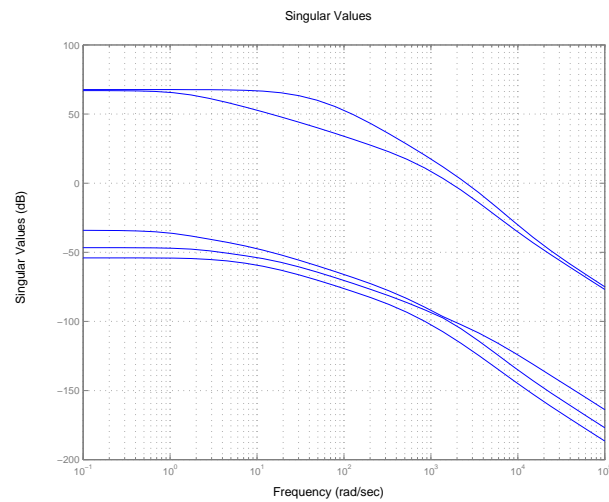


Figure 6.2: Singular value plot of TCV RZIP model

cannot exist in reality, we will remove them from the RZIP model using standard model reduction algorithms [36].

The order of the plant after reduction by the method described in Section 3.2 is 76. This degree of reduction was considered reasonable as it significantly reduced the plant order without discernibly affecting the transfer function.

6.2.1. Removal of poles at origin

The removal of the poles at the origin can be achieved by the Schur method of model reduction. We wish to find a realisation of $\mathbf{G}(s)$ that enables us to truncate the modes responsible.

In general

$$\mathbf{G}(s) \stackrel{s}{=} \left[\begin{array}{c|c} A & B \\ \hline C & D \end{array} \right] \xrightarrow{V} \left[\begin{array}{c|c} V'AV & V'B \\ \hline CV & D \end{array} \right] \quad (6.1)$$

where V is chosen such that

$$V' = V^{-1}.$$

Firstly we choose V such that \mathbf{G} will be in block ordered real Schur form,

$$\mathbf{G} \stackrel{s}{=} \left[\begin{array}{c|c} A & B \\ \hline C & D \end{array} \right] \xrightarrow{V} \left[\begin{array}{cc|c} A_{11} & A_{12} & B_1 \\ 0 & A_{22} & B_2 \\ \hline C_1 & C_2 & D \end{array} \right] \quad (6.2)$$

where A_{22} just relates to the states associated with the zero eigenvalues.

The transformation needed is

$$\mathbf{G} \stackrel{s}{=} \left[\begin{array}{cc} I & -X \\ 0 & I \end{array} \right] \left[\begin{array}{cc|c} A_{11} & A_{12} & B_1 \\ 0 & A_{22} & B_2 \\ \hline C_1 & C_2 & D \end{array} \right] \left[\begin{array}{cc} I & X \\ 0 & I \end{array} \right] \quad (6.3)$$

$$= \left[\begin{array}{cc|c} A_{11} & (A_{11}X - XA_{22} + A_{12}) & B_1 - XB_2 \\ 0 & A_{22} & B_2 \\ \hline C_1 & C_2 + C_1X & D \end{array} \right],$$

where we wish to find X such that the the Sylvester equation

$$A_{11}X - XA_{22} + A_{12} = 0$$

is satisfied.

This choice of X gives the required realisation of \mathbf{G} ,

$$\mathbf{G}(s) \stackrel{s}{=} \left[\begin{array}{cc|c} A_{11} & 0 & B_1 - XB_2 \\ 0 & A_{22} & B_2 \\ \hline C_1 & C_2 + C_1X & D \end{array} \right].$$

The latter part of the state space system pertaining to the neutrally stable modes can simply be truncated. This gives the reduced model

$$\hat{\mathbf{G}} \stackrel{s}{=} \left[\begin{array}{c|c} A_{11} & B_1 - XB_2 \\ \hline C_1 & D \end{array} \right].$$

6.2.2. Modelling of power supplies

The poloidal field coil power supplies are approximated by single pole filters, expressed in the state-space form as

$$A = -diag\left(\frac{1}{\tau_c}\right), \quad B = diag\left(\frac{1}{\tau_c}\right), \quad C = I, \quad D = I$$

where $\tau_c = 0.3ms$ for all PF coil power supplies used. Throughout the plant referred to is the tokamak including the power supplies.

6.3. Robust controller design

Motivated by its simplicity, we will use the the \mathcal{H}_∞ normalised coprime factorisation method [30, 37] for the controller synthesis. In many respects the research presented here is an evolution of that presented in [38]. After completing the loop shaping and controller synthesis, we will make use of some recent research [7] that facilitates a reduction in the controller order with guaranteed properties.

6.3.1. Normalised left coprime factorisation perturbations

A set of plant models that will be used to represent the machine will be characterised in terms of a perturbed normalised coprime factorisation. We suppose that \mathbf{G} is the nominal plant model. Then

$$\mathbf{G} = \mathbf{M}^{-1}\mathbf{N} \quad (6.4)$$

is a normalised left coprime factorisation of \mathbf{G} if $\mathbf{M}, \mathbf{N} \in \mathcal{H}_\infty$ are coprime and satisfy

$$\mathbf{M}\mathbf{M}' + \mathbf{N}\mathbf{N}' = \mathbf{I}.$$

Given such a factorisation we define the model set

$$\mathcal{G}_\gamma = \left\{ (\mathbf{M} - \boldsymbol{\Delta}_M)^{-1}(\mathbf{N} + \boldsymbol{\Delta}_N) : \begin{array}{l} [\boldsymbol{\Delta}_N \ \boldsymbol{\Delta}_M] \in \mathcal{H}_\infty \\ \|[\boldsymbol{\Delta}_N \ \boldsymbol{\Delta}_M]\|_\infty < \gamma^{-1} \end{array} \right\}. \quad (6.5)$$

6.3.2. The optimisation problem

Our aim is to design a controller that is optimal in the sense of minimising γ , in order to maximise the size of admissible perturbations as defined by (6.5). From

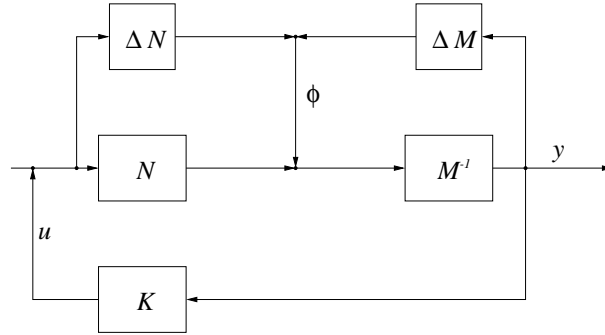


Figure 6.3: Robust controller design problem

Figure 6.3 we see that

$$\begin{bmatrix} u \\ y \end{bmatrix} = \mathcal{H}(\mathbf{G}, \mathbf{K})\phi, \quad \phi = [\Delta_N \quad \Delta_M] \begin{bmatrix} u \\ y \end{bmatrix},$$

where

$$\mathcal{H}(\mathbf{G}, \mathbf{K}) = \begin{bmatrix} \mathbf{K} \\ \mathbf{I} \end{bmatrix} (\mathbf{I} - \mathbf{G}\mathbf{K})^{-1} \mathbf{M}^{-1}. \quad (6.6)$$

From the small gain theorem [30], the condition

$$\|\mathcal{H}(\mathbf{G}, \mathbf{K})\|_{\infty} \leq \gamma \quad (6.7)$$

will ensure that the closed loop will be stable for all plants in the model set \mathcal{G}_{γ} . To maximise the robustness of the closed loop, we require a controller that minimises γ .

6.3.3. Parameterisation of all suboptimal controllers

The following result presented in [7] gives a parameterisation of all suboptimal controllers.

Lemma 6.1. [7, 30, 37, 39] *If \mathbf{G} has a minimal realisation $\mathbf{G} \stackrel{s}{=} (A, B, C, 0)$, there will exist unique stabilising and positive definite solutions X, Y to the algebraic*

Riccati equations

$$A'X + XA - XBB'X + C'C = 0 \quad (6.8)$$

$$AY + YA' - YC'CY + BB' = 0 \quad (6.9)$$

with

$$\gamma_{opt} = \sqrt{1 + \lambda_{max}(XY)} \geq 1. \quad (6.10)$$

For $\gamma > \gamma_{opt} \geq 1$ define $\beta = \sqrt{1 - \gamma^{-2}}$ so that $0 < \beta \leq 1$ and define $Z = (I - \gamma^{-2}\beta^{-2}YX)^{-1}$. We can then parameterise all suboptimal controllers by

$$\begin{aligned} \mathbf{K} &= (\Theta_{11}\mathbf{Q} + \Theta_{12})(\Theta_{21}\mathbf{Q} + \Theta_{22})^{-1}, \\ \mathbf{Q} &\in \mathcal{RH}_\infty, \quad \|\mathbf{Q}\|_\infty < \gamma, \end{aligned} \quad (6.11)$$

where we define

$$\Theta = \begin{bmatrix} \Theta_{11} & \Theta_{12} \\ \Theta_{21} & \Theta_{22} \end{bmatrix} \stackrel{s}{=} \left[\begin{array}{c|cc} A - BB'X & ZB & \beta^{-1}ZYC' \\ \hline -\beta^{-2}B'X & I & 0 \\ \beta^{-2}C & 0 & \beta^{-1}I \end{array} \right] \in \mathcal{RH}_\infty. \quad (6.12)$$

We will also require

$$\Theta^{-1} \stackrel{s}{=} \left[\begin{array}{c|cc} Z(A - YC'C)Z^{-1} & ZB & ZYC' \\ \hline \beta^{-2}B'X & I & 0 \\ -\beta^{-1}C & 0 & \beta I \end{array} \right] \in \mathcal{RH}_\infty \quad (6.13)$$

in the sequel.

Equation (6.11) gives the central controller in the form of a right coprime factorisation, by taking $\mathbf{Q} = 0$,

$$\mathbf{K}_{11} = \Theta_{12}\Theta_{22}^{-1} \stackrel{s}{=} \left[\begin{array}{c|c} A - BB'X - \beta^{-2}ZYC'C & ZYC' \\ \hline -\beta^{-2}B'X & 0 \end{array} \right]. \quad (6.14)$$

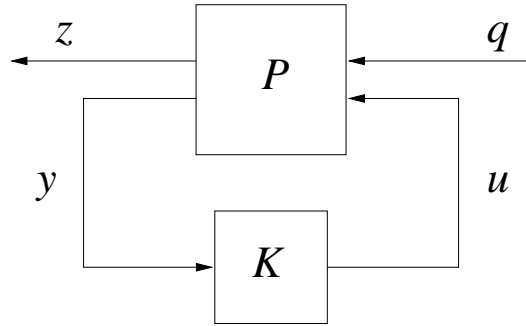


Figure 6.4: Lower LFT framework

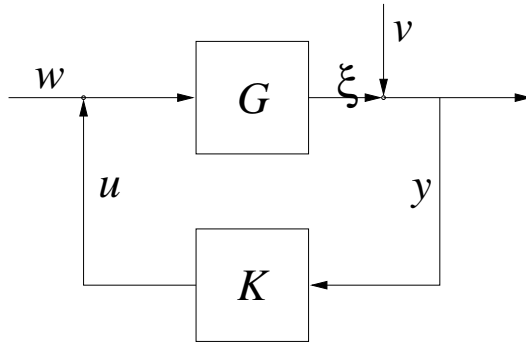


Figure 6.5: Closed-loop configuration, single degree of freedom controller

We will use this controller throughout.

6.3.4. The controlled plant

The plant and controller can be represented in lower LFT form as in Figure 6.4.

It is clear from the figure that \mathbf{P} can be partitioned as

$$\begin{bmatrix} z \\ y \end{bmatrix} = \begin{bmatrix} \mathbf{P}_{11} & \mathbf{P}_{12} \\ \mathbf{P}_{21} & \mathbf{P}_{22} \end{bmatrix} \begin{bmatrix} q \\ u \end{bmatrix}.$$

It is easily shown that

$$z = (\mathbf{P}_{11} + \mathbf{P}_{12}\mathbf{K}(\mathbf{I} - \mathbf{P}_{22}\mathbf{K})^{-1}\mathbf{P}_{21}) q.$$

From Figure 6.5 it is simple to express \mathbf{P} as

$$\begin{bmatrix} \begin{bmatrix} y \\ u \end{bmatrix} \\ y \end{bmatrix} = \begin{bmatrix} \mathbf{G} & \mathbf{I} & \mathbf{G} \\ \mathbf{0} & \mathbf{0} & \mathbf{I} \\ \mathbf{G} & \mathbf{I} & \mathbf{G} \end{bmatrix} \begin{bmatrix} \begin{bmatrix} w \\ v \end{bmatrix} \\ u \end{bmatrix}. \quad (6.15)$$

We can choose the disturbance $v = -r$, where r is a reference signal to track so that the controller minimises the control error $y = \xi - r$. w is a disturbance to the coil inputs u .

Substituting $\mathbf{G} = C(sI - A)^{-1}B + D$ into \mathbf{P} gives

$$\mathbf{P} \stackrel{s}{=} \left[\begin{array}{c|cc} A & [B \ 0] & B \\ \hline C & [D \ I] & [D] \\ 0 & [0 \ 0] & [I] \\ C & [D \ I] & D \end{array} \right]. \quad (6.16)$$

A minimal state-space realisation of the closed loop transfer function is given by [30]

$$\mathcal{F}_l(\mathbf{P}, \mathbf{K}) \stackrel{s}{=} \left[\begin{array}{cc|c} A + B\tilde{D}MC & B(I + \tilde{D}MD)\tilde{C} & [B \ 0] + B\tilde{D}M[D \ I] \\ \tilde{B}MC & \tilde{A} + \tilde{B}MD\tilde{C} & \tilde{B}M[D \ I] \\ \hline \begin{bmatrix} C \\ 0 \end{bmatrix} + \begin{bmatrix} D \\ I \end{bmatrix} \tilde{D}MC & \begin{bmatrix} D \\ I \end{bmatrix} (I + \tilde{D}MD)\tilde{C} & \begin{bmatrix} D & I \\ 0 & 0 \end{bmatrix} + \begin{bmatrix} D \\ I \end{bmatrix} \tilde{D}M[D \ I] \end{array} \right] \quad (6.17)$$

where

$$M = (I - D\tilde{D})^{-1},$$

and

$$\mathbf{K} \stackrel{s}{=} \left[\begin{array}{c|c} \tilde{A} & \tilde{B} \\ \hline \tilde{C} & \tilde{D} \end{array} \right].$$

This follows from direct elimination of u, y from (6.15). It is important to use a minimal realisation to avoid numerical errors.

6.3.5. Choice of weighting matrices

It is evident from Figure 6.2 that the unweighted plant model has singular values spread over at least $100dB$ at the frequencies shown. As this will lead to highly ‘direction sensitive’ responses, it was deemed necessary to rescale the outputs, thereby balancing the singular values. To do this, we post-multiply \mathbf{G} by the generalised inverse¹

$$\mathbf{W}_o = 500\mathbf{G}^\#(0)$$

to give

$$\mathbf{G}_W = 500\mathbf{G}^\#(0)\mathbf{G}.$$

The singular values of the weighted plant \mathbf{G}_W are shown in Figure 6.6. As expected, they are either approximately 500 or zero at low frequency. This choice of weighting satisfied the performance specifications and was the outcome of a loop shaping methodology [40]. As will be shown, this simple loop shape leads to acceptable closed-loop response when the controller given by (6.14) is implemented. Clearly the controller must be synthesised from a state-space model of \mathbf{G}_W rather than \mathbf{G} .

¹The generalised inverse is defined via the singular value decomposition. If

$$A = U\Sigma V'$$

is a singular value decomposition of A , then we define $A^\#$ as

$$A^\# = V\Sigma^{-1}U'$$

such that $A^\#A = I$.

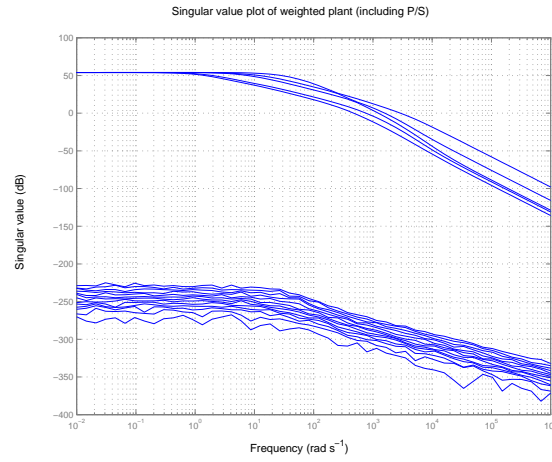


Figure 6.6: Response of the weighted plant

6.4. Normalised \mathcal{H}_∞ controller reduction

It follows from (6.14) that the degree of the controller is the same as that of the plant. In our case, the plant's McMillan degree is 76 and this would lead to a correspondingly high order controller.

In this section, we review the relative error controller order reduction procedure given in [7], the presentation of which will be followed. In this reference it is shown that the observability Gramian of the realisation of Θ in (6.12), and the controllability Gramian of Θ^{-1} in (6.13), may be expressed in terms of X and Y . These matrices are the unique positive definite solutions of (6.8) and (6.9) respectively:

Theorem 6.1. [7] *Let $P = P' \geq 0$ be the controllability Gramian of the realisation of Θ^{-1} in Lemma 6.1 and let $Q = Q' \geq 0$ be the observability Gramian of the realisation of Θ in Lemma 6.1 so that*

$$\begin{aligned} [Z(A - YC'C)Z^{-1}]P + P[Z(A - YC'C)Z^{-1}]' + ZBB'Z' + \\ ZYC'CYZ' = 0 \end{aligned}$$

$$(A - BB'X)'Q + Q(A - BB'X) + \beta^{-4}XBB'X + \beta^{-4}C'C = 0.$$

Then $P = ZYZ'$ and $Q = \beta^{-4}X$.

Choose a realisation of Θ that is inverse-weighted balanced such that

$$P = Q = \text{diag}(\Sigma_1, \Sigma_2) \quad (6.18)$$

where,

$$\Sigma_1 = \text{diag}(\sigma_1 I_{s_1}, \dots, \sigma_r I_{s_r}), \Sigma_2 = \text{diag}(\sigma_{r+1} I_{s_{r+1}}, \dots, \sigma_N I_{s_N})$$

with $\sigma_1 > \dots > \sigma_N \geq 0$ and so that the realisation in (6.12) is partitioned compatibly with Σ_1 and Σ_2 such that

$$\Theta \stackrel{s}{=} \left[\begin{array}{cc|c} A_{11} & A_{12} & B_1 \\ A_{21} & A_{22} & B_2 \\ \hline C_1 & C_2 & D_\Theta \end{array} \right] \quad (6.19)$$

with $D_\Theta = \begin{bmatrix} I & 0 \\ 0 & \beta I \end{bmatrix}$. This then gives

$$\hat{\Theta} = \left[\begin{array}{cc} \hat{\Theta}_{11} & \hat{\Theta}_{12} \\ \hat{\Theta}_{21} & \hat{\Theta}_{22} \end{array} \right] \stackrel{s}{=} \left[\begin{array}{c|c} A_{11} & B_1 \\ \hline C_1 & D_\Theta \end{array} \right] \quad (6.20)$$

which is stable and minimum phase and $\hat{\Theta} = (\mathbf{I} + \Delta)\Theta$, where $\Delta \in \mathcal{RH}_\infty$ will satisfy $\|\Delta\|_\infty \leq \delta$ where [30]

$$\delta := -1 + \prod_{i=r+1}^N (1 + 2\sigma_i \sqrt{1 + \sigma_i^2} + 2\sigma_i^2) \quad (6.21)$$

and

$$\sigma_i^2 = \frac{\nu_i^2}{\beta^4} \left(1 - \frac{\nu_i^2}{\gamma^2 \beta^2} \right)^{-2}.$$

The quantities ν_1^2, \dots, ν_N^2 are the distinct eigenvalues of XY .

Since the central controller is obtained from the controller generator in the form of the right coprime factorisation (6.14), it is shown in [7] that the approximation of Θ induces a relative reduction on the coprime factors of the normalised central controller. This gives guaranteed *a priori* bounds on closed-loop stability and performance degradation when taken with the bound on the relative approximation error. These results are summarised in the following theorem:

Theorem 6.2. [7] Let $\mathbf{K}_{11} = \Theta_{12}\Theta_{22}^{-1}$ be the central controller as defined in (6.14). Suppose that T is an inverse-weighted balancing transformation for Θ so that

$$\begin{aligned}\Sigma &= T^{-1}(ZYZ')(T^{-1})' = T'(\beta^{-4}X)T \\ &= \text{diag}(\sigma_1 I_{s_1}, \dots, \sigma_r I_{s_r}, \sigma_{r+1} I_{s_{r+1}}, \dots, \sigma_N I_{s_N}) \\ &= \text{diag}(\Sigma_1, \Sigma_2)\end{aligned}$$

with $\sigma_1 > \dots > \sigma_N \geq 0$. Applying the transformation T to the central controller \mathbf{K}_{11} and partitioning compatibly with Σ_1 and Σ_2 gives

$$\begin{aligned}\mathbf{K}_{11} &\stackrel{s}{=} \left[\begin{array}{c|c} T^{-1}(A - BB'X - \beta^{-2}ZYC'C)T & T^{-1}(ZYC') \\ \hline (-\beta^{-2}B'X)T & 0 \end{array} \right] \\ &\stackrel{s}{=} \left[\begin{array}{cc|c} \hat{A}_{11} & \hat{A}_{12} & \hat{B}_1 \\ \hat{A}_{21} & \hat{A}_{22} & \hat{B}_2 \\ \hline \hat{C}_1 & \hat{C}_2 & 0 \end{array} \right].\end{aligned}$$

The reduced order controller is then

$$\hat{\mathbf{K}} := \hat{\Theta}_{12}\hat{\Theta}_{22}^{-1} \stackrel{s}{=} \left[\begin{array}{c|c} \hat{A}_{11} & \hat{B}_1 \\ \hline \hat{C}_1 & 0 \end{array} \right], \quad (6.22)$$

and $\mathcal{H}(\mathbf{G}_w, \hat{\mathbf{K}})$ is stable if $\gamma\delta < 1$, in which case

$$\|\mathcal{H}(\mathbf{G}_w, \hat{\mathbf{K}})\|_\infty < \frac{\gamma}{1 - \delta\gamma}.$$

6.5. Controller reduction implementation

The final phase of the work is aimed at the implementation and testing of the reduced-order controller described in Theorem 6.2.

Preliminary testing was conducted on the linear RZIP model. Once the tests were deemed satisfactory, more demanding simulations were performed on the nonlinear PROTEUS model [35].

This programme began with the synthesis of a full-order normalised coprime factor controller. The synthesis used the formula (6.14) and a sub-optimal $\gamma = 3.02$. The controller realisation was then balanced in accordance with Theorem 6.2 so that reduced order controllers can be ‘read off’. This sequence of reduced order controllers was combined with \mathbf{G}_w in order to generate the plot shown in Figure 6.7. This diagram shows, for each reduced order controller, the infinity norm of the closed-loop transfer function as well as the upper bound given in (6.21). It is clear from this diagram that the closed-loop performance improves very little for controllers of McMillan degree ≥ 16 . The upper bound is clearly conservative and indicates that a controller of degree ≥ 30 is required. It should also be noted that the reduced-order controllers are stabilising for order ≥ 12 , while the bounds in Theorem 6.2 indicate that this lowest order for stability is 27.

On the basis of the data in Figure 6.7, a controller of order 18 was selected. This represents a significant reduction for the full order of 76.

Figures 6.8 and 6.9 show the effect of the reduction process on the controller and closed-loop transfer functions respectively. Figure 6.8 shows that the reduction from 76 to 18 states has almost no effect on the controller transfer function. Figure

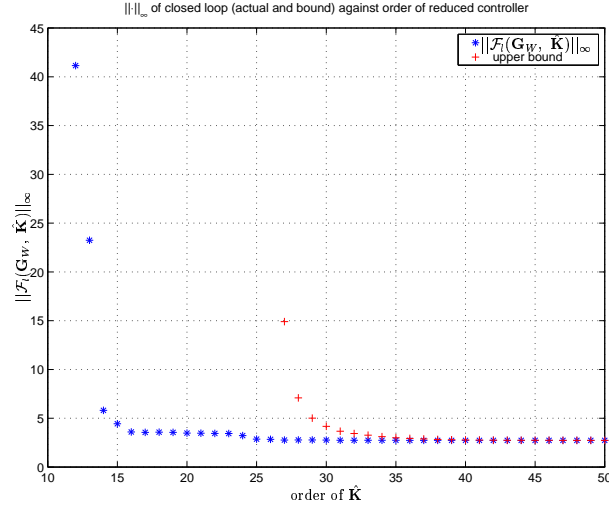


Figure 6.7: Plot of $\|\mathcal{F}_l(\mathbf{G}_W, \hat{\mathbf{K}})\|_\infty$ (*) against the order of the reduced controller. Closed-loop is unstable for order less than 12. The *a priori* bound on $\|\mathcal{F}_l(\mathbf{G}_W, \hat{\mathbf{K}})\|_\infty$ is shown as a (+) where stability is *a priori* guaranteed.

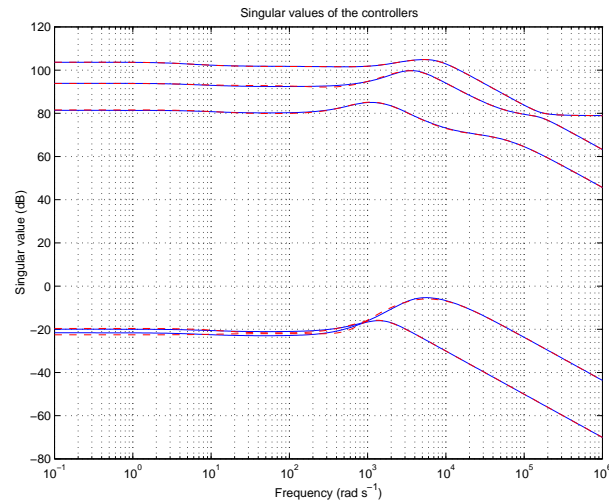


Figure 6.8: Singular value plots of the (-) $\gamma = 3.02$ controller, (- -) reduced $\gamma = 3.91$ controller (18 states)

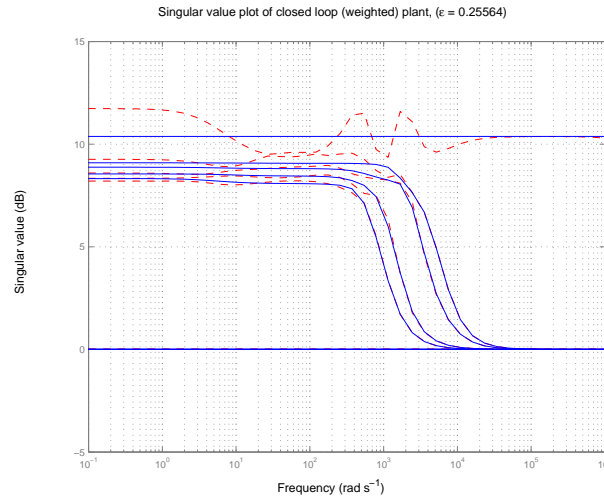


Figure 6.9: Singular value plot for the weighted closed-loop plant with (—) $\gamma = 3.02$ and (---) reduced $\gamma = 3.91$ controller

6.9 shows that the closed loop infinity norm is increased from $\gamma = 3.02$ to $\gamma = 3.91$. γ^{-1} can be interpreted through (6.5) as the maximum permissible model error.

It can be seen that the almost imperceptible changes made by the reduction process to the controller singular values have had a more pronounced impact on the closed-loop.

Controller Simulation Testing

“ ‘There is an old immortal who lives under the sea hereabouts and whose name is Proteus... If you can snare him and hold him tight, he will tell you about your voyage, what courses you are to take, and how you are to sail the sea so as to reach your home...’

“ ‘Can you show me,’ said I, ‘some stratagem by means of which I may catch this old god without his suspecting it and finding me out? For a god is not easily caught- not by a mortal man.’ ”

Homer, *The Odyssey* (IV)

On a tokamak such as TCV, experimental time and machine failures are potentially expensive. In order to obviate these difficulties, a programme of controller testing was undertaken at a simulation level prior to any hardware implementation. The two steps involved simulation testing on RZIP, with a second programme of tests on the nonlinear PROTEUS model. The outcome of the simulation tests will now be presented. This essential part of the work was performed solely by the author.

7.1. Testing on RZIP in SIMULINK

Since RZIP models are linear, the only source of nonlinearity in these simulations will be power supply saturation. It is convenient to use the SIMULINK environment to introduce these effects. A full list of the power supply limits is given in the table below [8].

PF coil P/S	Saturation voltage (+/-)	Saturation current (+/-)
OH1, OH2	1399V	31kA
E1-E8	648V	7.7kA
F1-F8	1250V	7.7kA
G	566V	500A (continuous) 2000A (2s /5min)

For the purposes of this study, we designed a controller that combines good robust stability margins, speed of response, dynamic tracking characteristics and closed-loop decoupling. In order to test for these various characteristics, the closed-loop system was driven with a vector valued reference signal that comprised pulse functions that were staggered in time. The pulse amplitudes were chosen to represent ‘reasonable’ but demanding excursions given the machine dimensions¹. The temporal separation between the pulses allows examination of the inter-loop cross-coupling. The performance of the 18-state reduced order controller is shown in Figure 7.1. It is clear from the responses that the controller possesses all the desired properties; the pulse inputs lie underneath the responses and are barely visible on the plot. This is testimony to the controller’s excellent tracking properties. It is also clear that the only cross-coupling appears at the pulse edges. Although saturation limits were included in the simulation, these played very little role in the particular responses shown here. This is because the TCV power supplies are deliberately over-designed.

¹ This includes both the machine geometry and the electromagnetic specifications.

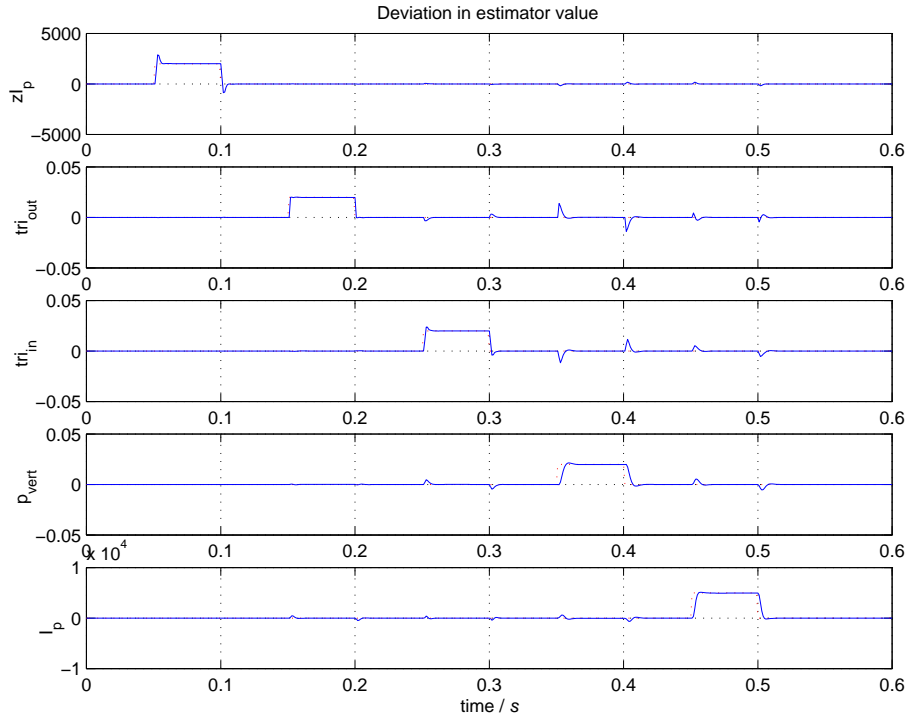


Figure 7.1: Results of closed loop simulation showing (·) reference and (-) RZIP simulated response.

7.2. Testing on the PROTEUS nonlinear tokamak simulation code

PROTEUS is a nonlinear tokamak simulation code that solves the Grad-Shafranov equation using an iterative finite element method. As such it can be used to predict the tokamak plasma's evolution forwards in time, under the assumption of a fixed plasma current. In order to initialise these simulations, PROTEUS requires data about the initial equilibrium, specifically the coil currents and some plasma profile parameters.

Although PROTEUS can model temporal changes in the plasma shape, it does not take account of transport and resistivity phenomena that are known to occur. Since the original code does not have a plasma circuit equation, one had to be introduced, although this is not strictly self-consistent with the initial assumptions. The controller acts to change the plasma current so this dynamic response must

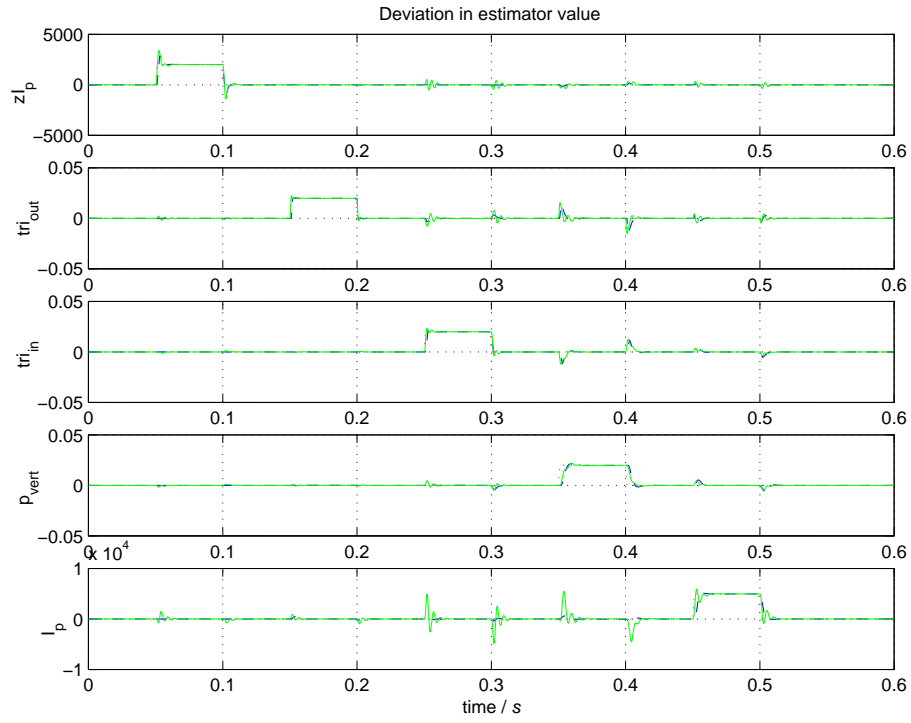


Figure 7.2: Results of closed loop simulations, showing (-) the PROTEUS simulated response, (:) the reference and (- -) the SIMULINK simulated response.

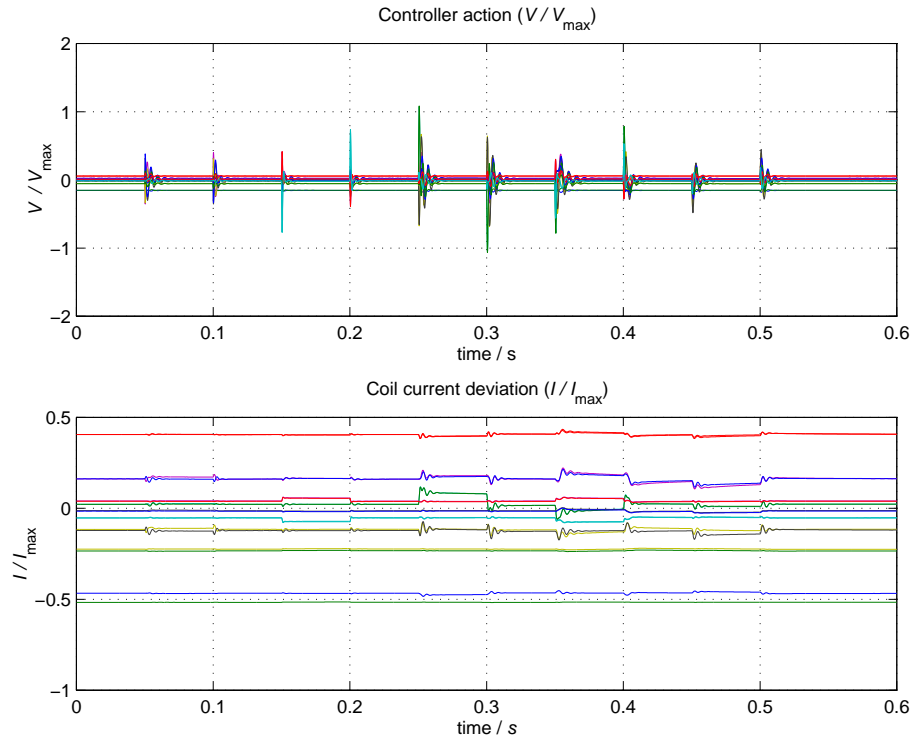


Figure 7.3: Closed loop simulation coil voltage and current.

be represented.

In order to complete the simulation work presented here, we had to introduce a facility for modelling discrete-time controllers and estimator matrices that generate the controlled plant outputs.

The PROTEUS simulations represent a form of robustness test, because the code is significantly different to the RZIP model used in the controller synthesis. The successful operation of the PROTEUS closed-loop therefore lends confidence to the idea that the control methodology will work successfully on the hardware system.

Figure 7.2 shows the results of the PROTEUS simulation with a $0.1ms$ timestep. To aid comparison, the RZIP results are shown on the same diagram. The input and nominal equilibrium conditions were chosen to match those associated with the RZIP results. It can be seen from Figure 7.2 that there is a high level of agreement between the PROTEUS and the RZIP predictions. With that said, one can see a number of lightly damped resonances in the PROTEUS plasma current that are absent in the RZIP equivalent. This is considered likely to represent the inconsistencies in the PROTEUS modelling of the plasma circuit equation.

The practical import of this close agreement is that RZIP simulations that require a few minutes to compute can be used instead of PROTEUS predictions that require days on a like-for-like basis.

Figure 7.3 shows the coil voltage and current as a fraction of the saturation limits. This diagram shows that the power supplies do not saturate except very briefly at 0.25 and 0.3 seconds where the inner triangularity is stimulated.

Conclusions and Future Work

8.1. Conclusions

This thesis has developed a new modelling and control system design paradigm for tokamak fusion reactors. From the initial modelling assumptions, the methodology takes us through the modelling process via model verification to low-order controllers with good performance and robustness characteristics.

Beginning with clearly stated assumptions, a new modeling approach is developed to derive a nonlinear model together with its linearised counterpart, using techniques from classical mechanics. This new approach to the tokamak modelling problem clarifies many of the relationships between the assumptions and the model properties. The model presented here incorporates plasma resistance from the start. The effect of removing plasma resistance from the model is also clarified and it is shown that such zero resistance terms leads to the introduction of uncontrollable modes at the origin.

All linearised models with the same choice of states can be represented in the same form presented here, simply differing in coefficients. As such, searching within this space for an optimal model provides the best among all linear models with the same choice of states. Thus, taking a simple rigid displacement model as a starting point is sensible.

Previous grey-box modelling work was seen to suffer from the ad-hoc nature of the cost function used. Here a new, more systematic approach was developed using the infinity norm of the relative model error, interpreted in a worst case energy gain sense.

Identification experiments on the large JT-60U tokamak confirmed the machine-independence of the plasmaless modelling method. Open-loop plasma frequency response identification experiments were performed on JT-60U for both ohmically-heated plasmas and plasmas heated by neutral beam injection.

It was found that the nominal plasma response model lay close to the best-fit model and that it gave excellent predictions in both the time and frequency domain, excepting some errors relating to the plasma current response. The modelling approach has been shown to be suitable for large tokamaks with both ohmically heated and neutral beam injection heated plasmas and for very different values of β .

The last part of the thesis demonstrates the utility and sufficiency of the derived linear plasma equilibrium response model in controller design studies. It also shows the effectiveness of a recently developed model reduction methodology for normalised coprime factor controller reduction. The known procedures of normalised coprime factor controller design produce control systems with order equal to that of the loop-shaped plant [30], [40]. Since we have used non-dynamic weights, the controller order is 76 according to this established wisdom. It is possible to reduce the controller order to 18 using the techniques described in [7] without a significant performance degradation. It was also demonstrated that this performance was successfully transferred to the nonlinear tokamak simulation code PROTEUS. In this context, this successful transfer is indicative of the inherent robustness properties of the controller. This is because PROTEUS is based on modelling assumptions quite different to those used in the model presented here, on which the controller synthesis was based. Given the successful transfer

to PROTEUS, it is to be expected that good performance would be achieved on the TCV hardware using this methodology.

We conclude that the work presented constitutes a reliable and fast methodology for producing and verifying accurate low order tokamak models, and low order robust controllers with excellent performance characteristics.

8.2. Future work

On the modelling side, further investigation on how to better quantify the model uncertainty in a structured way, against experimental data, could form the basis of future work. This would include an interpretation of the stability margin in terms of model parameter errors. Investigations of the consequences of uncontrollable modes due to superconducting coils on ITER could prove to be important.

Recommendations must also include a continuation of the controller testing programme. A first step would be tests on the more comprehensive DINA simulation code, which would provide an even more realistic simulation of the tokamak operating conditions, and would permit a controller design that properly accounted for the plasma current and resistance. Simulations involving more exotic and demanding equilibria could then be simply executed given that the design software and methodology are now established. Further to that actual hardware tests on the TCV digital control system would definitively prove the efficacy of the methodology.

Bibliography

- [1] V. Mukhovatov and V. Shafranov, “Plasma equilibrium in a tokamak,” *Nuclear Fusion*, vol. 11, 1971.
- [2] J. Wesson, *Tokamaks*. Oxford Science Publications, 1997.
- [3] A. Coutlis, D. Limebeer, J. Wainwright, J. Lister, and P. Vyas, “Frequency response identification of the dynamics of a tokamak plasma,” *IEEE Transactions on Control System Technology*, vol. 8, no. 4, 2000.
- [4] R. Albanese and F. Villone, “The linearized CREATE-L model for the control of current, position and shape in tokamaks,” *Nuclear Fusion*, vol. 38, no. 5, 1998.
- [5] A. Coutlis, I. Bandyopadhyay, J. Lister, P. Vyas, R. Albanese, D. Limebeer, F. Villone, and J. Wainwright, “Measurement of the open loop plasma equilibrium response in TCV,” *Nuclear Fusion*, vol. 35, no. 5, 1999.
- [6] J. Lister, A. Sharma, D. Limebeer, Y. Nakamura, J. Wainwright, and R. Yoshino, “Plasma equilibrium response modelling and validation on JT-60U,” *Nuclear Fusion (accepted for publication)*.
- [7] H. El-Zobaidi, I. Jaimoukha, and D. Limebeer, “Normalized \mathcal{H}_∞ controller reduction with *a priori* bounds,” *IEEE Transactions on Automatic Control*, vol. 46, no. 9, 2001.

- [8] J. Lister, F. Hofmann, J.-M. Moret, F. Bühlmann, M. Dutch, D. Fasel, A. Favre, P.-F. Isoz, B. Marletaz, P. Marmillod, Y. Martin, A. Perez, and D. Ward, "The control of Tokamak Configuration Variable plasmas," *Fusion Technology*, vol. 32, 1997.
- [9] F. Hofmann, J.-M. Moret, and D. Ward, "Stability analysis of the vertical position control loop in TCV using rigid and deformable plasma models," *Nuclear Fusion*, vol. 38, no. 12, 1998.
- [10] E. Lazarus, J. Lister, and G. Neilson, "Control of the vertical instability in tokamaks," *Nuclear Fusion*, vol. 30, no. 1, 1990.
- [11] J. Lister, E. Lazarus, A. K. abd J-M Moret, J. Ferron, F. Helton, L. Lao, J. Leuer, E. Strait, T. Taylor, and A. Turnbull, "Experimental study of the vertical stability of high decay index plasmas in the DIII-D tokamak," *Nuclear Fusion*, vol. 30, no. 11, 1990.
- [12] J. Wainwright, D. Copsey, D. Limebeer, M. Haines, and A. Portone, "Extensions to single filament modelling of a tokamak plasma," *Nuclear Fusion*, vol. 37, no. 12, 1997.
- [13] D. Humphreys, J. Leuer, and M. Walker, "minimal plasma response models for design of tokamak equilibrium controllers with high dynamic accuracy," *41st Annual Meeting of Division of Plasma Physics, American Physical Society, Seattle, WA, November 15-19, 1999*.
- [14] D. Humphreys and I. Hutchinson, "Axisymmetric magnetic control design in tokamaks using perturbed equilibrium plasma response modelling," *Fusion Technology*, vol. 23, 1993.
- [15] F. Hofmann, M. Dutch, D. Ward, M. Anton, I. Furno, J. Lister, and J.-M. Moret, "Vertical instabilities in TCV: Comparison of experimental and theoretical growth rates," *Nuclear Fusion*, vol. 32, no. 5, 1997.

- [16] F. Hofmann, A. Favre, P.-F. Isoz, Y. Martin, J.-M. Moret, and C. Nieswand, "Vertical position control in TCV: Comparison of model predictions with experimental results," *CRPP-EPFL internal report LRP*, no. 653, 1999.
- [17] F. Hofmann, M. Dutch, A. Favre, Y. Martin, J.-M. Moret, and D. Ward, "Feedback stabilization of axisymmetric modes in the TCV tokamak using active coils inside and outside the vacuum vessel," *Nuclear Fusion*, vol. 38, no. 3, 1998.
- [18] R. Khayrutdinov and V. Lukash, "Studies of plasma equilibrium and transport in a tokamak fusion device with the inverse-variable technique," *Journal of Computational Physics*, vol. 109, no. 2, 1993.
- [19] R. Khayrutdinov, J. Lister, V. Lukash, and J. Wainwright, "Comparing DINA code simulations with TCV experimental plasma equilibrium responses," *Plasma Physics and Controlled Fusion*, vol. 43, no. 3, 2001.
- [20] A. Portone, R. Albanese, Y. Gribov, M. Huguet, D. Humphreys, C. Kessel, P.-L. Mondino, L. D. Pearlstein, and J. Wesley, "Dynamic control of plasma position and shape in ITER," *Fusion Technology*, vol. 32, 1997.
- [21] M. Firestone, J. Morrow-Jones, and T. K. Mau, "Comprehensive feedback control of a tokamak fusion reactor," *Fusion Technology*, vol. 32, 1997.
- [22] P. Vyas, *Plasma vertical position control on COMPASS-D*. PhD thesis, Oxford University, 1996.
- [23] P. Vyas, D. Mustafa, and W. Morris, "Vertical position control on COMPASS-D," *Fusion Technology*, vol. 33, 1998.
- [24] M. Ariola, G. Ambrosino, J. Lister, A. Pironti, F. Villone, and P. Vyas, "A modern plasma controller tested on the TCV tokamak," *Fusion Technology*, vol. 36, 1999.

- [25] M. Walker, D. Humphreys, and J. Ferron, "Control of plasma poloidal shape and position in the DIII-D tokamak," *Proceedings of the 36th Conference on Decision and Control, San Diego, California USA, December, 1997*.
- [26] G. Ambrosino, M. Ariola, Y. Mitrishkin, A. Pironti, and A. Portone, "Plasma current and shape control in tokamaks using \mathcal{H}_∞ and μ -synthesis," *Proceedings of the 36th Conference on Decision and Control, San Diego, California USA., 1997*.
- [27] M. Al-Husari, B. Hendel, M. Jaimoukha, E. Kasenally, D. Limebeer, and A. Portone, "Vertical stabilisation of tokamak plasmas," *Proceedings of the 30th Conference on Decision and Control, Brighton, England., 1991*.
- [28] H. Goldstein, *Classical Mechanics (2nd edition)*. Addison-Wesley, 1980.
- [29] A. Coutlis, *System identification for MIMO discrete and continuous-time systems*. PhD thesis, University of London, 1996.
- [30] M. Green and D. Limebeer, *Linear Robust Control*. Prentice-Hall, 1995.
- [31] G. Stewart, *Introduction to Matrix Computations*. Academic Press NY, 1973.
- [32] K. Zhou, J. Doyle, and K. Glover, *Robust Optimal Control*. Prentice-Hall, 1995.
- [33] J. Wainwright, A. Sharma, and D. Limebeer, "Frequency Response Identification of the Fast Coil system of a Tokamak," *Proceedings of: International Symposium on Quantitative Feedback Control and Robust Frequency Domain Methods, University of Natal, Durban, RSA, August 26-27, 1999*.
- [34] J.-M. Moret, F. Buhlmann, D. Fasel, F. Hofmann, and G. Tonetti, "Magnetic measurements on the TCV tokamak," *Review of Scientific Instruments*, vol. 69, no. 6, 1998.

-
- [35] R. Albanese, J. Blum, and O. de Barbieri *12th Conference on Numerical Simulations of Plasmas, San Francisco, CA.*, 1987.
 - [36] M. Safonov and R. Chiang, “A Schur method for balanced-truncation model-reduction,” *IEEE Transactions on Automatic Control*, vol. 34, no. 7, 1989.
 - [37] K. Glover and D. McFarlane, “Robust stabilisation of normalized coprime factor plant descriptions with \mathcal{H}_∞ -bounded uncertainty,” *IEEE Transactions on Automatic Control*, vol. 34, no. 8, 1989.
 - [38] A. Portone, *Modelling and control of tokamak plasmas in fusion devices*. PhD thesis, University of London, 1994.
 - [39] K. Zhou, “Frequency-weighted \mathcal{L}_∞ norm and optimal Hankel norm model reduction,” *IEEE Transactions on Automatic Control*, vol. 40, no. 10, pp. 1687–1699, 1995.
 - [40] D. McFarlane and K. Glover, “A loop-shaping design procedure using \mathcal{H}_∞ synthesis,” *IEEE Transactions on Automatic Control*, vol. 37, no. 6, 1992.
 - [41] W. Smythe, *Static & Dynamic Electricity (3rd edition)*. McGraw-Hill, 1989.

Tokamak Equilibrium

A comprehensive discussion of tokamak equilibrium physics is to be found in [2], the presentation of which this Appendix closely follows.

A.1. Tokamak equilibrium

Tokamak equilibrium can be considered as an internal balance between the the plasma pressure and the forces from the magnetic field. This gives rise to the shape and position of the plasma, controlled by the currents in the external coils.

The largest component of the magnetic field is the toroidal field produced by the poloidal currents in the external coils. The smaller poloidal component of the field is produced mainly by the toroidal plasma current. A further contribution to the poloidal field is made by the toroidal currents in the external coils used for shaping and position control.

Neglecting the small poloidal plasma current, taking the line integral around a circular toroidal circuit inside the toroidal field coils, Ampère's law gives us the toroidal magnetic field B_ϕ ,

$$2\pi RB_\phi = \mu_0 I_T, \tag{A.1}$$

where R is the major radius coordinate and I_T is the total current in the coils. Naturally it follows that

$$B_\phi \propto \frac{1}{R}.$$

The poloidal magnetic field \mathbf{B}_θ and the toroidal current profile j_ϕ are interdependent. Where this current is driven by a toroidal electric field, the steady-state current profile is determined by the electrical conductivity. Since this increases with electron temperature as $T_e^{3/2}$, the current profile is peaked towards the centre where the temperature is highest. It is possible to drive the current by non-ohmic means (such as neutral beam injection) which can result in a different current profile.

Since the plasma mass density is so low (typically five orders of magnitude below atmospheric), and the internal forces on the plasma are large, to an excellent approximation the internal forces must balance. The plasma pressure exerts an outward force across the minor radius, and the poloidal magnetic field exerts a constraining inward force. The difference is made up by the magnetic pressure of the toroidal magnetic field, which may act inward or outward.

The resultant magnetic field produces nested toroidal magnetic surfaces. The actual field lines follow a helical path on the magnetic surfaces they define. The pressure in the plasma is constant along the magnetic field, due to the fast response to force imbalance of the plasma.

The toroidal geometry of the plasma results in a hoop force, since the plasma current rests in its own vertical magnetic field, which acts to radially expand the plasma torus. To achieve radial equilibrium we apply an opposing vertical magnetic field, which combines with the plasma current to balance this force.

The equilibrium is partly determined by the externally imposed conditions such as total current, applied magnetic field and heating, and partly by plasma behaviour. The density and temperature profiles are governed by the transport properties which are in turn affected by plasma instabilities.

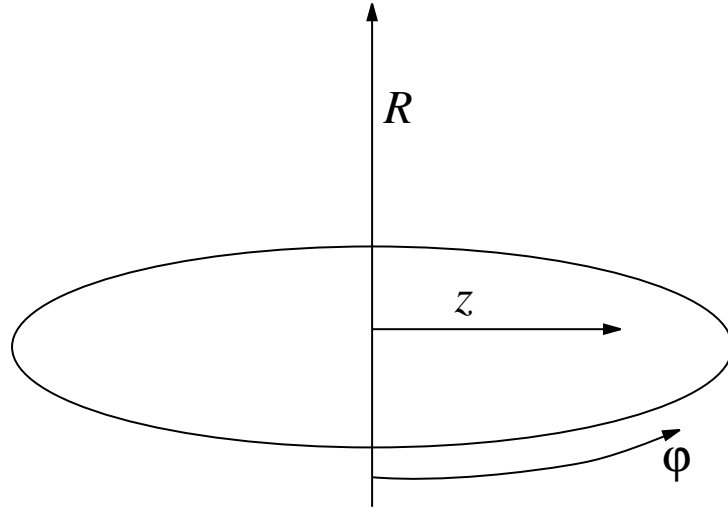


Figure A.1: Cylindrical coordinate system. $R = 0$ is the major axis of the torus.

A.2. Flux functions

The fundamental equilibrium condition is that the forces are zero at all points. Assuming the absence of plasma resistance, (*i.e.* ideal MHD conditions) we require that the magnetic and pressure forces balance at all points,

$$\mathbf{j} \times \mathbf{B} = \nabla p \quad (\text{A.2})$$

subject to toroidal symmetry (see Figure A.1), where \mathbf{j} is the current density, \mathbf{B} is the magnetic field and p is the pressure. From this it follows immediately that

$$\mathbf{B} \cdot \nabla p = 0,$$

showing that the magnetic surfaces are surfaces of constant pressure, and that

$$\mathbf{j} \cdot \nabla p = 0,$$

showing that the lines of current lie on the magnetic surfaces.

At this point it is convenient to introduce the poloidal magnetic flux function

Ψ . This function is determined by the poloidal flux lying within each magnetic surface and is therefore constant on that surface. Consequently

$$\mathbf{B} \cdot \nabla \Psi = 0.$$

Defining the flux function Ψ as the poloidal flux per unit radian in ϕ , the poloidal magnetic field is related to Ψ by¹

$$B_R = -\frac{1}{R} \frac{\partial \Psi}{\partial z}, \quad B_z = \frac{1}{R} \frac{\partial \Psi}{\partial R} \quad (\text{A.3})$$

conforming to the Maxwell equation $\nabla \cdot \mathbf{B} = 0$, that is

$$\frac{1}{R} \frac{\partial R B_R}{\partial R} + \frac{\partial B_z}{\partial z} = 0.$$

The flux function Ψ is arbitrary to an additive constant which is chosen for convenience. From the symmetry of \mathbf{j} and \mathbf{B} it is clear that a current flux function also exists. This function, f , is related to the poloidal current density by

$$j_R = -\frac{1}{R} \frac{\partial f}{\partial z}, \quad j_z = \frac{1}{R} \frac{\partial f}{\partial R}. \quad (\text{A.4})$$

Comparison of (A.4) with Ampère's equation,

$$j_R = -\frac{1}{\mu_0} \frac{\partial B_\phi}{\partial z}, \quad j_z = \frac{1}{\mu_0 R} \frac{\partial R B_\phi}{\partial R}$$

gives the relation between f and the toroidal magnetic field as

$$f = \frac{R B_\phi}{\mu_0}. \quad (\text{A.5})$$

It can be shown that f is a function of Ψ by taking the scalar product of (A.2)

¹See Appendix E for the differential operators in cylindrical coordinates.

with \mathbf{j} to obtain $\mathbf{j} \cdot \nabla p = 0$, and then substituting (A.4) for \mathbf{j} . Thus

$$\frac{\partial f}{\partial R} \frac{\partial p}{\partial z} - \frac{\partial f}{\partial z} \frac{\partial p}{\partial R} = 0$$

and so

$$\nabla f \times \nabla p = 0,$$

proving that f is a function of p . Then, since $p = p(\Psi)$, it follows that $f = f(\Psi)$. The flux functions as defined here give the poloidal flux per radian in ϕ . It is possible to define the total flux function for the torus which is simply $2\pi\Psi$.

A.3. The Grad-Shafranov equation

We can write the equilibrium equation for a tokamak as a differential equation in the poloidal flux function Ψ , accounting for axisymmetry. This equation, which has two arbitrary functions, is called the Grad-Shafranov equation.

The equilibrium equation (A.2)

$$\mathbf{j} \times \mathbf{B} = \nabla p$$

can be written

$$\mathbf{j}_p \times \hat{\phi} B_\phi + j_\phi \hat{\phi} \times \mathbf{B}_p = \nabla p \quad (\text{A.6})$$

where \mathbf{j}_p is the poloidal current density, \mathbf{B}_p is the poloidal magnetic field, and $\hat{\phi}$ is the unit vector in the direction of the toroidal coordinate (see Figure A.1).

We can now rewrite (A.6) in terms of the flux function Ψ . We can express (A.3) and (A.4) more compactly as

$$\mathbf{B}_p = \frac{1}{R}(\nabla\Psi \times \hat{\phi}) \quad (\text{A.7})$$

and

$$j_p = \frac{1}{R}(\nabla f \times \hat{\phi}). \quad (\text{A.8})$$

Substituting these new relations into (A.6) and noting that

$$\hat{\phi} \cdot \nabla \Psi = \hat{\phi} \cdot \nabla f = 0,$$

gives

$$-\frac{B_\phi}{R} \nabla f + \frac{j_\phi}{R} \nabla \Psi = \nabla p. \quad (\text{A.9})$$

We can write

$$\nabla f(\Psi) = \frac{df}{d\Psi} \nabla \Psi$$

and similarly for p

$$\nabla p(\Psi) = \frac{dp}{d\Psi} \nabla \Psi,$$

and substitution into (A.9) gives

$$j_\phi = R \frac{dp}{d\Psi} + B_\phi \frac{df}{d\Psi}.$$

Substituting (A.5) for B_ϕ gives

$$j_\phi = R p' + \frac{\mu_0}{R} f f' \quad (\text{A.10})$$

where we write x' to denote the derivative $\frac{dx}{d\Psi}$.

To write j_ϕ in terms of Ψ we must introduce Ampère's equation

$$\mu_0 \mathbf{j} = \nabla \times \mathbf{B}.$$

Substitution of (A.3) into the toroidal component of the above equation gives

$$-\mu_0 R j_\phi = R \frac{\partial}{\partial R} \frac{1}{R} \frac{\partial \Psi}{\partial R} + \frac{\partial^2 \Psi}{\partial z^2}.$$

Substituting this for j_ϕ into (A.10) gives, finally,

$$R \frac{\partial}{\partial R} \frac{1}{R} \frac{\partial \Psi}{\partial R} + \frac{\partial^2 \Psi}{\partial z^2} = -\mu_0 R^2 p'(\Psi) - \mu_0^2 f(\Psi) f'(\Psi). \quad (\text{A.11})$$

Equation (A.11) is the Grad-Shafranov equation. The flux surfaces and profiles of j_ϕ , p , and B_ϕ are typically obtained numerically.

Circular current loops

B.1. Inductance of circular current loops

The mutual inductance M_{12} of two coaxial current carrying loops (see Figure B.1) is given by [41]

$$M_{12} = \frac{2\mu\sqrt{ab}}{k} \left[\left(1 - \frac{k^2}{2}\right) K(k^2) - E(k^2) \right] \quad (\text{B.1})$$

where $k^2 = \frac{4ab}{[(a+b)^2 + c^2]}$ and K, E are elliptic integrals of the first and second kind respectively. The self inductance of one such loop is given by [41]

$$L_{loop} = \mu R \left[\ln \left(\frac{8R}{r} \right) - \frac{7}{4} \right] \quad (\text{B.2})$$

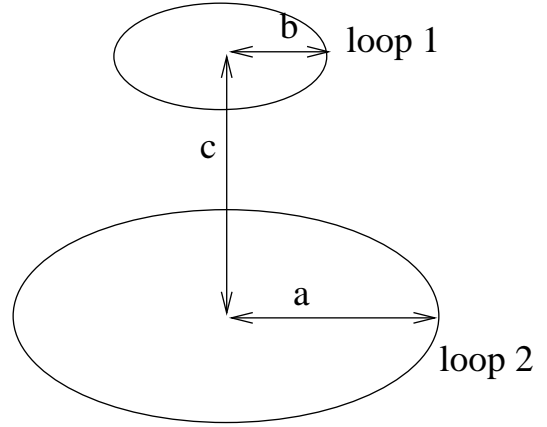


Figure B.1: Two current carrying loops

where r is the minor radius of the loop, in the approximation $R \gg r$.

B.2. Magnetic field due to circular current loops

From one toroidal current element with current I at position $R = a$, $z = z_1$, we get the magnetic field \mathbf{B}_I at $R = \rho$, $z = z_2$. Let $h = z_1 - z_2$ and let

$$k^2 = \frac{4a\rho}{((a + \rho)^2 + h^2)}.$$

The magnetic field components are given by [41]:

$$B_{RI} = \frac{\mu_0 I h}{2\pi \rho \sqrt{(a + \rho)^2 + h^2}} \left[-K + \frac{a^2 + \rho^2 + h^2}{(a - \rho)^2 + h^2} E \right]$$

$$B_{zI} = \frac{\mu_0 I}{2\pi \sqrt{(a + \rho)^2 + h^2}} \left[K + \frac{a^2 - \rho^2 - h^2}{(a - \rho)^2 + h^2} E \right]$$

where K and E are elliptic integrals of the first and second kinds respectively.

JT-60U Control System

C.1. Control parameter estimator algorithm

C.1.1. Definitions

\mathbf{B}_p is a vector of tangential and poloidal magnetic field probe signals. \mathbf{C} , \mathbf{D} and \mathbf{E} are respective vectors of coefficients. I_D is the D-coil current, I_{VT} is the T coil current, and I_p is the plasma current.

C.1.2. Estimator algorithm

This is the algorithm used to calculate the values of the JT-60U plasma control parameters in real-time.

$$dR = \left((\mathbf{B}_p \cdot \mathbf{C}_R) + (\mathbf{B}_p \cdot \mathbf{D}_R \frac{I_D}{I_p}) \right) / I_p + const.$$

$$dZ = \left((\mathbf{B}_p \cdot \mathbf{C}_Z) + (\mathbf{B}_p \cdot \mathbf{D}_Z \frac{I_D}{I_p}) \right) / I_p + const.$$

$$X_p = \left((\mathbf{B}_p \cdot \mathbf{C}_X) + (\mathbf{B}_p \cdot \mathbf{D}_X \frac{I_D}{I_p}) + (\mathbf{B}_p \cdot \mathbf{E}_X \frac{I_{VT}}{I_p}) \right) / I_p + const.$$

$$CL1 = \left((\mathbf{B}_p \cdot \mathbf{C}_\delta) + (\mathbf{B}_p \cdot \mathbf{E}_\delta \frac{I_{VT}}{I_p}) \right) / I_p + \text{const.}$$

I_p is directly measured with a Rogowski coil.

C.2. The plasma controllers

To implement a good closed loop model, useful in designing experiments, the controllers need to be modelled.

There are a number of control modes available on JT-60U:

Control mode	Function
0	PF coil current control
1	Plasma current control
2	PF coil voltage control
9	Plasma current control
13	Feedback control of dR, dZ, Xp, δ .

When mode 13 is selected the F coil still operates under mode 9.

C.2.1. Modelling of the PF coil current control loop (mode 0)

Plasmaless control is carried out in mode 0. The coil voltage vector \mathbf{V} is given by

$$\mathbf{V} = (\mathbf{I}_{ref} + (\mathbf{I}_{ref} - \mathbf{I}_{pol}) \times \mathbf{G}_{DDC}) \mathbf{R}_x.$$

\mathbf{G}_{DDC} is a control gain matrix and \mathbf{R}_x is a constant vector.

$$\mathbf{I}_{pol} = [I_D \ I_F \ I_T \ I_V \ I_H]^T.$$

The constant vectors and matrices are given in Section C.3.

C.2.2. Modelling of the plasma control loop (modes 13, 9)

For mode 13 the coil voltage is given by

$$\mathbf{V} = \mathbf{I}_{pol} \mathbf{R}_x + (\mathbf{FBP}_{13} \Delta \mathbf{CP} + \mathbf{FBD}_{13} \frac{d\Delta \mathbf{CP}}{dt}) \mu_0 I_p$$

$$\Delta \mathbf{CP} = (\mathbf{CP}_{ref} - \mathbf{CP})$$

where

$$\mathbf{CP} = [dR \ dZ \ I_p \ X_p \ \delta]^T.$$

For mode 9 the F coil voltage is given by

$$V^F = I_{pol}^F R_x^F + (F B P_9^F \Delta \mathbf{CP}).$$

\mathbf{FBP}_{13} , \mathbf{FBD}_{13} and \mathbf{FBP}_9 are feedback gain matrices given in Section C.3.

The two controllers can be combined simply:

$$\mathbf{V} = (\mathbf{I}_{pol} \mathbf{R}_x) + ((\mathbf{FBP}_{13} \Delta \mathbf{CP} + \mathbf{FBD}_{13} \frac{d\Delta \mathbf{CP}}{dt}) \mu_0 I_p + \mathbf{FBP}_9 \Delta \mathbf{CP}).$$

C.3. JT-60U feedback controller matrices

The coil indexing order is D F T V H.

$$\mathbf{R}_x = [3.5 \times 10^{-3} \quad 4.22 \times 10^{-3} \quad 9.08 \times 10^{-3} \quad 12.79 \times 10^{-3} \quad 7.97 \times 10^{-3}].$$

The diagonal matrix \mathbf{G}_{DDC} is given by

$$\mathbf{G}_{DDC}^{ii} = (\tau_i \mathbf{f}_i)$$

and zero elsewhere, where

$$\boldsymbol{\tau} = [652 \ 2910 \ 683 \ 3940 \ 80]$$

and

$$\boldsymbol{f} = [0.05 \ 0.1 \ 0.05 \ 0.07 \ 0.06].$$

τ is a vector related to the L/R times for each coil.

The feedback matrices are

$$\mathbf{FBP}_{13} = \begin{bmatrix} 0 & 5 \times 10^3 & 0 & 6 \times 10^4 & 0 \\ 0 & 0 & 0 & 0 & 0 \\ 0 & 0 & 0 & 0 & 1.5 \times 10^4 \\ -5 \times 10^3 & 0 & 3 \times 10^{-3} & 0 & 0 \\ 0 & 5 \times 10^4 & 0 & 0 & 0 \end{bmatrix}$$

$$\mathbf{FBD}_{13} = \begin{bmatrix} 0 & 0 & 0 & 0 & 0 \\ 0 & 0 & 0 & 0 & 0 \\ 0 & 0 & 0 & 0 & 0 \\ -3 \times 10^1 & 0 & 0 & 0 & 0 \\ 0 & 3 \times 10^2 & 0 & 0 & 0 \end{bmatrix}$$

$$\mathbf{FBP}_9 = \begin{bmatrix} 0 & 0 & 0 & 0 & 0 \\ -4 \times 10^3 & 0 & -1 \times 10^{-2} & 0 & 0 \\ 0 & 0 & 0 & 0 & 0 \\ 0 & 0 & 0 & 0 & 0 \\ 0 & 0 & 0 & 0 & 0 \end{bmatrix}.$$

Example of a Coupled LR Circuit

The purpose of this appendix is to illustrate, using the simple LR circuit in Figure D.1, the mechanism behind the creation of uncontrollable modes in tokamak models containing idealised superconducting plasmas¹. To the author's knowledge this problem has not been discussed previously.

In this diagram the secondary circuit represents the plasma, the primary circuit represents the tokamak coils and the mutual inductance the magnetic coupling between them.

It follows from simple circuit theory that:

$$\begin{bmatrix} 1 \\ 0 \end{bmatrix} V_1 = \begin{bmatrix} L_1 & M_{12} \\ M_{12} & L_2 \end{bmatrix} \begin{bmatrix} \dot{I}_1 \\ \dot{I}_2 \end{bmatrix} + \begin{bmatrix} R_1 & 0 \\ 0 & R_2 \end{bmatrix} \begin{bmatrix} I_1 \\ I_2 \end{bmatrix} \quad (\text{D.1})$$

which can be put into state-space form:

$$\begin{bmatrix} 1 \\ 0 \end{bmatrix} u = \mathcal{M}\dot{x} + \mathcal{R}x$$

$$\Rightarrow \quad \dot{x} = -\mathcal{M}^{-1}\mathcal{R}x + \mathcal{M}^{-1} \begin{bmatrix} 1 \\ 0 \end{bmatrix} u,$$

¹The results are also relevant to tokamaks with superconducting coils such as ITER. However in that case we would not simply be able to ignore the resulting uncontrollable modes.

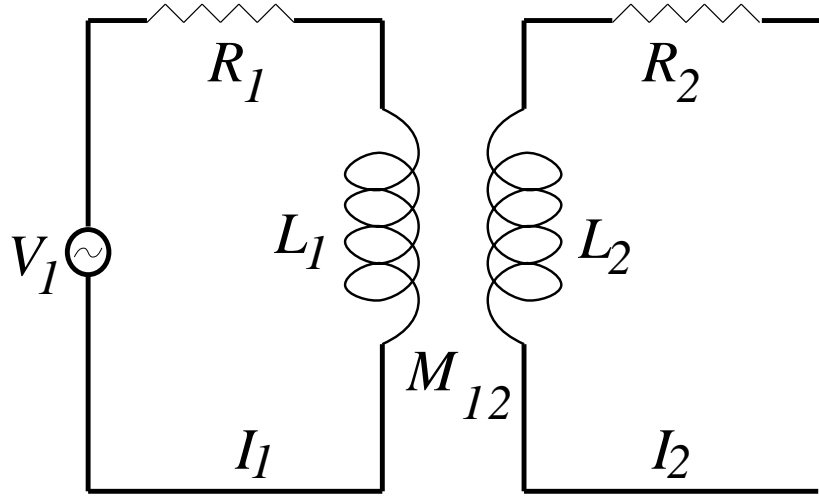


Figure D.1: A coupled LR circuit

with

$$A = -\mathcal{M}^{-1}\mathcal{R},$$

and

$$B = \begin{bmatrix} \alpha \\ \gamma \end{bmatrix}$$

where

$$\mathcal{M}^{-1} = \begin{bmatrix} \alpha & \beta \\ \gamma & \delta \end{bmatrix}.$$

Observe that \mathcal{M} is necessarily invertible because $L_1 > M_{12}$ and $L_2 > M_{12}$.

Hence

$$A = - \begin{bmatrix} \alpha R_1 & \beta R_2 \\ \gamma R_1 & \delta R_2 \end{bmatrix}.$$

It follows from standard passivity arguments that $\text{Re } \lambda_i(A) < 0$ for $R_1, R_2 > 0$.

The controllability matrix is

$$\left[\begin{array}{c|c} sI - A & B \end{array} \right] = \left[\begin{array}{cc|c} s + \alpha R_1 & \beta R_2 & \alpha \\ \gamma R_1 & s + \delta R_2 & \gamma \end{array} \right]. \quad (\text{D.2})$$

It is therefore the case that (A, B) is controllable if $R_2 > 0$. On the other hand, if $R_2 = 0$, the matrix in (D.2) will have unit rank at $s = 0$, indicating the presence of an uncontrollable mode there.

In reality we will never face the $R_2 = 0$ situation and so the associated uncontrollable mode may be ignored.

In the case that $R_2 = 0$, it follows that

$$I_2 = -\frac{M_{12}}{L_2} I_1 + C,$$

demonstrating that under these conditions the two loop currents are dependent.

We can also see that

$$\dot{I}_1 = -\frac{I_2 R_2}{M_{12}}$$

in the case that I_2 is constant, which illustrates the need to ramp I_1 in order that I_2 be maintained at a fixed value.

Differential Operators in Cylindrical Coordinates

In cylindrical coordinates r, ϕ, z ,

$$ds^2 = dr^2 + r^2 d\phi^2 + dz^2,$$

and the differential operators are given by

$$\nabla f = \frac{\partial f}{\partial r} \hat{\mathbf{r}} + \frac{1}{r} \frac{\partial f}{\partial \phi} \hat{\boldsymbol{\phi}} + \frac{\partial f}{\partial z} \hat{\mathbf{z}}$$

$$\nabla \cdot \mathbf{A} = \frac{1}{r} \frac{\partial}{\partial r} (r A_r) + \frac{1}{r} \frac{\partial A_\phi}{\partial \phi} + \frac{\partial A_z}{\partial z}$$

$$\nabla \times \mathbf{A} = \left(\frac{1}{r} \frac{\partial A_z}{\partial \phi} - \frac{\partial A_\phi}{\partial z} \right) \hat{\mathbf{r}} + \left(\frac{\partial A_r}{\partial z} - \frac{\partial A_z}{\partial r} \right) \hat{\boldsymbol{\phi}} + \left(\frac{1}{r} \frac{\partial}{\partial r} (r A_\phi) - \frac{1}{r} \frac{\partial A_r}{\partial \phi} \right) \hat{\mathbf{z}}.$$